Title

Forecasting Extreme Wildfires with WRF-Fire

Permalink

https://escholarship.org/uc/item/0qk6522h

Author

Turney, Francis

Publication Date

2024

Peer reviewed|Thesis/dissertation

UNIVERSITY OF CALIFORNIA

Los Angeles

Forecasting Extreme Wildfires with WRF-Fire

A dissertation submitted in partial satisfaction

of the requirements for the degree Doctor of Philosophy

in Atmospheric and Oceanic Sciences

by

Francis Turney

2024

ABSTRACT OF THE DISSERTATION

Forecasting Extreme Wildfires with WRF-Fire

by

Francis Turney

Doctor of Philosophy in Atmospheric and Oceanic Sciences

University of California, Los Angeles, 2024

Professor Pablo Saide Peralta, Chair

Large wildfires are notoriously unpredictable and devastating, with the smoke emitted

creating unhealthy air across vast regions and warming the globe in in a similar way to volcanic

eruptions. Despite their increasing prevalence and intensity, the drivers of these extreme

events are often difficult to understand and model. A distinction is often made between wind

driven and fuels driven fires, but a spectrum of regimes exist between the two categories, and

environmental factors such as bark beetle infestation and human fire suppression have the

potential to influence these events in ways not fully understood. Modeling wildfires thus has

the potential to alert communities to danger and address fundamental questions about the

drivers of large wildfires, although the process can be deeply challenging, as numerical

methods, fuel models, resolution, meteorology, turbulence, ignition method, topography, and

containment modeling can all play a role in how a fire evolves in simulation and how much

smoke is predicted to be lofted into the atmosphere. Because of this complication, different communities often use different models deepening on the question their trying to answer. Wildland firefighters often use simple fire-spread models which can take local measurements of conditions easily and produce accurate results over short periods of time, while air-quality forecasters use even simpler methods, but over longer periods of time, assuming the fire behaves the same as the day before. Researchers using the most detailed and computationally expensive models can account for many time scales and phenomena such as boundary layer turbulence, local meteorology, fire-spread, fire-weather feedback, and fuel dynamics, but the range of interrelated factors involved often leads to complicated sources of error and uncertainty in forecasted variables.

With that in mind, this dissertation summarizes the execution and analysis of simulations from Weather Research and Forecasting Model with Fire Code (WRF-Fire) of the 2019 Williams Flats Fire and 2020 Creek Fire to better understand the drivers of large wildfires and the associated uncertainty in their modeled output. Of particular curiosity was the question of whether detailed models such as WRF-Fire can outperform simpler models in the prediction of important variables for air-quality modelers. Improving air-quality forecasting from wildfire events has the potential to improve health outcomes for millions of people and better inform organizations where operations are dependent on outdoor visibility or clean air. This work also addresses the questions of how impactful firefighting containment efforts can be, how bark beetle infestations enhance large wildfires, why pyrocumulonimbus clouds form over certain fires, what is the role of fuel moisture in modulating wildfire dynamics, how canopy burning influences the depth of smoke injection, how fuel loads can influence the depth of the fire

front, and what modeling choices lead to the most accurate simulation outputs. The breadth of this knowledge can be used to inform modeling communities in continued development and use of wildfire simulations and to better understand the behavior of wildfire dynamics under changing environmental conditions.

I find that WRF-Fire can be a valuable tool for air quality and emergency response communities when careful consideration is paid to the inputs and model configuration. When accounting for containment lines, fuel moisture maps, and high fuel loads, simulations had ~30% less error on daily burned area compared with persistence forecasting over a 5-day forecast for the Williams Flats Fire. To capture accurate smoke injection heights, the inclusion of an explicit canopy model and an increase in fuel depths to a 50 cm average in forested regions was needed. For the 2020 Creek Fire, the fuel depth in forested regions needed to be increased to 1 m to capture ~16 km injection heights and intense pyrocumulonimbus activity, likely due to bark beetle infestation and subsequent modification of the fuel structure. The circularity of the fire front, partially aided by high fuel loads, was also found to play an important role in creating deep plumes as plume buoyancy was better persevered during assent.

The dissertation of Francis Turney is approved.

Marcelo Chamecki

Alton Park Williams

Alexander Dean Hall

Pedro A. Jimenez Munoz

Pablo Saide Peralta, Committee Chair

University of California, Los Angeles

2024

TABLE OF CONTENTS

LIST OF FIGURES

LIST OF TABLES

ACKNOWLEDGEMENTS

VITA

2019   Master of Science in Atmospheric and Oceanic Science, University of California,

Los Angeles (UCLA)

2016   National Science Foundation Graduate Research Student Fellowship

2015   Bachelor of Science on Atmospheric and Oceanic Science, University of

California, Los Angeles (UCLA)

PUBLICATIONS

Krishna, M., Saide, P.E., Ye, X., Turney, F., Hair, J., Fenn, M.A. and Shingler, T., 2023. Evaluation of Wildfire Plume Injection Heights Estimated from Operational Weather Radar Observations using Airborne Lidar Retrievals. *Authorea Preprints*.

Saide, P.E., Krishna, M., Ye, X., Thapa, L.H., Turney, F., Howes, C. and Schmidt, C.C., 2023. Estimating fire radiative power using weather radar products for wildfires. *Geophysical Research Letters*, *50*(21), p.e2023GL104824.

Turney, F.A., Saide, P.E., Jimenez Munoz, P.A., Muñoz-Esparza, D., Hyer, E.J., Peterson, D.A., Frediani, M.E., Juliano, T.W., DeCastro, A.L., Kosović, B. and Ye, X., 2023. Sensitivity of Burned Area and Fire Radiative Power Predictions to Containment Efforts, Fuel Density, and Fuel Moisture Using WRF-Fire. *Journal of Geophysical Research: Atmospheres*, *128*(18), p.e2023JD038873.

Comola, F., Kok, J.F., Lora, J.M., Cohanim, K., Yu, X., He, C., McGuiggan, P., Hörst, S.M. and Turney, F., 2022. Titan's prevailing circulation might drive highly intermittent, yet significant sediment transport. *Geophysical Research Letters*, *49*(7), p.e2022GL097913.

Chapter 1

Introduction

1.1 Science Questions and Forecasting

Wildfires are a natural and net beneficial aspect in many eco-systems, but climate change and historical fire suppression techniques have created more devastating and frequent fires (Halofsky et al., 2020) potentially changing the overall impact of these phenomena on the environment. This paradigm has prompted many scientific questions and forecasting challenges aimed at better understanding, predicting, and managing wildfire behavior. I focused this dissertation on a few broad questions that surrounded this larger subset of goals and questions; how accurate are wildfire forecasting models, and what practical steps can I take to improve their skill? Within that aim, I focus on the skill of forecastable variables that are most important to air quality modeling, although variables relevant to emergency response are also explored. Daily burned area is an important input for many simple emission models (Ye et al., 2021) and FRP has been found to correlate well with emissions on short time scales (Wooster, 2002). Both can be observed from satellite, making them relatively simple inputs to regional meteorological forecasts that account for aerosol transport and good candidates for observational comparisons. In the vertical dimension, the smoke injection height, or the depth at which smoke is lofted from the fire is also important for air quality models, as well as the fraction of smoke lofted above the atmospheric boundary layer (ABL) (Ye et al., 2021, 2022). These

variables control the extent and nature of smoke transport downwind as smoke mixes vertically due to atmospheric phenomena and gravitationally settles over time. The timing of emission output is also important to air quality forecasting with wildfire diurnal cycles and boundary layer dynamics possessing significant variability (Ye et al., 2021). Co-location of forecasted fire-spread with observation is an important variable for emergency response communities but is also relevant to air quality forecasting in simulating the burning of correct fuels. Assessment of these metrics guided our analysis, but many science questions were addressed along the way.

1.2 Case Studies

Here I investigate the skill of simulation output from two real fires. The 2019 Williams Flats Fire was a medium-large wildfire (~45k acres) which spawned several ~10 km high pyrocumulonimbus clouds (pyroCbs) and was one of the most intense fires sampled during the 2019 NASA/NOAA field campaign FIREX-AQ. As such, there is wealth of measurements and understanding about the circumstances that occurred. The 2020 Creek Fire was the second largest single ignition fire in California history (~379k acre) and spawned massive ~16 km pyroCbs that injected smoke into the stratosphere and led to significant smoke transport across much of California. The region was known to have extensive beetle kill mortality that likely contributed to the severity of the fire, although the extent to which that played an impact is still uncertain. These fires contrast in many important ways, were observed in detail, and displayed a wide range of phenomena making them ideal choices for study.

1.3 Chapter Outlines

Starting with the 2019 Williams Flats Fire in Chapter 2, I compare predictions of burned area and fire radiative power (FRP) from the coupled weather/fire-spread model WRF-Fire (Weather and Research Forecasting Tool with fire code) against simpler methods typically used in air quality forecasting. Using a novel re-gridding scheme, I compare WRF-Fire's FRP to geostationary satellite data at 1-hour temporal resolution. I also evaluate WRF-Fire's daily burned area time series against high-resolution imaging from the National Infrared Operations (NIROPS) aircraft data. I show that for this fire, accounting for containment efforts made the biggest difference in achieving accurate results for daily area burned predictions. When incorporating containment lines, fuel loading increases, and fuel moisture observations into the model, the error in average daily burned area was 30% lower than persistence forecasting over a five-day forecast. Prescribed diurnal cycles and those resolved by WRF-Fire simulations show a phase offset of at least an hour ahead of simulations, likely indicating the need for dynamic fuel moisture schemes. I show that with proper configuration and input datasets, coupled weather/fire-spread modeling has the potential to improve smoke emission forecasts for medium-large wildfires.

In Chapter 3 I examine the vertical dimension of Chapter 2 Williams Flats Fire simulations by comparing predictions of smoke injection height and FRP to radar, lidar, and satellite observations. For my best simulations, ~9 km pyroCbs were formed at roughly the right time as observed ~10 km pyroCbs. Smoke injection heights were most accurate when using a newly developed canopy code (Shamsaei et al., 2023) and increasing fuel depth in forested

regions to 50 cm. Large fuel depths were needed to counteract the slow fire spread from increased fuel loadings in Chapter 2 and to achieve realistic smoke injection heights, but this increase caused FRP to be significantly overpredicted. I show that several factors likely played a role in this error including convective available potential energy (CAPE), grid spacing, and canopy burning threshold. I also find that the fraction of smoke injected above the boundary reached slightly above 80% in our best simulations in contrast with higher ratios in observation, but closer to observation than plume rise models typically used in air quality forecasting models.

Switching to the 2020 Creek Fire in Chapter 4, I examine deep pyroCb activity in WRF-Fire and the potential role bark beetle played in generation of extreme wildfire activity. Simulated pyroCbs reach roughly the right injection heights (~16 km) at the right times for simulations configured with a canopy burning model, fuel depth increases up to 1 m in forested regions (to account for bark beetle), and 2014 fuel category data from LANDFIRE. Smoke injection height to FRP ratio was also reasonable for this fire as well, validating the need for increased fuel depths and implicating bark beetle as the reason. For this fire, I found that the circularity of the main fire front, perhaps driven by high fuel loadings, was the major factor impacting smoke injection height to FRP ratio. Bark beetle is thus implicated here as not only causing a hotter and bigger fire, but possibly one with deeper, more circular fire fronts capable of injecting deeper into the atmosphere. Divergence at the smoke cloud top was calculated and compared to maximum updraft speed and observation for use as a potential satellite product.

Chapter 2

Sensitivity of Burned Area and Fire Radiative Power Predictions to Containment Efforts, Fuel Density, and Fuel Moisture Using WRF-Fire [Turney et al., 2023]

2.1 Introduction

Large wildfires have become increasingly common in recent years (Abatzoglou & Williams, 2016) and their immediate destructive impacts are often followed by negative effects on regional air quality, public health, and the earth system. These problems have been exacerbated by the effects of climate change, historical containment efforts, and water usage, which have made fires more intense and more frequent, burning tree crowns more often and altering ecosystem succession dynamics (Halofsky et al., 2020). In turn, efforts to improve forest management, emergency response, and forecasting of air quality have the potential to reduce the negative impact of large wildfires on populations and the environment in a warming climate (McCaffrey et al., 2020). Air quality forecasting and emergency response efforts are commonly aided by models that predict wildfire growth despite considerable uncertainty

associated with their configurations and inputs. Studies evaluating the accuracy and computational costs of wildfire models under different configurations can thus be crucial in informing communities in choosing modeling solutions.

Dynamic wildfire models come in a variety of architectures, but only a few direct comparison studies exist (Dobrinkova & Dobrinkov, 2014; Graff et al., 2020). These models generally fall into two classes, coupled or non-coupled, depending on whether heat from the wildfire influences the atmospheric flow or not (Bakhshaii & Johnson, 2019). Non-coupled models such as FARSITE (Finney, 1998), Prometheus (C. Tymstra et al., 2010), and BEHAVE (Andrews, 2014)), are often used to aid firefighting efforts because of their computational speed and flexibility in inputting meteorological data from simulation or field, but these models are limited by their inability to resolve fire-weather interactions. Coupled models such as WRF-Fire (Coen et al., 2013), WRF-SFIRE (A. K. Kochanski et al., 2013), and CAWFE (Clark et al., 2004; Coen, 2005) are now widely used by researchers to better understand the mechanisms behind and interactions between wildfire spread, atmospheric turbulence, fire-weather, and smoke emission, but they are used less often for operational purposes because of longer computing times, complexity of configurations, and difficulty of validating the real-world outputs of these models. There have been recent efforts to gear coupled models towards operational forecasting (J. Mandel et al., 2014; Jimenez et al., 2018; Kochanski et al., 2021; Wang et al., 2022), but direct comparisons between coupled models and simpler approaches are rare in the scientific literature (Dobrinkova & Dobrinkov, 2014; Wang et al., 2022). Additionally, multiple studies have been performed to assess the sensitivity of fire-spread modeling to a variety of factors including fuel moisture representation (Jolly, 2007), ignition location and timing (Zinger

et al, 2020) and ignition ahead of the fire line by spotting (Frediani et al, 2021). However, I am not aware of work exploring observed containment efforts in the context of coupled fire-weather modeling, and more realistic treatments of heat release due to canopy burning are explored in Chapter 3 (Shamsaei et al., 2023).

Despite the widely understood interactions between fire and local weather, operational air quality forecast models still often rely on "persistence forecasting", in which daily burned area from the previous day is assumed to repeat and thus forecast emissions on the subsequent days (Ye et al., 2021). Persistence forecasts fail to account for the dynamic nature of wildfires, and their performance will be especially poor on days of large fire growth or decline (Ye et al., 2021). Although several tools have been explored to overcome the deficiencies of persistence forecasting (Graff et al., 2020; Peterson, et al., 2013; Preisler & Westerling, 2007), persistence forecasting remains a *de facto* standard for smoke forecasting models. Along with persistence in burned area, Fire Radiative Power (FRP), or the radiant energy released by a fire, is also predicted as a function of the previous days burned area in models such as HRRR-Smoke (Ahmadov et al., 2017) and NCAR WRF-CHEM (Kumar et al., 2021). FRP has been found to be highly correlated with smoke emissions from wildfires (Wiggins et al., 2020), and important to modeling smoke injection heights (Ye et al., 2021), thus making another great benchmark for WRF-Fire comparisons.

Here I evaluate a case-study set of simulations produced by the coupled fire-spread model WRF-Fire (Coen et al., 2013; Jan Mandel et al., 2011; Muñoz-Esparza et al., 2018) to better understand the potential of coupled models to predict daily burned area and FRP. Persistence and smoke emission models are used as benchmarks and configurations are varied

within the set to reflect potential operational considerations. WRF-Fire can capture realistic fire growth, regional meteorology, and Large Eddy Simulation (LES) scale fire induced weather patterns all at once with potentially reasonable computing time, making it a prime candidate for improvement over simpler methods.

I focus this study on the 2019 Williams Flats Fire, as it was the most intense fire sampled during the 2019 NASA/NOAA Fire Influence on Regional to Global Environments and Air Quality (FIREX-AQ) field campaign. The Williams Flats Fire was ignited by lightning and fuel-driven for the first few days before exploding in growth after the breakdown of an upper-level high pressure ridge and subsequent period of enhanced wind speeds and instability (Peterson et al., 2022). There were significant efforts to contain the fire and protect surrounding buildings which seem to have succeeded in cutting the fire off in the southern and western flank. In addition, a pyrocumulonimbus (pyroCb) cloud developed during the final days of the fire (Peterson et al., 2022). I perform WRF-Fire simulations starting from both a point source representing ignition, as well as from perimeter observations. Simulations are run for multiple days, and initialization at different days is compared. I then analyze WRF-Fire's forecasting skill under a variety of sensitivities that the end user has control over including horizontal resolution, fuel moisture, fuel density, ignition method, and inclusion of containment data.

2.2 Methods

The methods are divided into groups either describing WRF-Fire (Section 2.2.1 – 2.2.4) or comparisons with other models and observations (Section 2.2.5). I discuss WRF's background, meteorological forcing, and resolution in Section 2.2.1, input data and preprocessing in Section 2.2.2, and fire-code implementation in Section 2.2.3. My configuration choices and motivations are detailed in Section 2.4 before discussing comparisons to observations and benchmarks in Section 2.2.5.

2.2.1 Weather Model (WRF)

All my simulations have WRF (Weather Research and Forecasting tool) at their core (Skamarock et al., 2019), a long-standing community model capable of simulating a wide range of atmospheric phenomena from global climate to cloud microphysics. I take advantage of WRF's nested domain configuration options, to feed synoptic meteorological data through a coarse-resolution domain and into a high-resolution LES domain where the fire code runs. This form of mesh refinement is a common practice in WRF and allows us to resolve several scales of meteorology at once.

Our WRF simulations use a two-domain configuration going from 1-km resolution on the outer domain to 200 m on the inner domain; I include only one way coupling from the outer to the inner domain. Using a 50 km by 50 km inner domain and 200 km by 200 km outer domain, together with the meteorological boundary conditions from 3 km HRRR forecasts, WRF can resolve synoptic, mesoscale, and boundary layer features for many days into the simulation.

Mesoscale/synoptic meteorology is a well-known driver of wildfire behavior, with surface wind events commonly linked to the breakdown of the upper-level ridge or passing of synoptic lows and fronts (Tymstra et al., 2021).

I choose 200 m for the base LES horizontal resolution because at the scale of medium-large wildfires (~50 k acres), it allows us to run two to three times as fast as reality. Although 200 m is in the gray zone (aka terra incognita), or the range at which PBL schemes and LES can both underperform (Juliano et al., 2022; Rai et al., 2019; Wyngaard, 2004), my early results indicated that increasing the resolution to 100 m grid spacing did not improve simulations significantly enough to warrant the extra computational time (see Supplemental Figures A.1 and A.2).

It's well known that turbulence plays a significant role in the way weather and wildfire activity interact (Supplemental Section A.2). Here I simulate some of those important dynamics through WRF's LES configuration. In my inner domain, the Planetary Boundary Layer (PBL) scheme is turned off and a 3D turbulent kinetic energy (TKE)-based sub-grid scale (SGS) scheme is used to predict eddy diffusivity (Deardorff, 1980).

2.2.2 Input Data (WPS)

For all simulations, I use the WRF Pre-processing System (WPS) to interpolate input data and format the data to be read by WRF. Both domains require interpolation of meteorological data, topography, and land-surface data, while data such as fuel category, fuel density, and fuel moisture are interpreted to the fire model sub-grid.

Our simulations run with initial and boundary conditions from the High-Resolution Rapid

Refresh (HRRR) model, which are 3 km resolution hourly updated instances of WRF from NOAA

that run over the United States (Benjamin et al., 2016). HRRR assimilates data from satellite,

aircraft, and many other observations and is forecasted out up to 48 hours in advance at every

six-hour forecast, and 18 hours in advance otherwise. Here I always use the 0-hour forecast for

initial and boundary conditions which are the closest to observation. Although there are other

meteorological products with similar resolutions that would be suitable for WRF-Fire (NAM 3

KM CONUS) I am not aware of a public archive for them, and other meteorological forecasting

data available are too coarse to use in a single nested domain study. The impact of using either

coarser or non-archived meteorological input data is left to future studies.

While my outer domain uses default topography to simulate mesoscale phenomena,

turbulence in an LES domain needs a roughness element or initial disturbance to be spun up

realistically. A fully spun up Atmospheric Boundary Layer (ABL) may require long fetches over

steep topography or continuous perturbation methods (Lee et al., 2019) so to trip turbulence

here, I use high-resolution topography and a roughly 20 km fetch in all directions. Although

confirmation of fully developed turbulence is beyond the scope of this study, key turbulent

structures and interactions appear in my simulations (Supplemental Section A.1; Supplemental

Figures A.3-A.5).

Our 30 m resolution topographic dataset comes from the LANDFIRE archive (Landscape

Fire and Resource Management Planning Tools, (Ryan & Opperman, 2013)) where data is

available over the contiguous United States (Figure 2.1). The 30 m topographic data is

interpolated to the 200 m LES grid and either smoothed slightly using the WPS native

smoothing found in *GEOGRID.TBL or* spectrally smoothed (Kosovic, 2021) to obtain speed-ups

for possible operational purposes. Smoother terrain lowers vertical wind velocities and reduces

the chance of winds being advected beyond a cell's length (De Moura & Kubrusly, 2013). This

allows for numerical stability on larger time steps and computational speeds of up to six times

faster than reality for this fire (Section 2.2.4).

Another consideration in modeling with WRF is the use of land-surface models. I

selected the highest resolution land cover dataset intrinsic to the general WRF static input data,

a 9 second NLCD (National Land Cover Database) data set, which is specified during the pre-

processing configuration, on the *namelist.wps* file:

geog_data_res = 'nlcd2006_9s+30s','3s+nlcd2006_9s+30s',

Fuel category is central to WRF-Fire's burning scheme in separating types of fuels and

their propensity to burn and spread. I gather fuel category data from the LANDFIRE website

(Ryan & Opperman, 2013), which uses the Fuel Characteristic Classification System (FCCS) and

separates fuel loads into low, medium, or high load categories. I performed my simulations

using the 2016 version of the FCCS classification using either the 13-category (Anderson, 1981)

or 40-category data (Scott, 2005). A number of corresponding coefficients that influence fire-

spread are listed in the configuration file *namelist.fire (*see Open Research*),* including fuel

density, fuel depth, and weighting coefficients for mass loss rate curves.

Dry fuels can be a significant driver of wildfire behavior and smoke emission, and to

better understand model sensitivity to fuel moisture, I incorporate recently derived fuel

moisture satellite products intro WRF-Fire as static input conditions (Kosović et al., 2020). Here

I use the WRF-Fire code developed for Colorado Fire Prediction System (CO-FPS) which allows

fuel moisture content (FMC) maps from the Moderate Resolution Imaging Spectroradiometer

(MODIS) instruments Terra and Aqua to be ingested into my simulations at 1 km resolution

(Kosović et al., 2020). Fuel moisture maps (Figure 2.1c and 2.1d) are static for each simulation

and are usually retrieved around 12 hours before the start of my fire simulations. There are

dead and live fuel moisture maps, and in the CO-FPS model live fuel can both burn and be

converted to dead fuel. The dead FMC maps that I use are typically lower in FMC (6.5% mean

value for Figure 2c than what WRF prescribes as its default value (8%) and as dead fuels make

up the bulk of the fire-spread along the ground, I generally get faster fire spreads when using

these satellite FMC products as inputs.
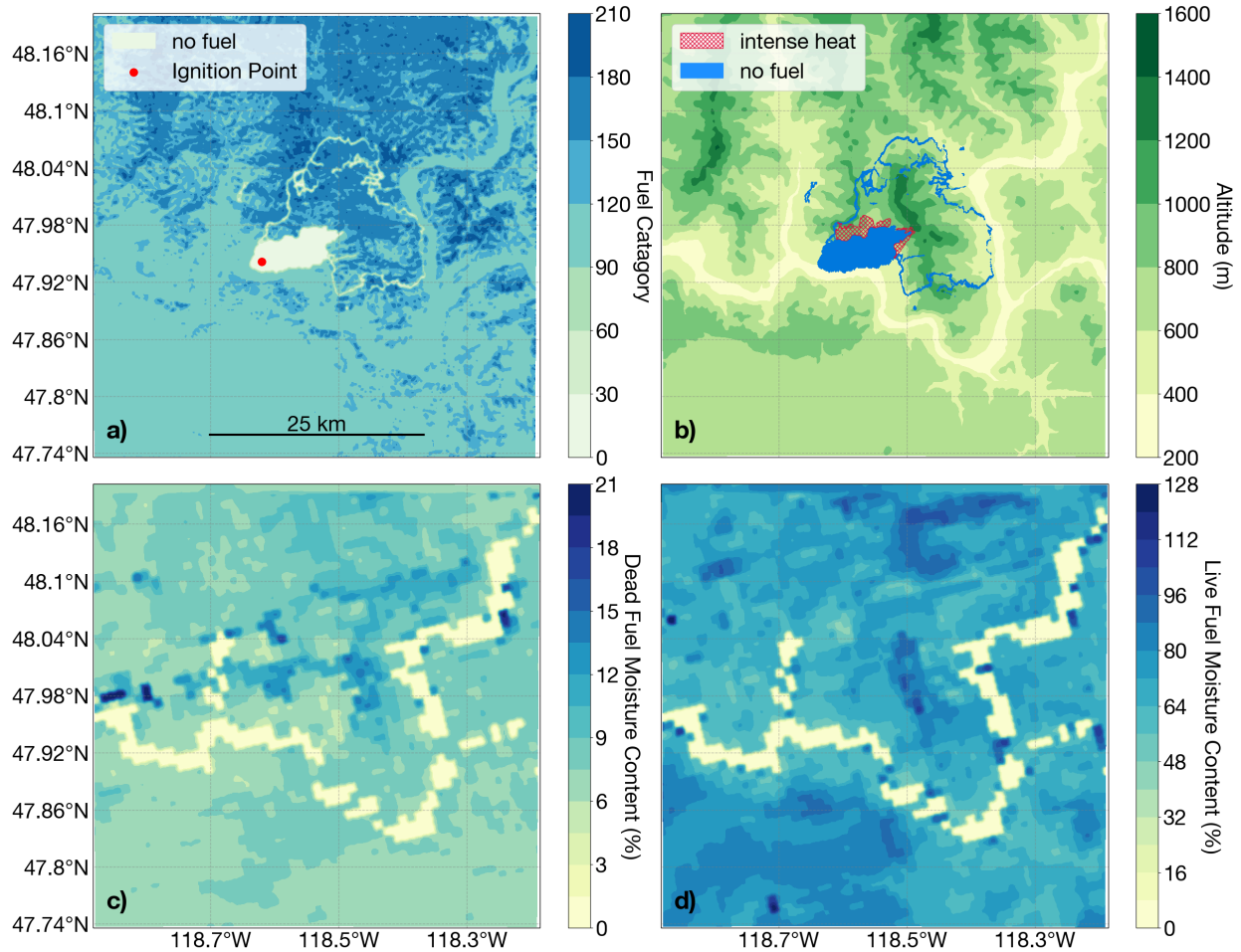
Figure 2.1. Inputs for WRF-Fire simulations of the 2019 Williams Flats Fire ignited just before August 4th. a), fuel categories represented here include dry grass (102), dry timber-shrub (165), long-needle litter (188), and no fuel (14, light green, see section 2.2.3) from the 40-category dataset (Scott 2005). Ignition point is chosen as approximately the middle of the first VIIRS retrieval (see Figure 2.2). b), No-fuel sections of fuel category are either the scattered and no heat areas at the interior of the fire or containment lines. The intense heat region in hatched red, taken from NIROPS the night of August 3rd, is the only region which is set to burn at the start of simulation.

2.2.3 Fire-Spread Model (WRF-Fire)

At the smallest scales of my simulations is the fire-spread model, a sub-grid semi-

empirical algorithm with the Rothermel equations at its core (Rothermel, 1972). Like many other fire-spread models the rate-of-spread (ROS) is a function of wind speed, fuel moisture, and slope of the topography with scaling effects from fuel properties. Fuel combustion rate scaling factors set in the configuration file *namelist.fire* modulate these equations and thus influence the ROS and heat release of the model. Inputs are interpolated, combustion is parameterized, and the fire front is propagated on my LES domain's sub-grid with a grid spacing of 50 m (Coen et al., 2013).

The propagating fire line is tracked by an improved level-set function which represents a line as the intersection of a signed three-dimensional curve and a plane (Muñoz-Esparza et al., 2018). This allows for fire lines to split and rejoin in natural ways and is generally considered more accurate than other common methods for representing fire line such as Huygen's elliptical algorithm (Anderson et al., 1982). The signed nature of the curve, negative on the inside of the fire, is a crucial part of propagation, but over time the function can accumulate error, lose its signed nature, and yield inaccurate results (Chopp, 1991; Sussman et al., 1994). A reinitialization of the level-set function is often implemented to account for this and the number of iterations of the algorithm can thus act as an important numerical parameter. WRF-Fire recently received an update implementing high-order numerical methods to advance the level-set function and re-initialization as part of the fire-spread model (Muñoz-Esparza et al., 2018) which I use in this work. A dependence of the re-initialization on the LES time step was discovered in this work and changes were made to the "FIRE_LSM_REINIT_ITER" parameter to account for this (Supplemental Section A.2). For this study, I find 3.3 iterations of re-initialization per second to be optimal.

WRF-Fire can be ignited by points or lines but over time may deviate significantly from observation. In addition, after a long integration (~>2 days) it becomes impractical to start from point ignitions. To overcome this, WRF-Fire can also be ignited from an observed perimeter, which can help realign a simulation with observations and reduce the computational time compared to simulating the fire progression from a point/line. Here I use the National Infrared Operations (NIROPS) aircraft retrievals, flown at most once a day on large wildfires, which have high spatial resolution and resolve regions of high intensity, scattered heat, and no heat. Within the fire perimeter, negative values are written into WRF's Level-Set Function (LFN) history variable to represent burning regions. In the scattered and no heat regions within the perimeter, I remove the fuel so that no burning over already burnt fuels occurs.

Currently, WRF-Fire only considers the burning of surface fuels and thus can underpredict heat flux where crown fires have occurred. Here I implement a modification of fuel densities (kg/m^2) to make up for the missing fuel load and subsequent heat output when burnt. For the 13-category fuel category data, I replace fuel densities with their closest corresponding category value from a list of average fuel densities for wildfires over three major fuel types in FINN (Fire INventory from NCAR, (Wiedinmyer et al., 2011) corresponding to grasslands (0.98 kg/m^2), savannah (5.7 kg/m^2) and temperate forest (10.49 kg/m^2). Other fuel loading models and observations in the region show a wide range of estimates with FINN values falling in between and getting closer to observations than most (Drury et al. 2014). In addition, the data from FINN represents average fuel densities burned for different fuel categories, which includes canopy burning, making it an ideal choice for an implicit model which aims to correct fuel density burning on average rather than explicitly accounting for canopy fires. For the 41

category fuel category data, I group the categories into the three major FINN categories and then normalize their fuel density, so the average of the group is equal to the corresponding FINN value, thus retaining the relative variability for categories within each group (Figure 2.1, Supplemental Table A.1). Both methods yield significant improvements in heat output when compared to satellite retrieved FRP (Section 2.3.3). A caveat of this implementation is that it assumes all fuel is on the surface and thus could affect fire spread. However, I kept this implementation as this sensitivity has not been assessed in previous work and it allowed for increased heat release without having to develop a canopy burning parameterization.

The National Interagency Fire Center (NIFC) has a repository through ArcGIS online for historical wildfire containment data that I use in this work. Here I take completed containment lines from the "EventLine2019" operational data archive and filter them to keep completed dozer lines, completed hand lines, completed lines, and roads as completed lines for the Williams Flats Fire. The dates of completion for the containment lines appear to be inaccurate or incomplete at this time, as many lines are listed as being completed well after the fire burned past them. Handwritten notes on the efforts exist but to my knowledge are only available to fire crew. With that in mind, I use this data in an ideal sense, removing fuel along every containment line available for the fire from the very beginning as if all containment lines were constructed before the fire reached them (Figure 2.1a and 2.1b)). This assumption is likely valid given that crews would not complete a line after a fire burned past. I additionally compared containment lines to road maps and found most lines are on roads, possibly indicating that lines were established well ahead of time. However, using containment lines with accurate dates would possibly yield different simulation results, likely burning past final

containment perimeters more when simulations overestimate fire spread. At this time, I am not aware of real-time data available for such containment efforts so simulations that use this method are only meant to show the difference that modeling containment could make in WRF-Fire in a best-case scenario.

2.2.4 Model Configurations Tested

Because there were so many variables affecting fire-spread in any given simulation, I selected a few key configurations from the above-mentioned methods to test the model's sensitivity to important factors by sequentially increasing the realism of the simulations. I tested 6 different configurations: Base, Crown, FMC, Smooth-FMC, Contain-FMC and Contain (Table 2.1). All simulations share outer domain settings, domain boundaries, sub-grid turbulence parameterizations, standard meteorology schemes, HRRR input meteorology, and 9 second land category data. I take as ***Base*** simulation what I consider to be closer to default settings, 200 m horizontal resolution, 13-category fuel data, and homogenous fuel moisture supplied in the default version of *namelist.fire* of 0.08 kg/kg. To represent a fire that has crown burning, I alter the base simulation by scaling up the 13-category fuel density (Section 2.2.3, Supplemental Table A.1) in ***Crown*** simulations. I add FMC maps from NCAR for a ***FMC*** simulation, although I also use scaled 41-category fuel category data to match developer configurations and capture the most accurate representation of heat release (Section 2.2.2, Supplemental Table A.1). For a less computationally intensive model I alter the Fuel Moisture simulation by spectrally smoothing topography to 275 m (Section 2.2.2) which I label ***Smooth-FMC***. In my ***Contain-FMC*** sensitivity, the FMC simulation is used but all the fuel category cells

overlapping with containment lines from containment lines are set to the zero-fuel category to
simulate an ideal containment scenario (Section 2.2.3). My final sensitivity **Contain** takes the
contain simulation and turns off the fuel moisture scheme so I can analyze the effect of my
ideal containment scenario without FMC. I also construct an **Ensemble** average forecast from
the FMC and Crown sensitivities as they are usually the furthest spread apart in predictions and
feasible for use in an operational setting.

	200m Topo	275m Smooth Topo	Fuel Moisture	Crown Adjust	Containment
Base	✓				
Crown	✓			✓	
FMC	✓		✓	✓	
Smooth-FMC		✓	✓	✓	
Contain-FMC	✓		✓	✓	✓
Contain	✓			✓	✓

Table 2.1. Simulation Configurations. Differences between simulations' configuration options with check
marks indicating which features (columns) and used in which configurations (rows). Topo is short for
topography, and explanations for configuration options are described in Section 2.2.4.

2.2.5 Observations and Benchmarks

Active fire products from NOAA's Geostationary Operational Environmental Satellites (GOES) Advanced Baseline Imager (ABI) produce fire count and Fire Radiative Power (FRP) at 5-minute intervals using the Wildfire Automated Biomass Burning Algorithm (WFABBA) algorithm (Schmidt, 2020). These GOES-17 fire pixels were filtered similarly as in previous work (Li et al., 2022) based on flag and only kept if the flag was for a processed fire pixel (10), high-probability fire pixel (13), or medium probability fire pixel (14) excluding cloudy, saturated, and low probability fire pixels. GOES data was not parallax corrected, but aggregated over a box where pixels corresponding to the Williams Flats fire are still contained (Lat 47.90-48.05, Lon -118.67--118.3) as done in previous work (Ye et al., 2021, Berman et al., 2023). Here I use data from GOES-17 to evaluate wildfire simulations at higher-temporal resolution than any comparison that I am aware of in the literature. To directly compare WRF-Fire and GOES-17 FRP, WRF-Fire output is re-gridded to the GOES-17 grid by summing up heat fluxes inside GOES-17 cells (2 km horizontal resolution). Comparing cells that are on fire in WRF-Fire vs GOES-17 on the GOES-17 grid gives us a unique comparison in fire count, which is the number of pixels deemed on fire by GOES-17 or assumed on fire if GOES-17 could somehow observe my simulation (i.e., Equivalent Fire Counts). In addition, summing up the total radiant power over all cells inside the fire domain (calculation described below) gives us a measure of a simulated fire's FRP. Both FRP and Fire Count are processed on 5-minute windows and then averaged over each hour.

These comparisons rely on a few assumptions about the amount of radiation from the fire that would realistically be observed by GOES-17. Firstly, I assume that only 20.5% of the

total heat released by WRF-Fire (Sensible + Latent) is in the form of radiation that can be observed by satellite. This ratio is an average of the ideal range of radiant fraction measured in Johnston et al. (2017), which is notably at the higher range of estimates compared to previous studies (Freeborn et al., 2008) but not outside classical estimates (Byram, 1959). The rest of the heat is assumed to be partitioned into latent, convective, and conductive heat. In reality, the exact ratio is likely more variable and dependent on at least sensor angle (Johnston et al., 2017), wind speed, fuel depth, fuel moisture, and fuel category (Frankman et al., 2012), but I use a constant given the considerable uncertainty in those relationships in the literature. Secondly, I assume that GOES-17 has a minimum FRP per pixel that it can detect, below which the pixel will not be considered on fire. I take this minimum value to be 25 MW per pixel based on the similar resolution between GOES-17 and MODIS Aqua's day edge, where the exponential drop off in FRP density is around 25 MW (D. Peterson, et al., 2013). More recent studies (Xu et al. 2021; Li et al. 2020) found thresholds of 30 MW- 35 MW for GOES retrievals, but differences in FRP and Fire-count were nearly imperceptible across this range. A snapshot of WRF-Fire's equivalent fire counts vs GOES-17's fire counts shows that the algorithm produces a realistic pixel distribution (Supplemental Figure A.7). In addition, while fire counts shown in Figure 2.8 show reasonable agreement after thresholding, choosing a minimum pixel power threshold was found to not significantly affect FRP results.

I used several other datasets to evaluate WRF-Fire against. The Visible Infrared Imaging Radiometer Suite (VIIRS) is a sensor on board the S-NPP satellite that usually samples fires twice a day (day and night overpasses) and produces fire hotspot pixels and FRP at a nadir resolution of 375 m (Schroeder & Giglio, 2017). Fire hotspots were aggregated to estimate burned area

(Berman et al., 2023) which I use in cases of missing NIROPS flights along with a VIIRS FRP

product that was used to evaluate WRF-Fire equivalent FRP. I also compared WRF-Fire FRP to

the MODIS/ASTER Airborne Simulator (MASTER), an infrared sensor flown on the DC-8 aircraft

during FIREX-AQ from which an FRP estimate can be derived as done in previous work (Thapa et

al., 2022).

Assumptions commonly used in smoke forecasting are used here as benchmarking

metrics. I compare WRF-Fire predictions of daily burned area to a persistence forecast

computed using the difference between NIROPS perimeters on Day 0 and the previous day.

When NIROPS is not available I used a VIIRS based estimate (Berman et al., 2023). HRRR-Smoke

(Ahmadov et al., 2017) and NCAR WRF-CHEM (Kumar et al., 2021) are smoke forecasting

models which have fixed diurnal cycles that I compare WRF-Fire diurnal activity to. The diurnal

cycles are normalized by the magnitude of the sum of FRP values (X. Ye et al., 2019; Xinxin Ye et

al., 2021).

Although there are no high-quality observations of surface meteorological conditions

within my second domain, comparisons between nearby US Forest Service Remote Automatic

Weather Stations (RAWS) and WRF meteorological variables provided us some insight into my

simulations accuracy in simulating the weather events that influenced the Williams Flats Fire.

The Wellpinit RAWS stations is ~35 km from the Williams Flats Fire so it provides basic

meteorological diagnostics for the region. Supplementary figures 8 and 9 show the timing and

magnitude of WRF winds are likely reasonable although perhaps slightly underpredicted. Air

temperature and Relative Humidity (RH) also show reasonable magnitude and temporal cycles.

Although only one WRF-Fire simulation is shown, it's representative of the other simulations and days.

Computational times over this 50 km x 50 km domain with 400 cores were six times faster than reality when spectrally smoothed, and three times faster otherwise, but consistent results depend on adjusting the number of re-initialization iterations if the time step is reduced.

2.3 Results

2.3.1 Burned Area Perimeters

Burned area perimeters are plotted for my simulations at times corresponding to NIROPS perimeter products or VIIRS retrievals (Figures 2.2, 2.3, Supplemental Figure A.11). I find that, especially in point-ignited simulations, spatial differences between WRF-Fire and NIROPS's burned area perimeters generally increase over time as I might expect from a stochastic weather forecast (Figure 2.2). As time passes, errors compounded on each other, with fires continuously spreading along fronts that were contained (Figure 2.1b)) or continuously stagnating in directions that should have burned more quickly (Figure 2.2). Simulations often burned too much along the grassy southern and western flanks where containment was effective and not enough into the forested mountains where containment lines were sparse (Figure 2.1b)). Inclusion of containment lines yielded better perimeters in almost all cases, although in the case of a point ignition the fire seemed to make its way

through the containment perimeter, likely either because of gap in containment data or a river

that is not well represented in the fuel category data (Figure 2.2).

When igniting WRF-Fire from an observed fire perimeter (i.e., later into the fire), many

of these problems were minimized (Figure 2.3). Often, the already burned interiors blocked fire

from spreading back into already burned areas, forcing spread in the right direction. Also,

because the fire burn towards a large river bend in the south and east, simulations ignited or

burning later into the fire were trapped within these natural boundaries.
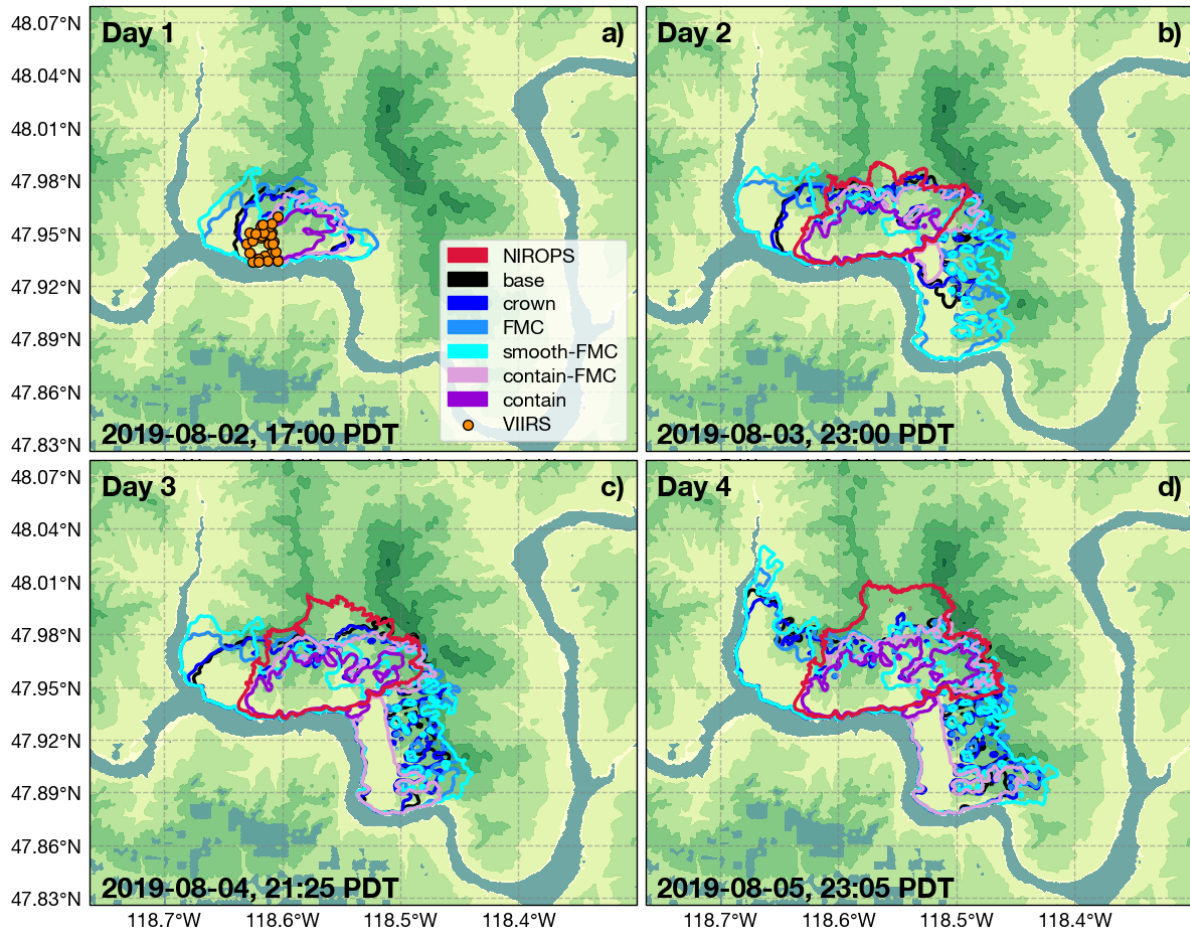
Figure 2.2. The first four days of point ignited simulations for the 2019 Williams Flats Fire. For a breakdown of sensitivities see section 2.2.4 and/or Table 1.1. **VIIRS** hot spots are 375 m resolution satellite products that indicate the presence of fire and pass near any location usually twice per day. The simulations were ignited at 3 AM PDT, near the time of first report, at the ignition point shown in Figure 2.1.
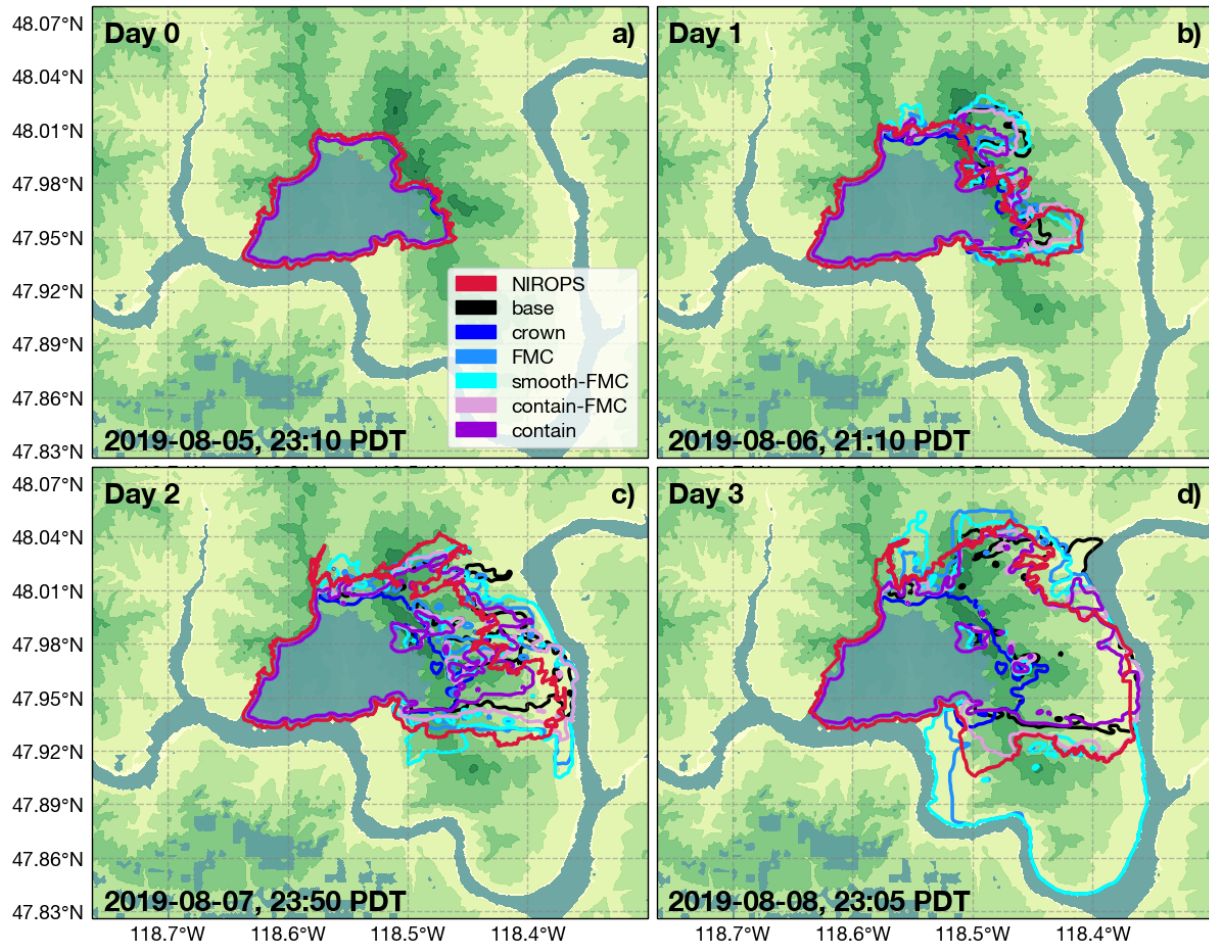
Figure 2.3. Three-day forecasts of WRF-Fire's real perimeter ignition simulations, starting at 23:10 PDT on August 5th, 2019, for the Williams Flats Fire. See Section 2.2.4 and/or Table 2.1 for a breakdown of different simulations. The gray blue color of the river that also extends into the center of the fire is the no-fuel region, here representing burnt out fire interiors, water, and urban or agricultural non-fuels.

2.3.2 Total Burned Area and Daily Burned Area

From these perimeters I calculate a total burned area time series for WRF-Fire simulations to compare against observed burned area estimates (Figures 2.4a and 2.5a). I found the most consistent way of computing burned area from WRF-Fire was to input the wildfire

perimeters from my spatial plots (e.g., Figures 2.2 and 2.3) into a polygon area calculation

scheme using an equal area projection (see Open Research). Differences in initial burned area

between NIROPS and WRF-Fire when starting the fire from a real perimeter (e.g., 23 PT on

August 5th in Figures 2.3 and 2.5) can be attributed to the way the level-set function is written

into the inputs as a distance transform that results in slightly positive values close to and inside

the perimeter. This is likely a relatively small factor in the prediction skill overall.

NIROPS perimeters are taken once every night, if flight conditions are favorable, when

the fire has mostly finished burning, so I take differences in consecutive NIROPS perimeters as

daily burned area observations. I also take differences in WRF-Fire permitters over NIROPS

retrieval windows when calculating daily burned area for WRF-Fire (Figures 2.4b and 2.5b).

Using the Root Mean Squared Error (RMSE) between daily burned area predictions and NIROPS

observations I calculate and plot the Skill Score as defined by:

$$Skill\ Score\ =\ 1\ -\ \frac{RMSE(WRF)}{RMSE(persistence)} \qquad \text{(Eq. 2.1)}$$

The skill score is computed for all simulation days and sensitivities (Figure 2.6), positive

values representing fractional improvement over persistence and 0 or below indicating reduced

skill. Because this is a single fire with just five different ignition days, data quantity and

therefore generalizations are limited, but the trends appear consistent and explainable for this

study.

In general, I see a significant overestimation of burned area in my time series unless fuel

density was increased or containment modeling was used (Figures 2.4 and 2.5). I note that

simulations without containment at times bound the observations (Figure 2.5 and

Supplemental Figure A.14) and thus their ensemble average has the potential to predict burned

area progression better than those individual models. Here I took the *ensemble* product to be

the average of the *crown* and *FMC* configurations because they often display opposite

behaviors, underestimating and overestimating respectively. Including only two models in the

ensemble average also allows for the potential for reasonable computational time of the

average in an operational setting. I find that on average, the ensemble forecast outperforms all

other non-containment configurations in predicting daily burned area (Figure 2.6).

I find that simulations which consider containment modeling (*contain, contain-FMC)*

have higher skill than persistence for the first few forecast days, but which decreases over time

(Figure 2.6). Predictions of daily burned area in my *contain-FMC* simulations are, on average,

30% more accurate than persistence over a five-day forecast. In contrast, simulations without

containment show a steep skill decrease on days one and two followed by an increase on later

days, in some cases becoming more skillful than persistence towards the end of the fire. I can

also see that using containment modeling together with fuel moisture maps yields better

results than the containment measures alone, on average 15% more accurate in daily area

burned over a five-day forecast. Including fuel moisture maps, without containment modeling,

did not improve my accuracy overall but *FMC* runs did add to skill when used as a factor in the

ensemble average values. Despite topography being spectrally smoothed to 275m, *smooth-FMC*

configurations do not show a large decrease in skill compared to other non-containment

models in my results.
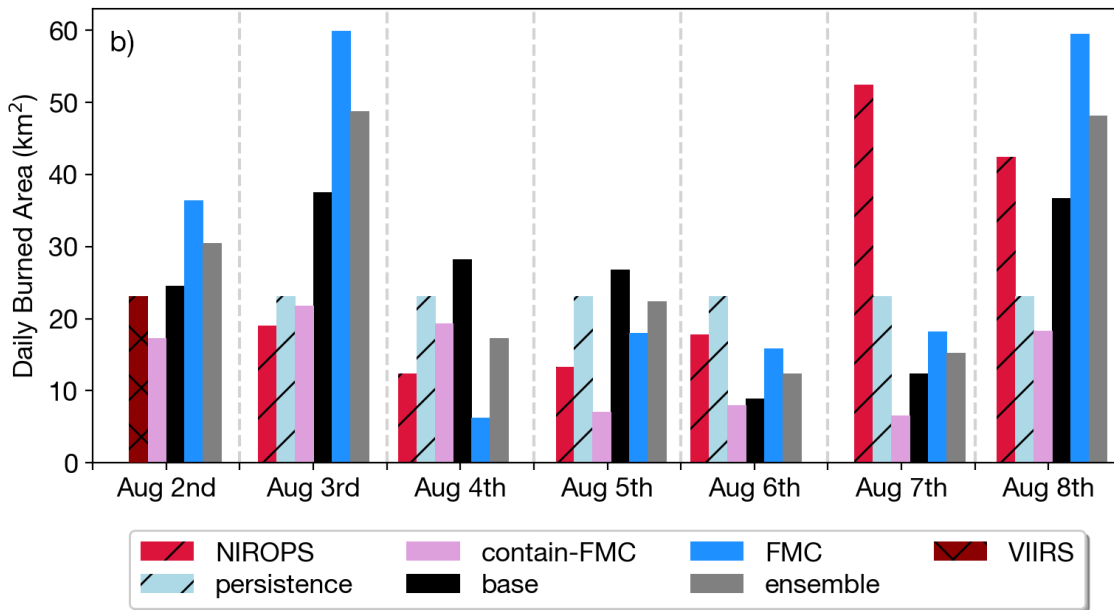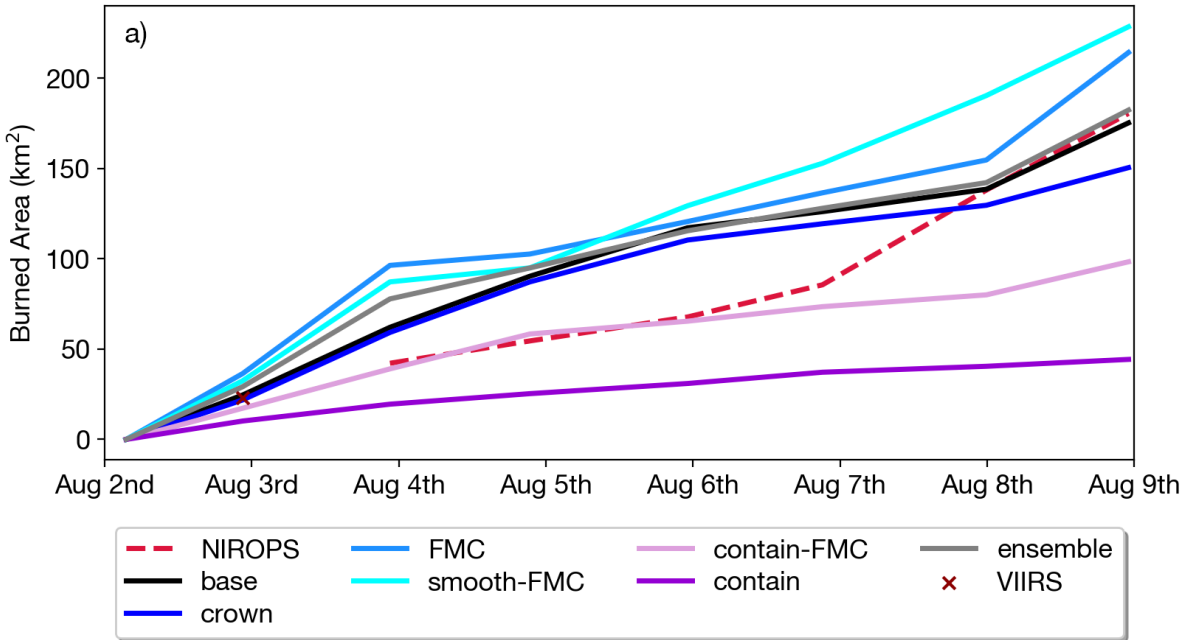
Figure 2.4. a), Time series of total burned area for point ignited simulations. See Section 2.2.4 and/or Table 2.1 for a breakdown of different simulations. b), Daily burned area for the same set of simulations and observations as a). Persistence is forecasted for 6 days and based on the day 1 VIIRS burned area estimate.
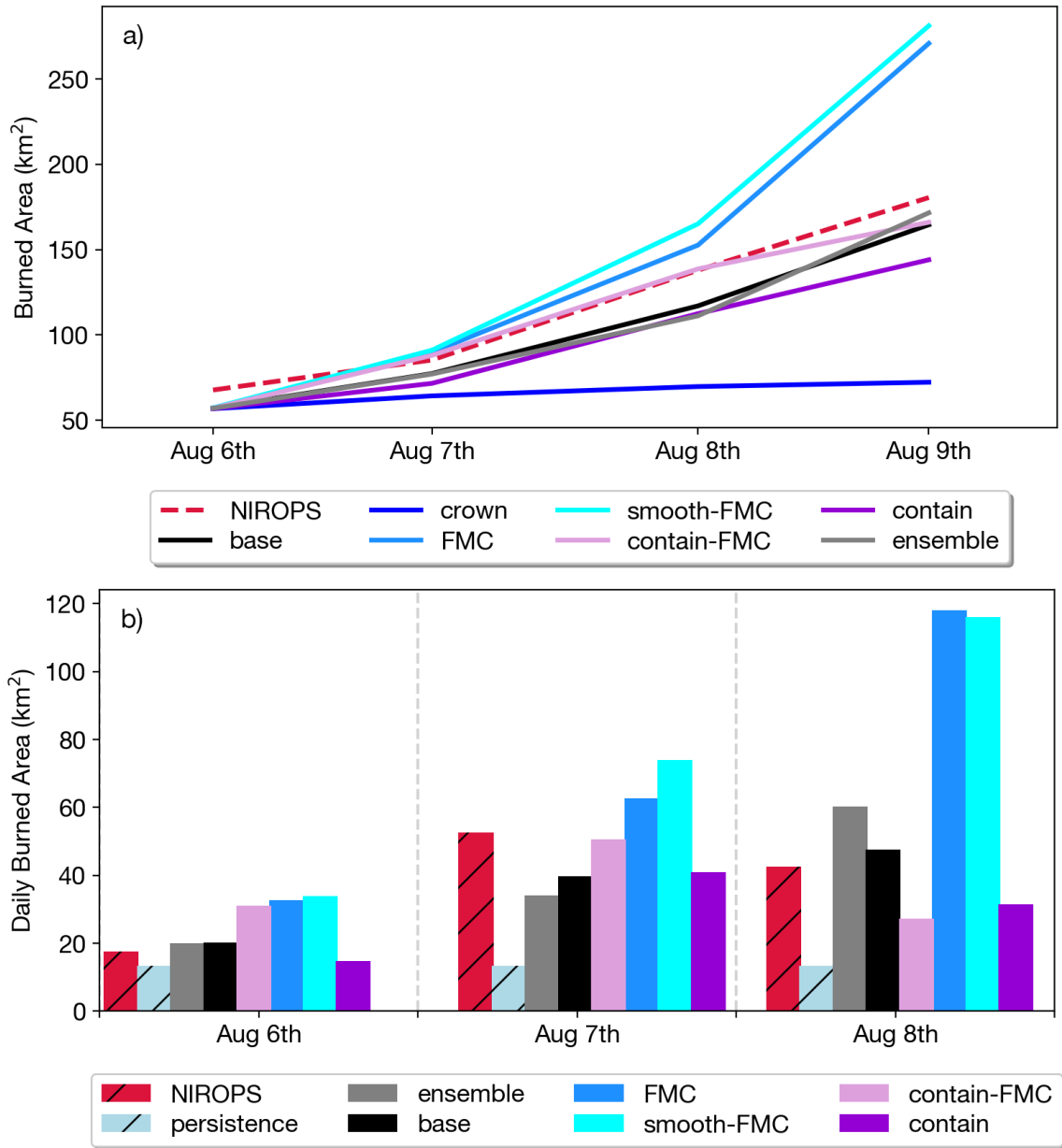
Figure 2.5. a), Burned area time series for real perimeter ignited simulations starting on August 6th, 2019. See Section 2.2.4 and/or Table 2.1 for a breakdown of different simulations. b), Corresponding daily burned area plot.
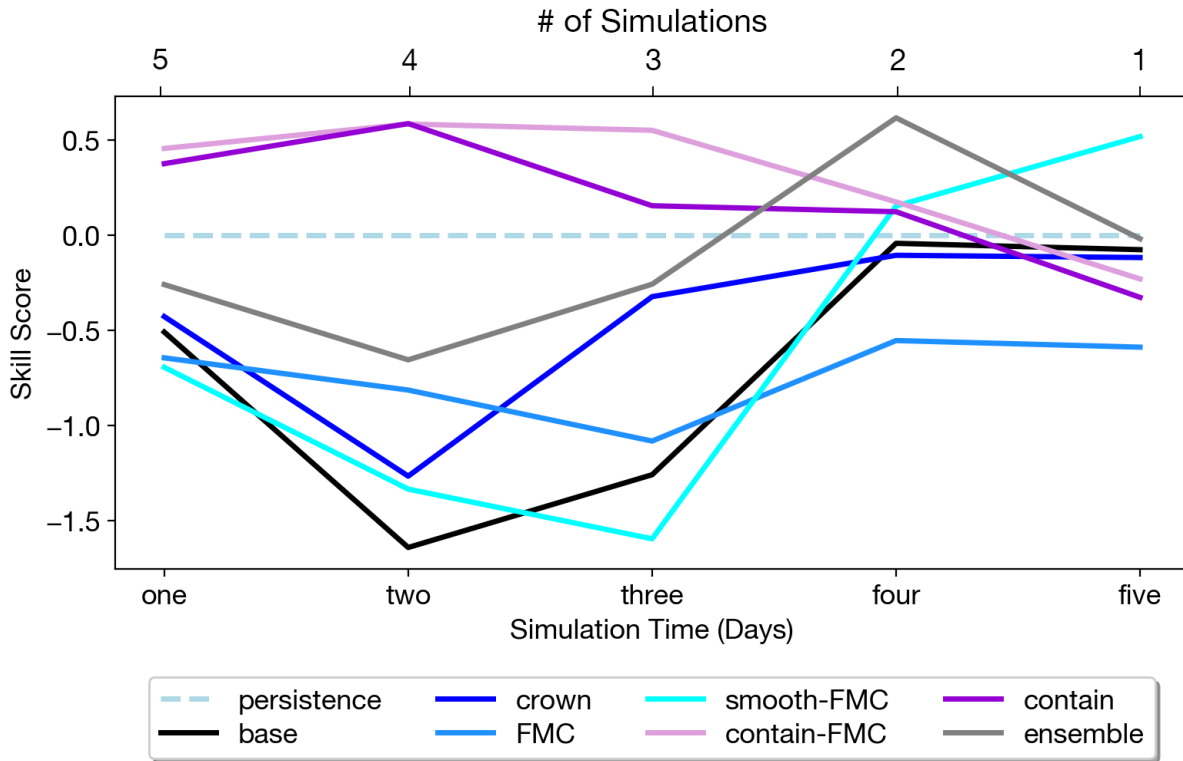
Figure 2.6. Time series of Skill Score (Equation 2.1) between WRF-Fire and NIROPS on daily area burned. Positive values represent fractional improvement over persistence, zero or negative values indicate reduced or no skill increase. Top axis shows the number of simulations per data point. There were 5 one-day forecasts, 4 two-day forecasts, 3 three-day forecasts, 2 four-day forecasts, and 1 five-day forecast. The same breakdown goes for persistence forecasts.

I also plot the absolute error in daily burned area for one, two, and three-day forecasts vs their ignition day (Figure 2.7). In the *ensemble* average and in models without containment, I can see that accuracy improves as perimeters are ignited later in time, at times improving upon persistence for day one forecasts when ignited on later days. This is likely to be a result of the

fire being trapped between the river and its own burnt-out interior on later fire days as

described in Section 2.3.1, although other factors are expanded on in the discussion.
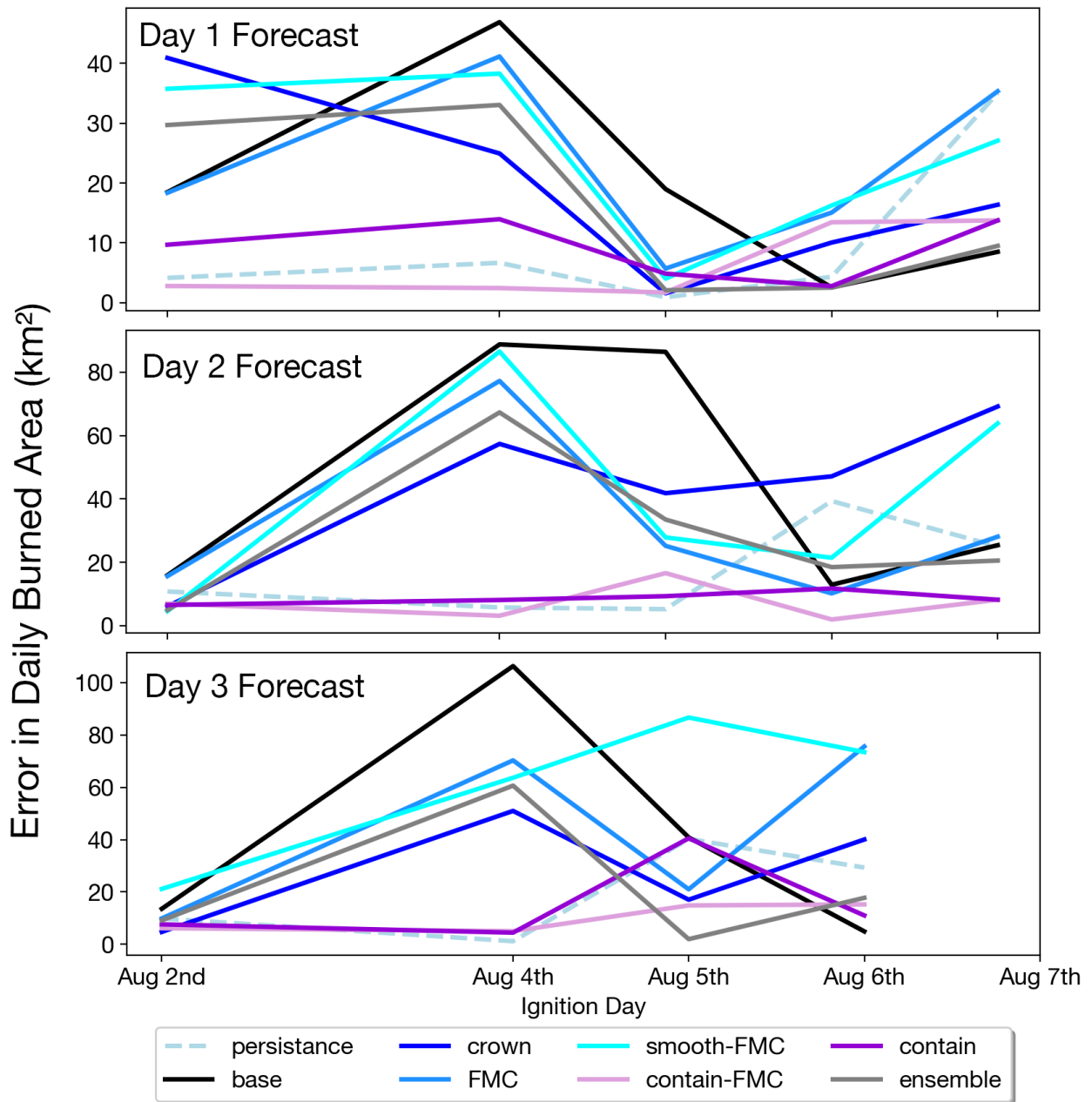
Figure 2.7. Absolute difference between WRF-Fire and NIROPS on daily burned area for different ignition

days and different lengths of time into the simulation. There are no 3-day forecasts for August 7th as the

fire had been mostly contained by August 9th.

2.3.3 Evaluation of Energy Release and Diurnal Cycles

I produce an FRP and fire count product (Section 2.2.5) from WRF-Fire and show one of

my more accurate ignition days simulations (Figure 2.8). Fire count curves have similar

magnitude and shape to GOES-17 products, suggesting that my physical thresholding, radiant

heat fraction, and re-gridding process allows for a reliable comparison framework between

WRF-Fire heat outputs and GOES-17 FRP retrievals.
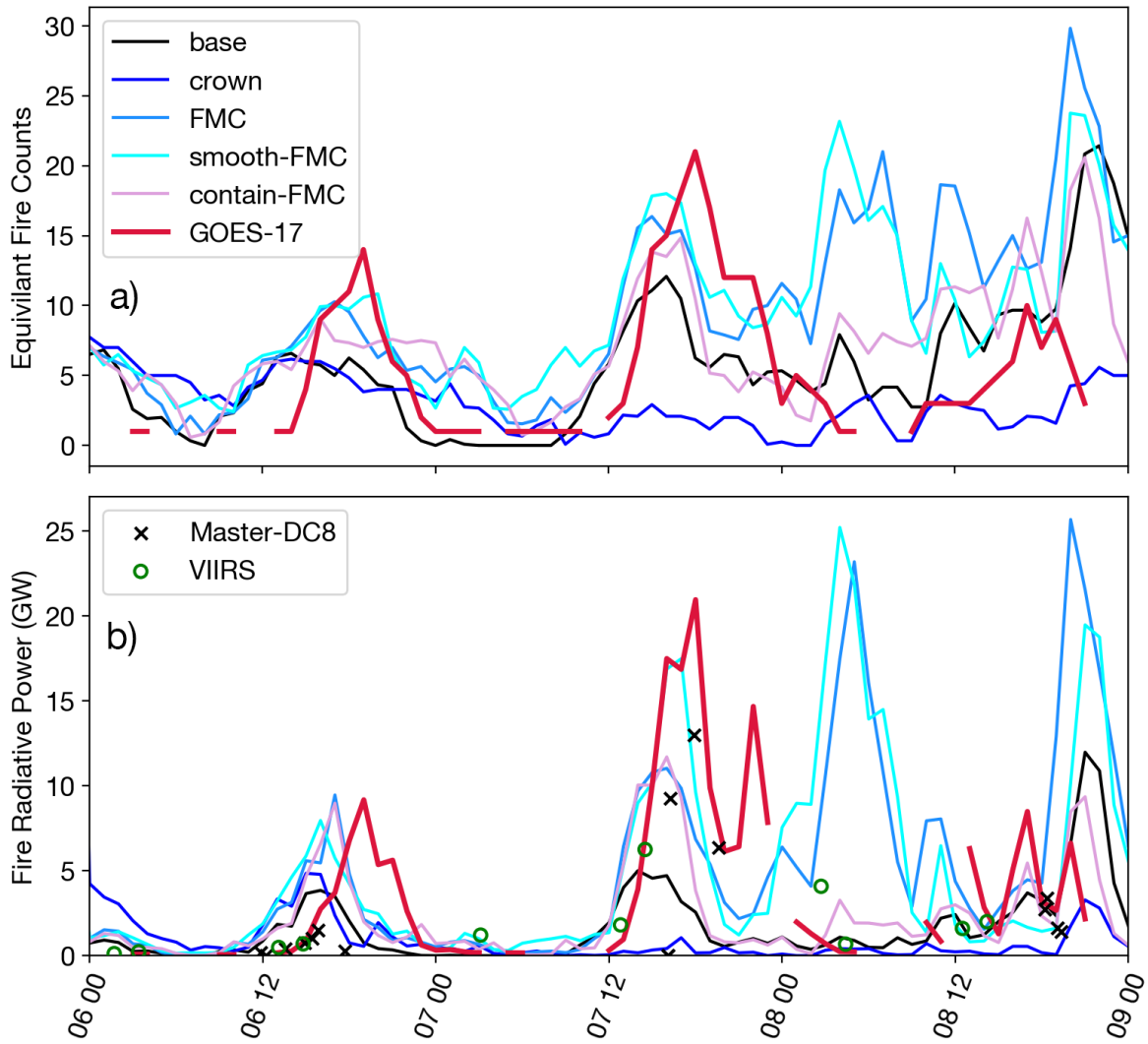
Figure 2.8. Simulations starting from a real perimeter ignition on Aug 6th, 2019. a), Fire counts, either from GOES-17 directly or with WRF-Fire heat data re-gridded and modeled after GOES-17 fire count retrieval (Section 2.2.5). b): Fire Radiative Power (FRP) for all simulations, GOES-17 retrievals, VIIRS retrievals, or the master data from the DC-8 airplane flown in the joint NASA-NOAA 2019 campaign FIREX-AQ.

I find that for configurations that have scaled fuel density, FRP values are always closer to observation on one-day forecasts and usually closer to observation in following days,

alluding to the lack of canopy burning in WRF-Fire *base* configuration (Figure 2.8b). Despite my

fuel density scaling correction and even though fire counts may be high or daily burned area

accurate, the FRP can still be underpredicted. This might be due to uncertainties in fuel type,

fuel density, radiant heat fraction, or some combination of factors.

Another discrepancy I see with FRP comparisons is overprediction of nighttime burning

for some simulations (Figure 2.8b, Supplemental Figure A.15), which may be due in part to the

lack of a dynamic, or time variable, fuel moisture scheme in this study (Hiers et al., 2019;

Moinuddin et al., 2021). Meteorological conditions at Williams Flats over the 7th and 8th

enhanced the nocturnal fire activity (Peterson et al., 2022), which is reflected in the GOES-17

data and partially captured by WRF-Fire simulations (Figure 2.8), albeit overpredicted.

I found it was common in this study for modeled FRP to be out of phase with

observation, usually with fire activity starting and ending too soon. To quantify this lead time, I

looked at cross-correlations between WRF-Fire and GOES-17 FRP curves. To measure just the

correlation in the broad day-night burning signal I removed much of the noise in FRP data. All

simulated FRP curves were smoothed with a 12th degree Savitsky-Golay filter, Min-max

normalized, and had early morning burning from the modeled FRP curves removed due to

unrealistic nighttime burning from the previous day (Figure 2.9). I then estimated the lead time

from modeled to observed FRP curve by selecting the offset time which yielded the maximum

correlation coefficient. Here I found that, on average, all models and prescribed temporal cycles

led FRP retrievals by at least an hour, which increased with forecast day (Figure 2.10). On

average, WRF-Fire's accuracy in temporal cycle is only comparable to the prescribed diurnal

cycle that performed the best (HRRR-Smoke) when containment is applied, fuel moisture maps

are used, and fuel density is scaled up simultaneously (i.e., *contain-fmc* simulation). Although

WRF and nearby RAWS surface wind speeds led, or peaked earlier in the day than, GOES-17 FRP

temporal cycles, surface Air Temperature (T) and Relative Humidity (RH) lagged behind FRP,

peaking or hitting a low later in the day (Supplemental Figures A.8 and A.9).
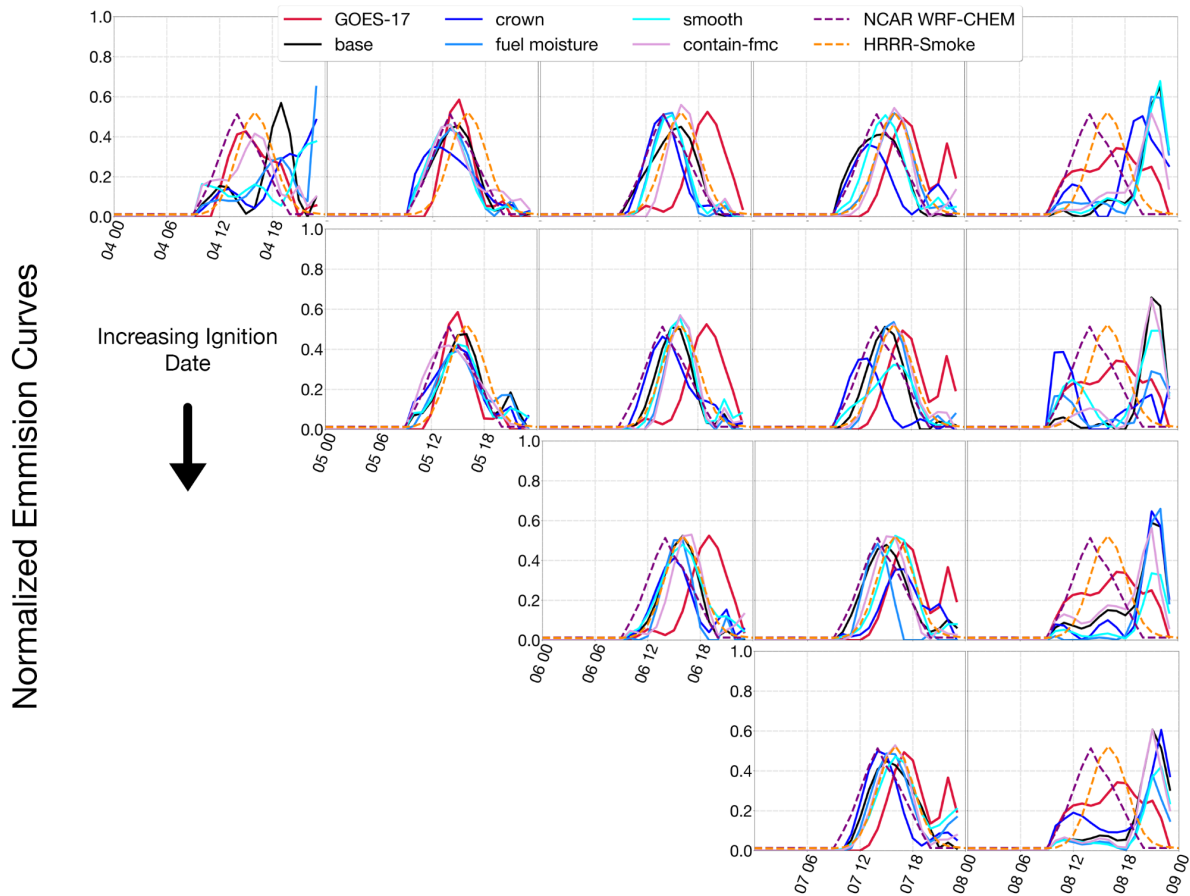
Figure 2.9. Normalized temporal cycles by time into simulation and day ignited. WRF-Fire simulations

and GOES-17 data are interpolated, smoothed, and zeroed out in the early hours of the day to improve

correlation statistics for Figure 2.10. **NCAR WRF-CHEM** and **HRRR-Smoke** are prescribed temporal cycles

for smoke emission modeling, often used in conjunction with persistence forecasting (Section 2.2.5).
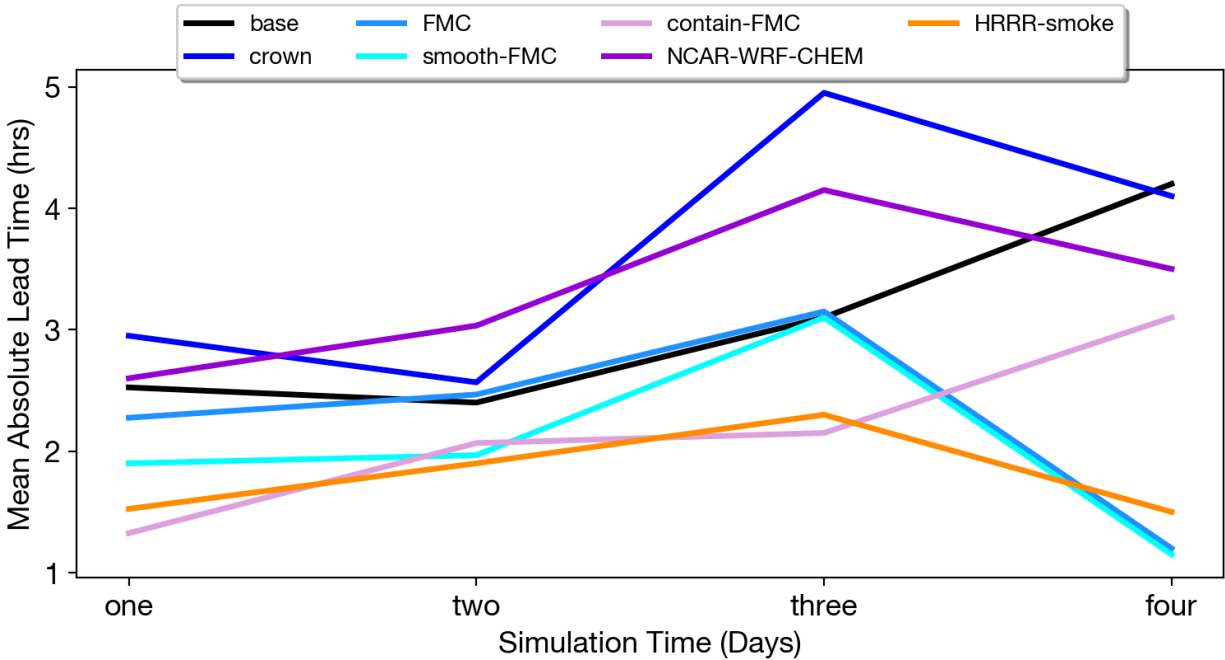
Figure 2.10. Time series of mean absolute lead time between WRF-Fire simulations, smoke emission model prescriptions, and GOES-17 temporal cycles (Figure 2.9). Lead time is the offset of cross correlation that produces the maximum correlation coefficient. Although I show the absolute offset here, it's almost always the case that the model temporal cycles led observations, perhaps in part do my static fuel moisture input (Section 2.4). See Table 2.1 and/or Section 2.2.4 for breakdown of the models.

2.4 Discussion

It is not uncommon for studies to report model biases in overpredicting fire spread and although the mechanisms behind it may be difficult to identify, fuel models are often implicated as the cause (Dahl et al., 2015; Salis et al., 2016). Here I observe a general bias toward overestimation of burned area with some notable exceptions in simulations that were ignited

or burned late into the fire, had increased fuel density, or accounted for containment. The inclusion of FMC maps created larger overpredictions at times as observed conditions were drier than what WRF prescribed by default. This is remedied however when used in conjunction with containment and fuel density scaling which then led to the most accurate results overall. Conversely, when modeling containment and increasing fuel density without fuel moisture maps, I see an underestimation of burned area (*crown* and *contain*, Figures 2.3, 2.5) implying fuel moisture maps generally create more accurate forecasts when containment and fuel density increases are incorporated as well. Thus, my results indicate that increasing realism in all aspects simultaneously (moisture, heat release and containment efforts) is needed to achieve optimal results.

Increasing fuel density to account for crown fires played a role in reducing fire spread where it was part of the configuration. Simulations with increased fuel density but without the fuel moisture maps had significantly less fire spread than the base in the forested regions (Figures 2.2 and 2.3) and at times ended in relative stagnation (Figure 2.3). This is to be expected as higher density fuels spread slower, release more heat and create a stronger convection sink in the center of the plume, potentially inhibiting fire spread (Quaife & Speer, 2021). These results show that WRF-Fire and other coupled models are sensitive to canopy fire modeling and fuel density characteristics. Thus, future work needs to implement canopy burning in a more explicit way (e.g., burning canopy and surface fuels independently) to assess effect into fire spread and heat release. Some of this work is explored in Chapter 3 (Shamsaei et al., 2023).

In this study, modeling containment had the highest impact in reducing burned area

overestimation with the caveat that I have a relatively idealistic way of accounting for containment, where all fire lines are assumed to be completed at the start of the simulation (Section 2.2.3). While this assumption was necessary for my study, future work could include more accurate containment dynamics. Despite this, these results, and the presence of significant containment efforts (Figure 2.1) suggest that for this fire, containment likely played a large role in reducing the spread of the fire, and without modeling containment, overestimation is likely to occur when forecasting burned area. Access to near-real time information on completed and planned fire lines would facilitate the inclusion of this information when these tools are used in forecasting mode.

Without modeled containment, simulations tend to overestimate fire-spread until the later days of the fire where intense burn days occurred. In these final days of the fire, steep topography, lack of roads, a large burnt-out interior, and proximity to the river bend may have made containment difficult or not needed, resulting in few containment lines in the forested mountain ridges (Figure 2.1) and improved accuracy for non-containment simulations (Figures 2.6 and 2.7). Once these factors are in place, I can see that not only are non-containment runs frequently more accurate than persistence, but also the *ensemble* mean can be more accurate than the containment runs (Figure 2.7).

The same configurations that increased accuracy in burned area and FRP (i.e. *contain-fmc*) also increased accuracy in predicting temporal cycles, despite still consistently leading the observations. In general, WRF-Fire and prescribed smoke emission curves both predict the fire as picking up too early in the day and dying off too early at night. Because the modeled temporal curves do not seem to get less out phase with observation as the fire is ignited later

into the fire (Figure 2.9), more accurate meteorology or fire perimeters are perhaps unlikely to be the main driving factor in the lag I observe. One factor influencing this could be the lack of dynamic fuel moisture modeling in this study as fuel may not properly dampen when the temperature drops at night. Indeed, from comparisons between WRF and RAWS data (Supplemental Figures A.8-A.10), it appears that although simulated and observed surface wind speeds lead observed FRP, often picking up in the morning, surface RH and T don't reach their minimum and maximum, respectively, until the afternoon. This supports the idea that the FRP temporal curve is shifted later into the day by the cycle of relative humidity and temperature that modulate fuel moisture content and which is missing in my simulations. New releases of WRF-Fire contain a dynamic fuel moisture model that could be assessed in future work.

A few real-world insights are implied from the difference between WRF-Fire configurations in this study. Based on the impact that containment modeling makes in this study, it's very likely the effort by fire-fighters along the southern and western flanks of the fire, specifically hand lines, dozer lines, and roads as lines, were effective in preventing a much larger wildfire. In this fire, containment lines in flat grasslands may have been easier for fire crews to implement compared to steep forests but the results here indicate that such efforts likely make a large difference in containing the overall fire spread anyway. I believe that the development of a near-real-time public data repository for current and planned containment lines and/or the addition of more accurate timestamps in the historical archives have the potential to greatly improve smoke and wildfire modeling efforts.

2.5 Conclusions

Wildfire forecasting remains a challenging task in both operational and research settings. Here we've partially alleviated this by assessing WRF-Fire's sensitivity to different model configurations. Inputs such as FMC, scaled fuel densities, and containment lines were incorporated into the model in different configurations and the results were compared against common forecasting metrics. Daily burned area and FRP were calculated and compared to standard methods of forecasting such as persistence and assumed temporal cycles. Results suggest that certain configuration options can be the difference between outperforming standard forecasting methods or incurring significant error, with containment modeling being the most important for this fire.

I found that WRF-Fire can be more accurate than persistence in burned area, and thus improve smoke forecasting skill, when used with sufficiently realistic input conditions. The combination of incorporating novel inputs in containment, fuel moisture, and fuel density in one configuration yielded the best results, with 30% less error than persistence on daily burned area over a five-day forecast. To a lesser degree, using an ensemble forecast, igniting later into the fire, or forecasting for big fire growth days also helped in improving upon persistence. When used as inputs, satellite derived fuel moisture maps improve accuracy in daily burned area occasionally, but only when combined with containment and fuel density increases do they provide a consistent boost in accuracy.

This trend continued into my analysis of diurnal cycles, where accounting for containment, fuel moisture, and fuel density increases showed the most skill in capturing

temporal cycles and heat output. Under these best-case configurations, WRF-Fire matches the accuracy of prescribed diurnal cycles used in air quality models. I found that increasing the fuel density, especially when FMC balanced out the reduced fire spread, improved WRF-Fire's FRP outputs significantly.

On average, all WRF-Fire temporal cycles and smoke emission model cycles commence too early in the day by at least an hour, and although the cause is not completely clear, a further investigation into dynamic fuel moisture schemes could help to illuminate this. In addition, I found simulations that accounted for FMC could produce nighttime burning similar to GOES-17 observations but often overestimated. With the increase of nocturnal burning under climate change (Balch et al., 2022) dynamic fuel moisture and nighttime burning could be important for future studies.

From a methodological standpoint, this study has established several important comparisons between simulation and observation. I have shown that WRF-Fire can be compared against GOES-17 fire count and FRP after re-gridding to the GOES-17 grid and accounting for the radiant heat fraction. Several insights have been drawn from this comparison including that the WRF-Fire default configuration does not release enough heat compared to satellite observation. In addition, my sensitivity study on WRF-Fire's second domain time step, or by proxy, the number of re-initializations per second of the level set function, was a previously unexplored topic in real fire simulation studies and shows the need for future studies to carefully consider time step choice on a case-by-case basis.

Chapter 3

Sensitivity of Smoke Injection Heights and Pyrocumulonimbus Clouds to Canopy Burning and Increased Fuel Depth

3.1 Introduction

The effect of wildfire smoke on regional and local air quality can be hazardous and unexpected (Black et al., 2017) and with large wildfires becoming increasingly common in recent years (Abatzoglou & Williams, 2016), the need for better forecasting has risen as well. Wildfires are notoriously hard to forecast in simulation, needing careful consideration to outperform simple "persistence" models (Chapter 2). While I showed that WRF-Fire could predict daily burned are better than persistence when accounting for containment and fuel moisture heterogeneity, fire radiative power (FRP) was still underpredicted and is a key variable correlated with smoke emission (Sofiev et al., 2011) and smoke injection height (the maximum height smoke is lofted to over the fire). Forecasting smoke injection height for a fire, and the vertical partitioning of smoke mass throughout the atmosphere is critical to forecasting downwind air quality during wildfire events (Ye et al., 2021).

Smoke injection heights and vertical smoke distribution are also difficult to predict and often times parameterized plume rise models are used along with planetary boundary layer schemes (PBL) to achieve realistic results (Thapa et al., 2022; Ye et al., 2021). Other studies have used coupled-fire weather models such as WRF-Fire but used observations of high temporal resolution fire-spread to drive the fire spread exactly along the path of the real fire, isolating the effect of fuel properties and heat output on smoke injection (Lee et al., 2023; Roberts et al., 2023). Smoke injection height can still be underpredicted in these models and uncertainty in fuel properties is suggested as driving much of the error.

Here I add a recently developed canopy model (Shamsaei et al., 2023) to our WRF-Fire simulations from Chapter 2, along with fuel depth increases to account for fire suppressed regions to determine what fuel properties are needed to forecast realistic smoke injection heights and vertical smoke distributions. The focus remains on the 2019 Williams Flats Fire and the wealth of observations taken during the 2019 FIREX-AQ field campaign.

3.2 Methods

This Chapter will continue the analysis of Chapter 2 on the 2019 Williams Flats Fire but focus on the vertical dimension therefore much of the methods from Chapter 2 apply here as well. I continue to use HRRR re-analysis data as meteorological forcing for most simulations, horizontal resolution is set to 200 m and 50 x 50 km on the inner domain while the outer domain has a resolution of 1 km. NIROPS and VIIRS analysis is the same from Chapter 2 and GOES-17 FRP is compared to simulation using the same framework. The WRF and WRF-Fire model are described in the methods section of Chapter 2 as well as the sources for input data

for WRF-Fire and the background for the Williams Flats Fire. The most notable differences between methods sections include the use of a canopy model and the increase of fuels depths.

The canopy model used in this study was developed by Kasra Shamsaei out of the University of Nevada, Reno and this is one of the first implementations of the code in the literature (Shamsaei et al., 2023). The code will take canopy bulk density and canopy cover data from the LANDFIRE repository described in the Chapter 2 (see Methods 2.2.2) and use that to produce additional heat flux when the fire is burning in the surface grid. These canopy fuels are considered thermally thin, in that the density only describes the fuel that are easily burnt, similar to the surface fuel loading. In addition, they burn at the same rate as the surface fuels, with the time to reach 30% fuel mass remaining set by the weighting parameter *w* in the "namelist.fire" which is an effective proxy of resistance time for a burning fuel cell. A limitation of this code is that there is no threshold for burning of canopy fuels, they are always on fire if the surface fuel is on fire. Although this likely leads to unrealistically high heat release to some degree, the implementation for such a threshold is not straightforward and could depend on fuel type, canopy base, wind speed, and fire-spread. In addition, because this fire generated a pyroCb and was medium-large in overall size (~44 km^2), and because I underpredicted FRP in Chapter 2, such a threshold may not be a big factor for this study. I also note that the canopy code is separate from the fuel moisture map code out of NCAR (CO-FPS) and both configurations can't be combined currently, although when running the canopy model, the homogeneous fuel moisture content is taken as the average value of the corresponding day's fuel map.

Modifying fuel loading and fuel moisture had important and sometimes competing

effects on the simulation output in Chapter 2, and here I include fuel depth in that analysis. In

Chapter 2 I showed that increasing fuel loading slowed fire-spread but that was counteracted

by using fuel moisture maps as input. Here I investigate a new property, fuel depth, which can

increase the rate of fire-spread and heat output of the fire and counteract the effect of

increased fuel loads more causally. Observation and analysis has shown that fuel loads [kg/m]

increase under fire suppression in Temperate and Boreal Forests including the Western United

States (Johnson et al., 2001; Roos et al., 2020). This makes fuel depth and fuel loading logical to

increase with each other but the exact magnitude of which is somewhat uncertain. Some

studies suggest an equilibrium surface fuel depth is achieved over time (Keifer et al., 2006) with

the caveat of limited data. Other data suggest surface fuel depth could nearly double 5 years

post bark beetle mortality (Hoffman et al., 2011), a sign of significant variability in fuel depth in

response to environmental conditions. WRF-Fire, by default prescribes average fuel depths for

forested categories of 23.1 cm, which is roughly in line with field measurements of similar

forested stands to the Williams Flats Fire (Donato et al., 2013). Here I increase fuel depths in

simulations with *fuels+* designations so that the negative effect of increasing fuel loads is

counteracted by the increase in fuel depth and while producing realistic smoke injection

heights. I find that increasing the average fuel depth of forested region to 50 cm best fits this

aim (Table 3.1). This fuel depth is well above literature cited values but was necessary to

achieve realistic fire spread and smoke injection heights with increased fuel loadings from FINN

(Chapter 2, *crown*) and without the fuel moisture code CO-FPS (Chapter 2, *FMC*). One possible

explanation for the needed increase in fuel depth is that WRF-Fire was not developed with

intense pyro-convection (vertical winds > 10 m/s) in mind and disturbance of the fuel structure mid-fire could play a role, despite a lack of investigation in the literature. Another is the possibility of compensating for the lack of conversion from live fuel to dead fuel, something that was only possible with the CO-FPS model that the fuel moisture maps are part of. The combination of these factors or other undiscussed ideas should be considered as well. As an update from Chapter 2, the average fuel loading in conifer forest categories was increased to 19.3 kg/m^2, to better match observations of such fuels under historical fire suppression (Keifer et al., 2006). All other fuel categories fuel loadings followed increases related to FINN values (Wiedinmyer et al., 2011) from Chapter 2, and fell within the range of values reported as possible under long term fire suppression (Keifer et al., 2006).

	Scott-Burgan	Scott-Burgan FINN	Fuel Depth
15: Short, Sparse Dry Climate Grass (Dynamic) [GR1 (101)]	0.02	0.25	0.12
16: Low Load, Dry Climate Grass (Dynamic) GR2 (102)	0.02	0.25	0.30
17: Low Load, Very Coarse, Humid Climate Grass (Dynamic) [GR3 (103)]	0.02	0.25	0.61
18: Moderate Load, Dry Climate Grass (Dynamic) [GR4 (104)]	0.06	0.62	0.61
19: Low Load, Humid Climate Grass (Dynamic) [GR5 (105)]	0.09	0.99	0.46
20: Moderate Load, Humid Climate Grass (Dynamic) [GR6 (106)]	0.02	0.25	0.46
21: High Load, Dry Climate Grass (Dynamic) [GR7 (107)]	0.22	2.47	0.91
22: High Load, Very Coarse, Humid Climate Grass (Dynamic) [GR8 (108)]	0.11	1.24	1.22
23: Very High Load, Humid Climate Grass (Dynamic) [GR9 (109)]	0.22	2.47	1.52
24: Low Load, Dry Climate Grass-Shrub (Dynamic) [GS1 (121)]	0.04	0.66	0.27
25: Moderate Load, Dry Climate Grass-Shrub (Dynamic) [GS2 (122)]	0.11	1.66	0.46
26: Moderate Load, Humid Climate Grass-Shrub (Dynamic) [GS3 (123)]	0.07	1.00	0.55
27: High Load, Humid Climate Grass-Shrub (Dynamic) [GS4 (124)]	0.43	6.30	0.64
28: Low Load Dry Climate Shrub (Dynamic) [SH1 (141)]	0.06	0.83	0.30
29: Moderate Load Dry Climate Shrub [SH2 (142)]	0.30	4.48	0.30
30: Moderate Load, Humid Climate Shrub [SH3 (143)]	0.10	1.49	0.73
31: Low Load, Humid Climate Timber-Shrub [SH4 (144)]	0.19	2.82	0.91
32: High Load, Dry Climate Shrub [SH5 (145)]	0.81	11.95	1.83
33: Low Load, Humid Climate Shrub [SH6 (146)]	0.65	9.62	0.61
34: Very High Load, Dry Climate Shrub [SH7 (147)]	0.78	11.61	1.83
35: High Load, Humid Climate Shrub [SH8 (148)]	0.46	6.80	0.91
36: Very High Load, Humid Climate Shrub (Dynamic) [SH9 (149)]	1.01	14.93	1.34
37: Low Load Dry Climate Timber-Grass-Shrub (Dynamic) [TU1 (161)]	0.04	0.86	0.47
38: Moderate Load, Humid Climate Timber-Shrub [TU2 (162)]	0.21	4.08	0.79
39: Moderate Load, Humid Climate Timber-Grass-Shrub (Dynamic) [TU3 (163)]	0.25	4.73	1.03
40: Dwarf Conifer With Understory [TU4 (164)]	1.01	19.34	0.39
41: Very High Load, Dry Climate Timber-Shrub [TU5 (165)]	0.90	17.19	0.79
42: Low Load Compact Conifer Litter [TL1 (181)]	0.22	10.81	0.16
43: Low Load Broadleaf Litter [TL2 (182)]	0.31	6.02	0.16
44: Moderate Load Conifer Litter [TL3 (183)]	0.11	21.62	0.24
45: Small downed logs [TL4 (184)]	0.11	2.15	0.32
46: High Load Conifer Litter [TL5 (185)]	0.26	24.86	0.47
47: Moderate Load Broadleaf Litter [TL6 (186)]	0.54	10.31	0.24
48: Large Downed Logs [TL7 (187)]	0.07	1.29	0.32
49: Long-Needle Litter [TL8 (188)]	1.30	24.92	0.24
50: Very High Load Broadleaf Litter [TL9 (189)]	1.49	28.57	0.47
51: Low Load Activity Fuel [SB1 (201)]	0.34	6.45	0.79
52: Moderate Load Activity Fuel or Low Load Blowdown [SB2 (202)]	1.01	1.01	0.30
53: High Load Activity Fuel or Moderate Load Blowdown [SB3 (203)]	1.23	1.23	0.37
54: High Load Blowdown [SB4 (204)]	1.18	1.18	0.82

Table 3.1: Fuel loadings in kg/m^2 for "Scott-Burgan" and "Scott-Burgan FINN" vs fuel category description and number. "Fuel Depths" in meters for with adjusted average fuel depth of 50 cm in forested regions. The first 14 fuel categories are not used by the Scott-Burgan 40 fuel category model in WRF-Fire, see Chapter 1, Supplemental Table 1. The values in parenthesis at the end of the fuel category name represent the values in the actual input data.

The simulations chosen for this chapter are described in Table 3.2 and are partially taken from Chapter 2, with several important exceptions. The *contain_canopy_fuels+* simulations use the final containment lines, the new canopy code, the fuel loading increases from FINN (Chapter 2), fuel depth increases to 50 cm in forested categories (Table 3.1). The *contain_fuels+* uses the same configuration but omits the canopy code. The *contain_canopy_fuels+NAM* follows the same pattern but uses the 12 km North American Mesoscale Model (NAM) as meteorological forcing (Rogers et al., 2009) instead of the HRRR. The *contain_fmc_vert_hrs* simulation is the same as the *contain_fmc* simulation except it uses a refined vertical resolution, maintaining roughly 200 m vertical grid spacing from above the surface layers (layers with less than 200 m spacing) until the top of the domain. This enhanced vertical resolution more than doubles the number of vertical levels from 44 to 106. The *contain_fmc_111m* simulation is the same as the *contain_fmc* simulation except it uses a refined horizontal resolution of 111 m on the LES domain (while smoothing terrain to maintain time step; see Chapter 2, Supplemental Section A.2). The Simulations ending in *06* are ignited on August 23:10 PDT August 5th, 2019, from a NIROPS perimeter as described in Chapter 2 and shown in Figure 2.2a. Simulations which end in *07* are ignited on 21:10 PDT August 6th from NIROPS perimeters shown in Figure 2.2b. Simulations which end in *02* are ignited on August 2nd from a point ignition as described in Chapter 2. The naming trend is such that the number at the end represents the first simulation day for that configuration.

	200m LES	200m Vert	Fuel Moisture	FINN Fuel Loading	50cm Fuel Depths	Canopy Model	Containment	NAM Forcing
base	✓							
crown	✓			✓				
contain_FMC	✓		✓	✓			✓	
contain_FMC_111m			✓	✓			✓	
contain_FMC_vert_hres	✓	✓	✓	✓			✓	
contain_canopy_fuels+	✓			✓	✓	✓	✓	
contain_fuels+	✓			✓	✓		✓	
contain_canopy_fuels+NAM	✓			✓	✓	✓	✓	✓

Table 3.2. Simulation names and the different configuration options they represent. "200m LES" represents 200 m horizontal resolution on the inner LES domain, where not indicated the resolution was 111 m. "200m Vert" represents a vertical resolution of about 200 m above the surface layers (< 200m spacing). "Fuel Moisture" represents fuel moisture maps used in Chapter 2. "FINN Fuel Loading" represents scaling of fuel loading from Chapter 2. "50cm Fuel Depths" indicates fuel depths were scaled up to a 50 cm average in forested regions. "Canopy Model" represents use of new canopy burning model (Shamsaei et al., 2023), "Containment" represents final containment lines from Chapter 2. "NAM Forcing" represents North American Mesoscale Model as meteorological forcing, with HRRR used when not indicated.

3.3 Results

In Figure 3.1, I show the fire perimeters from Chapter 2 simulations (*crown, contain_FMC)* against new configurations with the canopy burning code included and fuel depth increases (*canopy_fuels+)*. The new canopy code simulation perimeters and burned areas compare well to the NIROPS perimeters as well as simulations from Chapter 2. Note that the *crown* simulation from Figure 3.1 has the same fuel loadings as the *contain_fuels+* simulations, but without fuel depth increases, fuel moisture maps, or a canopy model (*fuels+, FMC, canopy),*

leading to virtual stagnation of the fire-spread from the high fuel loadings. Despite the

reasonable accuracy, *fuels+* simulation seems to display many spotty areas of unburnt fuel

within the final fire perimeter (Figure 3.1d) which could have been a detriment to establishing

long or deep fire fronts.
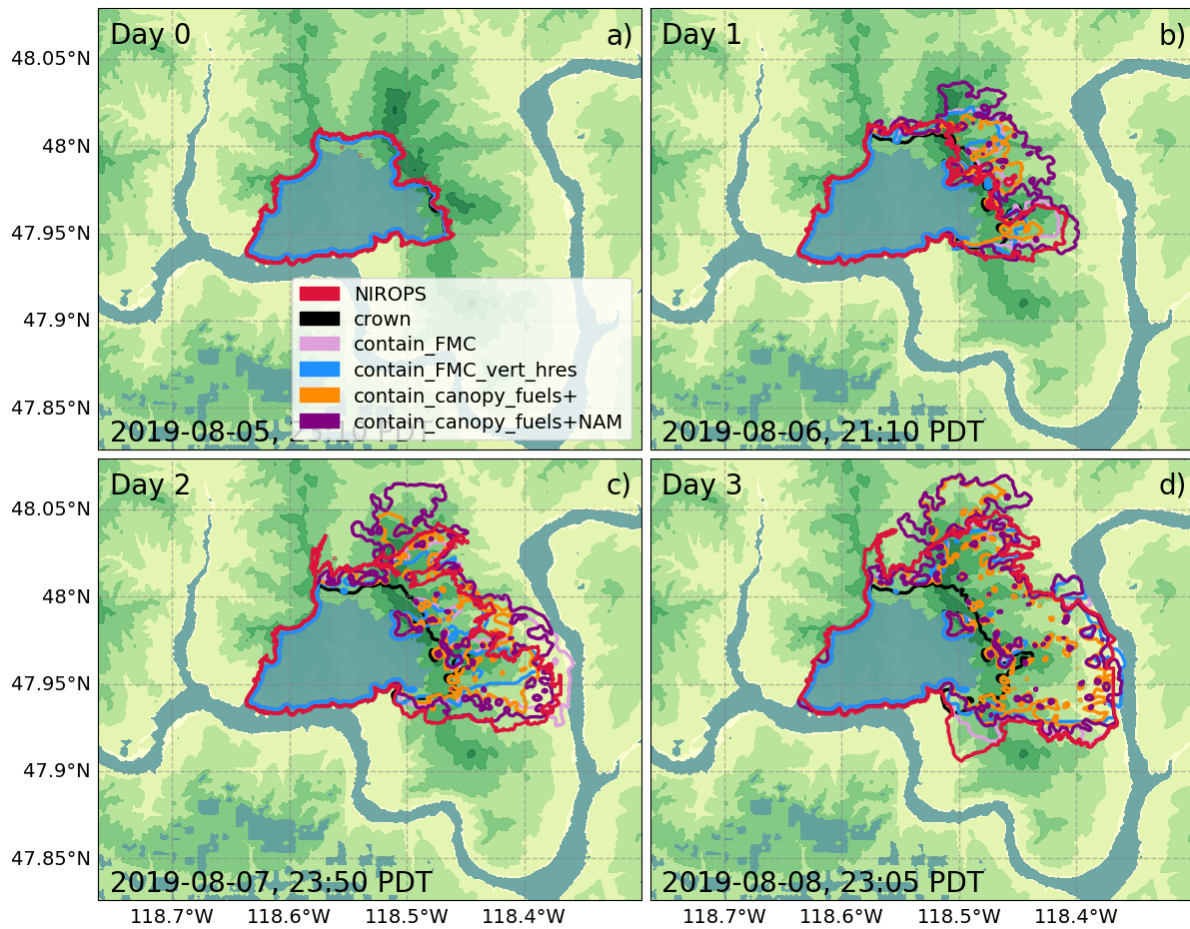
Figure 3.1. Fire perimeters for simulations ignited on August 5th, 23:10 PDT for the first three days of

Williams Flats Fire simulations. Configurations from Chapter 2 are plotted against a newly developed

canopy burning code in simulation with orange and purple. All simulations shown here are ignited from

the NIROPS perimeter in a) as described in Chapter 2 Methods.

In Figure 3.2, I show a vertical snapshot of smoke and cloud contours at peak smoke height injection time. This figure illustrates the process of deep convection that occurs in our simulations of the pyroCb event that took place on August 8th, 2019, at the Williams Flats Fire. Contours of water and ice cloud are shown, but rain, snow, and graupel were all present in significant amounts throughout the cross-section, perhaps implying significant downdrafts in the wake that bring smoke back down to lower altitudes. Note the significant amount of smoke below the boundary layer, as well as what looks like a separated plume above that from deeper injection.
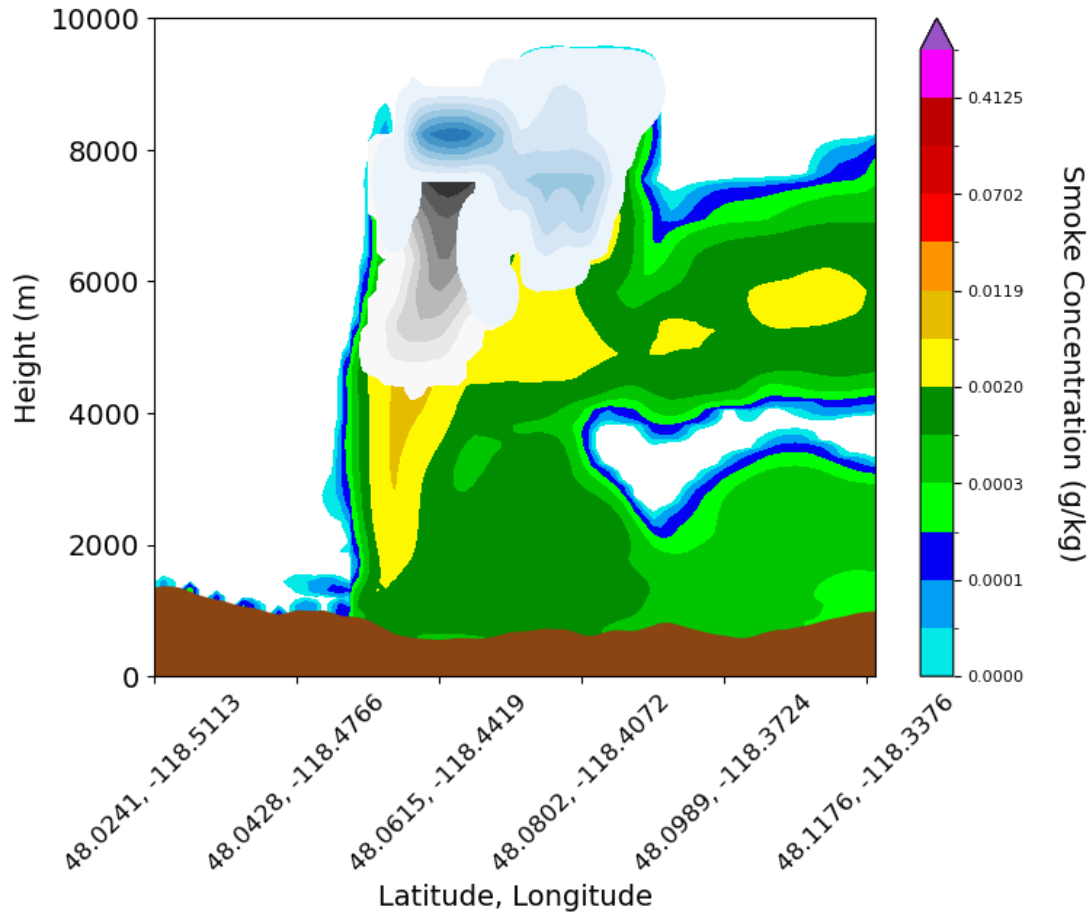
Figure 3.2. Vertical cross-section at peak injection time (21:00 PST August 8th, 2019) of smoke (multicolored), cloud (greys), and ice (blues) concentration contours for the *contain_canopy_fuels+_06* simulation. Rain, snow, and graupel (not shown for clarity) were present in significant amounts in the cross-section, but at lower heights than the ice clouds.

Continuing vertical analysis of the fire in Figure 3.3, I show smoke injection heights for simulations over the period in which pyroCbs formed for the Williams Flats Fire (Aug 6th-9th). Many deep ice clouds were formed in simulation, both near the PyroCb times (Late Aug 8th), and earlier. I compare simulation output against radar estimates of smoke injection heights

(Krishna et al., 2023) and lidar products from the DC-8 aircrafts (Ye et al., 2021). Radar

estimates of smoke injection heights are the 90th percentile of the distribution of retrieved

smoke tops, as those values tend to agree better with other observations and perhaps help

account for error in resolution at the top angles of the radar. Configurations with *fuels+*

designations performed well against observations reaching ~9 km on the 8th, compared to ~10

km in observations (Figure 3.3) although smoke injection heights were still underpredicted on

the night of the 7th and during the afternoon of the 8th. I note some overestimation of heights

on *fuels+* simulations on the 6th, the lowest fire activity day shown in figure 3.3, but not by large

amounts. Configurations without the *fuels+* changes underpredicted for much of the period,

but the *contain-FMC-hrs-vert* and the *contain-FMC-111m* simulation managed to reach ~8 km

on the evening of the 8th, with the *contain-FMC-111m* configuration outperforming other non-

fuels+ simulations on the 7th. No simulations accurately capture the pyroCb generated on the

night of the 7th, shown in the radar data. The simulation starting on the evening of the 6th

(*contain_canopy_fuels+07)* performs slightly better on smoke injection heights and timing on

the 7th and 8th, but not by wide margins. Changing the forcing meteorology from HRRR to NAM

seems not to have made a significant difference in smoke injection height.
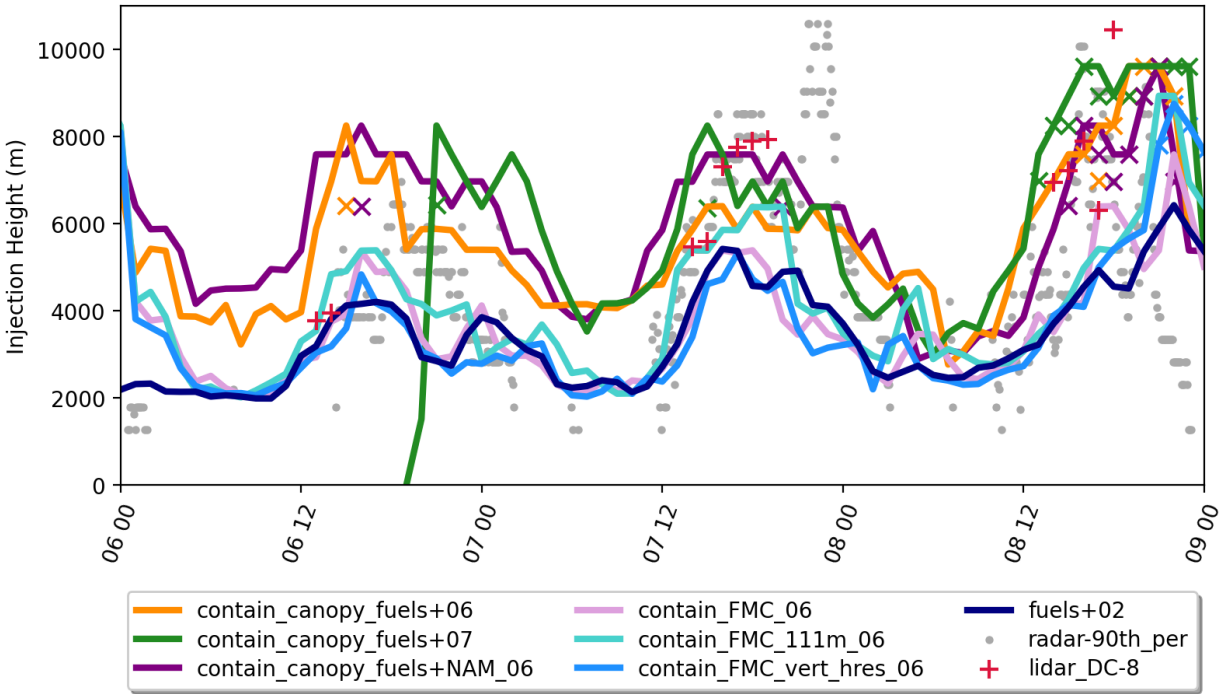
Figure 3.3 Smoke injection (-) and ice cloud top (X) heights across the period of maximum fire activity

from the 2019 William Flats Fire (Aug 6th-9th). Gray circles are radar inferred smoke top heights (Krishna

et al., 2023). Red plus symbols are LIDAR measurements from the DC-8 aircraft which flew over the

Williams Flats Fire during the 2019 FIREX-AQ field campaign (Ye et al., 2021).

In Figure 3.4, I show FRP times series from various simulations compared to satellite and

aircraft observations (VIIRS and DC-8 respectively) using the same methodology used to

construct Figure 2.8 (see Methods 2.2.5). I note a large overestimation in FRP for the

canopy_fuels+ simulations last the length of the fire. This is likely due to my increase of fuel

depth in my simulation above what is noted in the literature, or a lack of canopy burning

threshold (see Methods 3.2) but note that although I used 50 cm as an average fuel depth in

forested regions, I still underestimate smoke injection heights on many days (Figure 3.3) and

adjusting to 40 cm average fuel depth (not shown here) produced significantly lower smoke

injection heights. This perhaps implies that the increased fuel depth and loading leads to heat

excessive heat release that is overcompensating for some aspect of deep convection not

accounted for in the model. Potential missing factors for deep convection are speculated on the

Discussion and Conclusion 3.4.
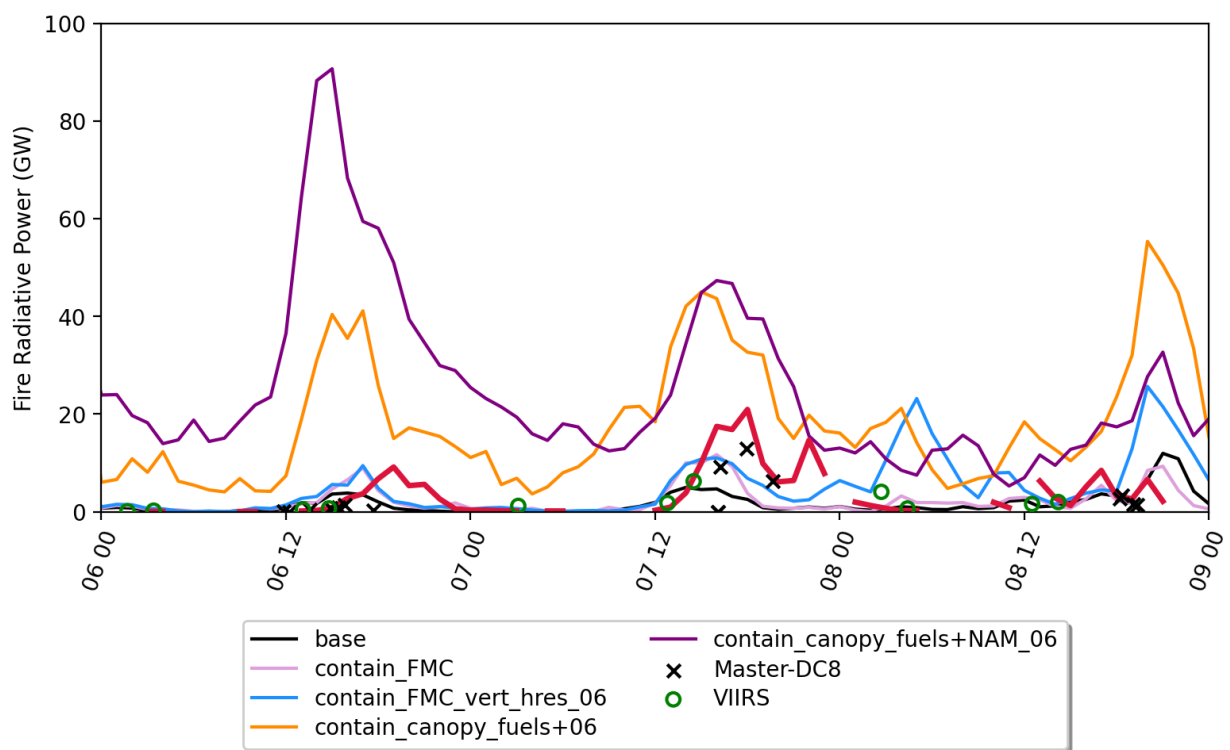
Figure 3.4. FRP across the most intense period of fire activity for the 2019 Williams Flats Fire.

Green circles are FRP products from VIIRS and black crosses are FRP retrievals from the DC-8

aircraft collecting data during the FIREX-AQ field campaign.

In Figure 3.5 I show iso-contours of heat flux at 1000 W/m^2 during a pyroCb event to

illustrate the geometry of the fire front. In all simulations, there seems to be a tendency to

56

create many small pockets of high heat rather than the more connected and typical fire front

shape I see from aircraft observations over the fire (Peterson et al., 2022). This was true of

other iso-contour values, but 1000 W/m^2 was chosen as best representative of that feature.

There is a potential for this to result in shallower fire fronts than what occurred in reality,

leading to smaller plume diameters and shallower plume heights for a given FRP (Badlan et al.,

2021b). This is one factor that might have driven the need for high fuel loads and subsequently

high FRP to reach realistic smoke injection heights.
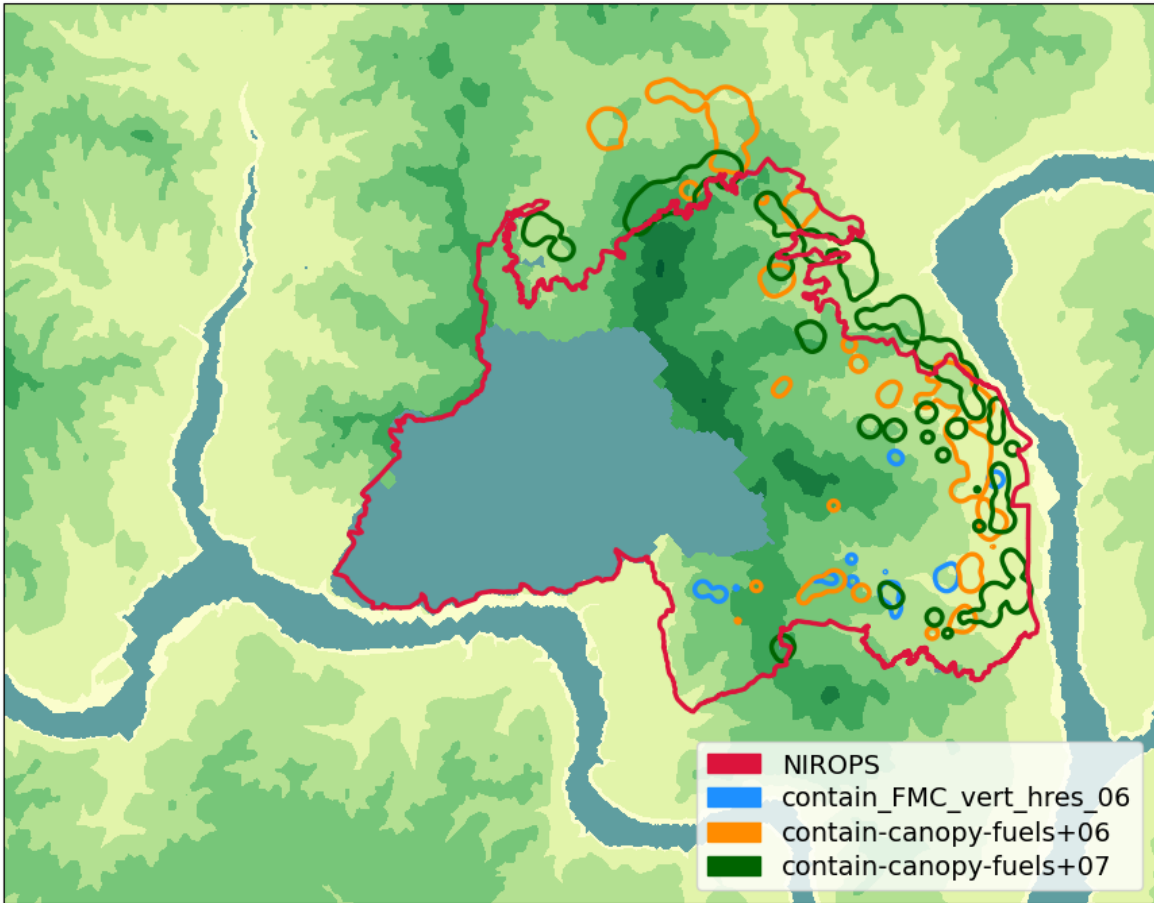
Figure 3.5. Iso-contours of heat flux at 1000 W/m^2 for three simulations discussed earlier at 20:00 PDT Aug 8th, compared to the final NIROPS perimeter. This roughly corresponds to a local maximum in FRP from Figure 3.4 and contributes to the pyroCb shown in Figures 3.2 and 3.4.

In Figure 3.6, I show smoke injection heights across the period of main fire activity for the Williams Flats Fire. 7-day forecasts starting on August 2nd from point ignition and 3-Day forecasts starting on August 5th from NIROPS retrievals are shown. My *contain_canopy_fuels+_02* simulations display surprising amount forecast skill on a 7-day forecast of smoke injection height, with heights increasing over time in agreement with

observations. Interestingly, simulations ignited from NIROPS on the 5th do not display

significantly different accuracy in smoke injection heights compared with point ignited

simulations. I also note that the *fuels+* simulation, without the *canopy* model, significantly

underpredicts smoke injection heights, highlight the need for the explicit canopy burning

formulation.
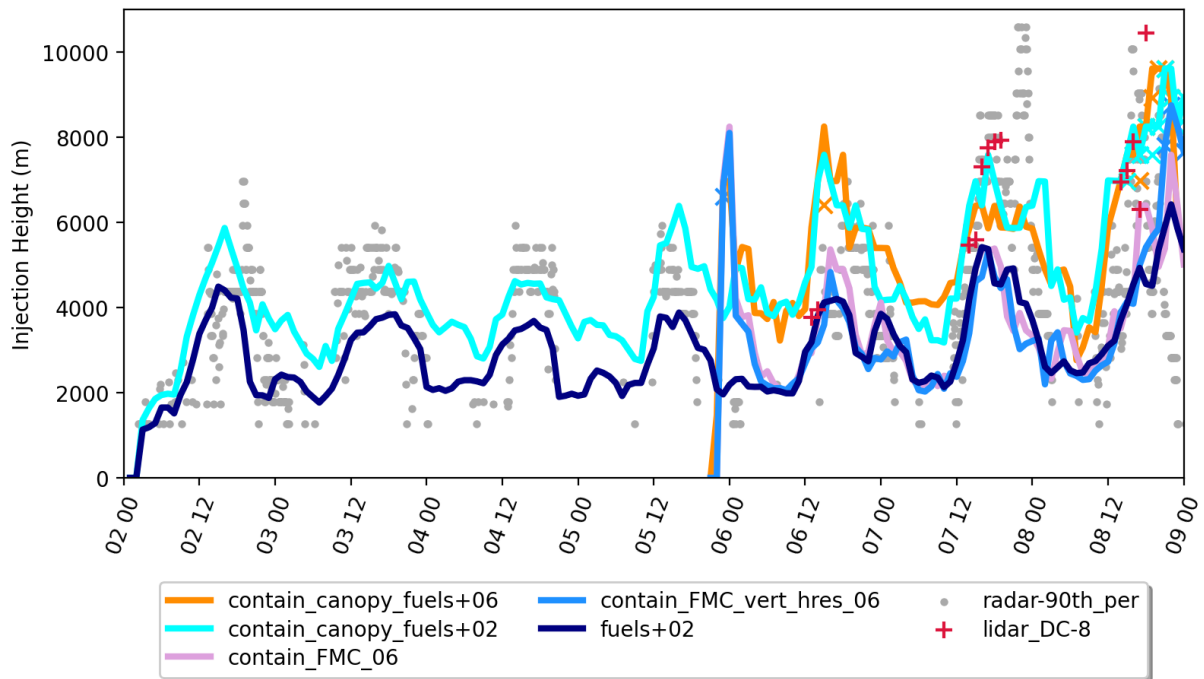
Figure 3.6. Smoke injection heights across the whole period of the 2019 Williams Flats Fire. Observations are the same as Figure 3.3.

In Figure 3.7, I show SkewT diagrams for HRRR and NAM driven simulations to illustrate

the difference between thermodynamic profiles in input and during simulation. The top row (a,

b) are profiles interpolated from the HRRR or NAM forcing meteorology in WPS (see Methods

2.2.2), while the bottom row are profiles after the simulation has run for multiple days. I

calculate the Convective Available Potential Energy (CAPE) for these profiles, which gives an estimate of the instability of the atmosphere and the potential for deep convection to occur. CAPE is calculated by lifting a surface parcel adiabatically until the lifting condensation level (LCL) and moist adiabatically after that until the upper-level inversion. The integrated buoyancy of that parcel is the CAPE [J/kg] and is largely a function of surface level moisture (or dew point), the surface temperature, and the location of upper-level inversion. The simulations in all cases lack sufficient surface level moisture compared to observations and thus underperform substantially on CAPE, but input conditions perform slightly better. This implies a drying out of the surface layer in simulation that is not reflected in observation. Using the NAM model as meteorological forcing seems to have made little difference in the CAPE or smoke injection heights, perhaps pointing towards input meteorology missing a large moisture transport event in the region. This is another potential reason for the mismatch between FRP and smoke injection heights.
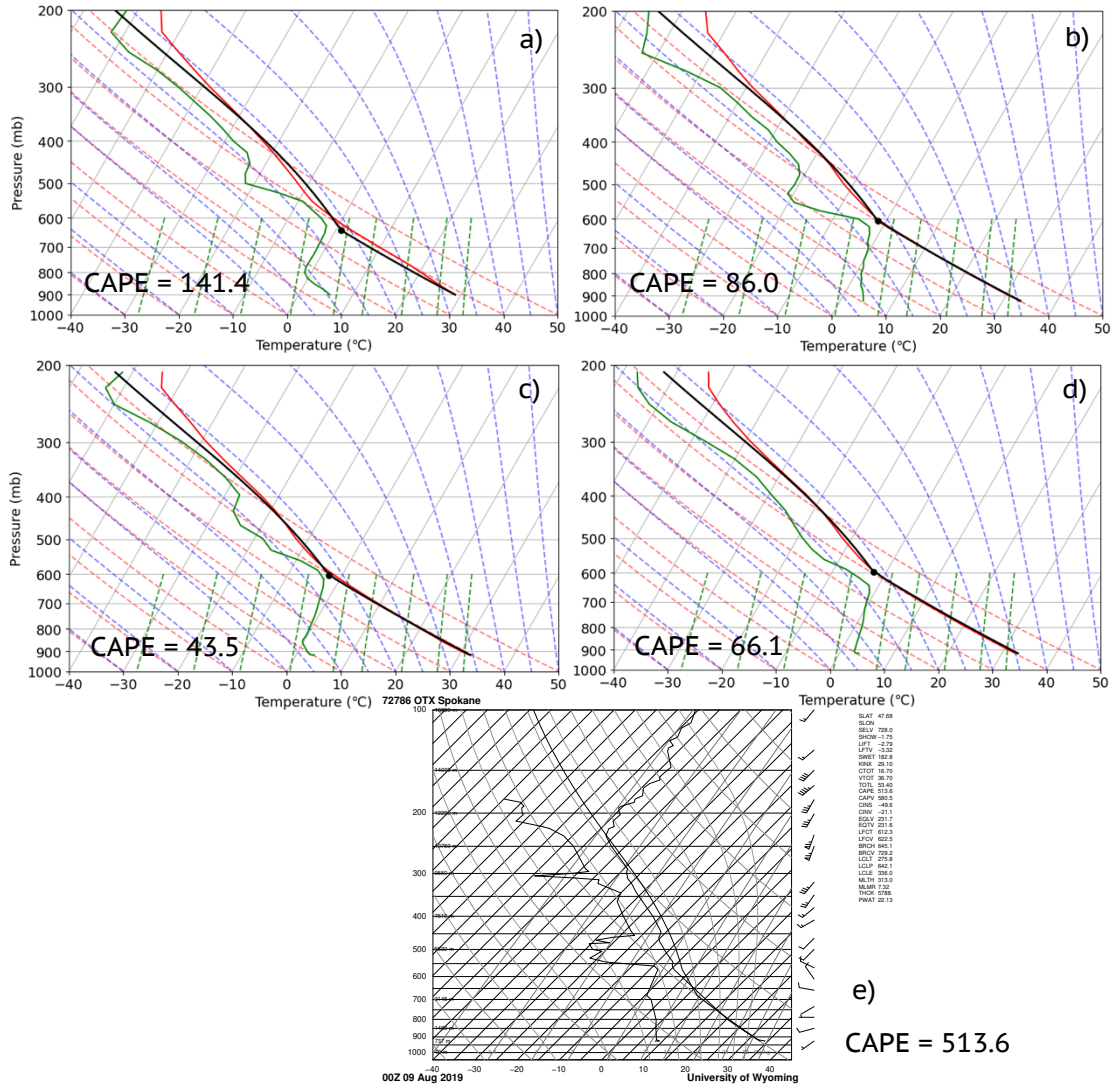
Figure 3.7) SkewT diagrams for HRRR driven simulations (a, c) and NAM driven simulations (b, d) on August 9th at 00:00 UTC (near pyroCb activity) to compare to previous analysis (Peterson et al. 2021, Figure 1), and OTX Spokane sounding e), where CAPE was found to be 513.6 J/kg. For (a-d), red curves are temperature and green curves are dew point, the same left-right orientation applies to temperature and dewpoint in e). Parcel path and lifting condensation level are drawn as black lines or dots respectively (a-d). Top charts (a, b) are after preprocessing, bottom charts (c, d) are from simulation output. The location chosen for SkewT in simulation is near the center of the final perimeter from Williams Flats Fire, although results were insensitive to exact location within the final fire perimeter.

In Figure 3.8, I show the ratio of smoke injection heights to FRP for my simulations and observations from Figures 3.3 and 3.4. This ratio quantifies the effectiveness of heat output in translating to deep injection heights, with background meteorology, horizontal/vertical resolution, and geometry of fire line potentially playing important roles. Here it can be seen that simulations with higher resolution (111 m horizontal, or 200 m improved vertical) perform better on this ratio, but simulations which achieve the best results on smoke injection height have poor ratios. This can be seen as a direct result of the vast overprediction of FRP from *canopy_fuels+* simulations in Figure 3.4, and perhaps implicates the vast underestimation of CAPE from Figure 3.7, or many unburnt sections within the fire perimeter from Figure 3.1 which could break up the fire front into smaller shapes (Figure 3.5).
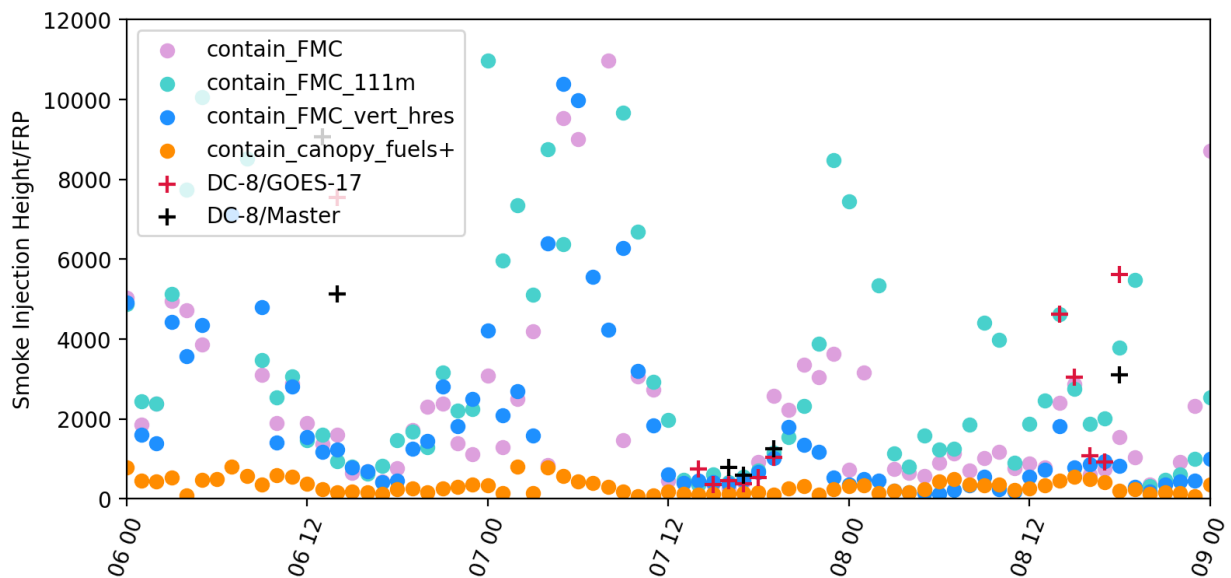
Figure 3.8) Smoke injection height to FRP ratio [m/GW] for the period of most intense fire at the Williams Flats Fire. Simulation output and observations are taken from Figure 3.3 and Figure 3.4.

In Figure 3.9 I show boundary layer heights and ratio of smoke injected above the

boundary layer to compare with observations taken over the Williams Flats Fire (Ye et al.,

2021). Boundary layer heights are taken as the height of the maximum gradient in vertical

moisture differences, the metric which most closely matched boundary layer heights visible in

SkewT plots in Figure 3.7. The ratio of smoke injected above the boundary layer is taken as the

instantaneous mass ratio across the boundary layer, normalized by corresponding wind speed

weights (to account for different residence times of smoke above and below the boundary

layer). Boundary layers and smoke injection ratios match observation well on the first few days

but smoke injection ratios are much lower for August 8th, keeping with a general trend of lower

smoke injection ratios over time. Overall, WRF-Fire simulations show lower smoke injection

fractions than what was observed (Ye et al., 2021, median observed LIDAR value = 85%),

although my *canopy_fuels+* simulations appear closer to observation than the plume rise model

analyzed (Ye et al., 2021, Figure 4).
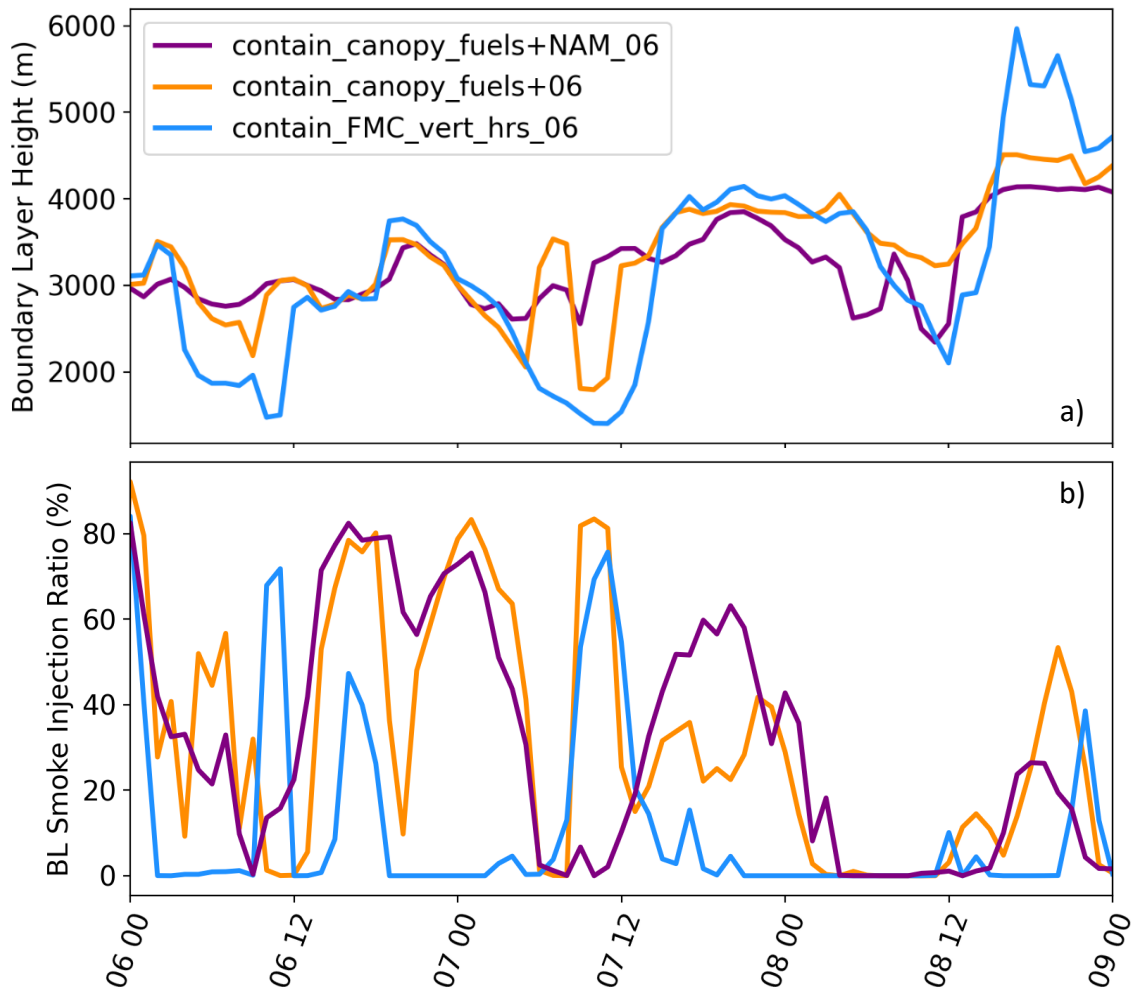
Figure 3.9) a) Time series of median boundary layer heights over the LES domain for the same period as Figure 3.3. and b) the ratio of smoke injected above the boundary layer compared to below. Simulations without the *NAM* designation used HRRR meteorological forcing.

3.4 Discussion and Conclusions

In this chapter I added to fuel depth increases to simulations from Chapter 2 to increase heat output and smoke injection height to realistic levels. This was accomplished by use of both an explicit canopy burning model, and an increase in the fuel depth of forested regions to an average depth of 50 cm. This resulted in pyroCbs forming in my simulations at roughly the right height and time, and with more accurate smoke injection heights across the simulation overall. With the increase of fuel depths up to 50 cm, the FRP was often overpredicted, but injection heights could often still be underpredicted during pyroCb activity, leading to poor smoke injection height to FRP ratios. Analysis revealed that refining a simulation's resolution, either horizontally or vertically, yielded better smoke injection height to FRP ratios, perhaps due to better resolved turbulent entrainment of the plume. Time series showed smoke injected above the boundary layer decreased over time in my simulations, and never got significantly above 80%, in contrast with slightly higher ratios in observation. The source of errors in these metrics were difficult to pin down, but a few key factors stood out.

In Figure 3.1 it was seen that many fuels within the fire perimeter remined unburnt, potentially breaking the coherency of the fire front (Figure 3.5) and leading to less deep fire fronts and shallower injection heights. The most likely cause of this is the fuel loading increases applied, as there is potential for stagnation shown as with the *crown* simulation (Figure 3.1). Although fuel depth increases were able to speed up the fire-spread alongside fuel density loading to a large degree, it appears not to have been enough to eliminate artificial stagnation across the entire domain. These large values of fuel loading and fuel depth were needed to

achieve accurate injection heights, but they may be overcompensating for incompleteness in my characterization of within *canopy* simulations. These deficits include at least lack of canopy burning threshold, lack of fuel moisture content heterogeneity (*FMC*), and lack of dynamic fuel moisture scheme (see Discussion 2.5). If these modeling deficits had been overcome in the *canopy* simulations, the fuel depths and loadings may not have needed to be increased to such an extent to achieve pyroCb conditions, fire fronts may have been more cohesive and FRP closer to observation, leading to better smoke injection height to FRP ratios. It is still possible that large increases in fuel depth and loading would be necessary even with the additions described, as WRF-Fire was not developed with intense pyro-convection (vertical winds > 10 m/s) in mind and disturbance of the fuel structure mid-fire by strong turbulence is not unreasonable to consider, despite a lack of investigation in the literature.

The second leading factor for bias in smoke injection height over FRP ratio is that of background meteorology, where CAPE was significantly underpredicted. The lack of surface level fuel moisture in my simulations led to low convective potential in comparison to observation, and likely contributed to my simulations to struggling to produce the deep injection heights seen during the Williams Flats Fire. I found that simulations tend to dry out over time when compared to the initial forcing meteorology (NAM and HRRR), which underpredicted CAPE themselves. This points to a potential land surface model or PBL scheme issue where moisture is either not released at the surface in sufficient quantities or is not distributed realistically into the middle layers of the atmosphere, although testing these model sensitivities was beyond the scope of this chapter. The quality of forcing meteorology in terms of surface moisture accuracy could have been could have been at fault as well, but a fair deal of

research may be needed to understand the problem if the error is in synoptic or mesoscale

meteorology.

Chapter 4

Factors Influencing the Formation of Pyrocumulonimbus

Clouds over the 2020 Creek Fire

4.1 Introduction

Pyrocumulonimbus clouds (pyroCbs), or fire generated storms, have come into the spotlight in recent years for their potential to inject smoke deep into the atmosphere in similar magnitudes to volcanos (Katich et al., 2023; Peterson et al., 2017). Nearby cities and often entire regions can be blanketed in smoke for weeks when fires begin to generate pyroCbs (Nolan et al., 2021), making their potential increase under climate change a serious hazard to consider. Although many studies have attempted to understand the causes and effects of pyroCbs (Couto et al., 2024; Katich et al., 2023; Levin et al., 2021; Ma et al., 2023; Salas-Porras et al., 2022), few studies have attempted fully coupled fire-weather simulations to investigate their mechanics (Couto et al., 2024; Lee et al., 2023; Simpson et al., 2014) and often these models use idealized configurations to control the complexity of the many different influencing factors.

In Chapter 3 I showed that getting pyroCb smoke injection heights in a realistic range for the coupled fire-weather model WRF-Fire over the 2019 Williams Flats Fire was possible using increased fuel loads, fuel depths, and a newly developed canopy model (Shamsaei et al., 2023). Although the Williams Flats Fire injected smoke to around ~10 km other fires have been known

to inject smoke into the stratosphere and thus potentially have added complexity

mechanistically. The 2020 Creek Fire was one such fire, which saw smoke injected into the

stratosphere (~16 km) and fire generated tornadic vortices on the first day of the fire (Lareau et

al., 2022). There has also been substantial evidence linking bark beetle activity in the region to

the extreme fire activity (Lee et al., 2023; Stephens et al., 2022) adding to the potential

understanding that can be gained from investigations of the this fire.

Here I deviate from other studies which ran idealized simulations of the Creek Fire with

WRF-Fire (Lee et al., 2023) by allowing fire-spread to freely propagate in my coupled-fire spread

model for the 2020 Creek Fire. I also deviate from previous pyroCb simulation studies (Couto et

al., 2024; Lee et al., 2023) by adding the canopy model and fuel properties from Chapter 3 to

my simulations and igniting fires from VIIRS satellite retrievals. My main objectives here are

thus to determine which factors drive deep smoke injection heights and pyroCb activity for the

2020 Creek Fire and to see whether a fully coupled fire-weather model with a freely evolving

fire front can capture the extreme pyroCb activity seen during the Creek Fire.

4.2 Methods

The simulation configurations for this chapter largely follow the established methods in

Chapters 2 and 3 but for the 2020 Creek Fire, a much bigger fire which required some numerical

stability accommodations. The 2020 Creek fire burned nearly the same amount of area on the

first day as the 2019 Williams Flats Fire did for over its life span and the fire reached smoke

injections heights of about 16 km, implying a much larger heat release and rate of spread.

Under these circumstances, It's reasonable to expect a more intense turbulent regime in which the updrafts and wind speeds reach much higher values as well (Rodriguez et al., 2020) and indeed fire generated tornadic vortices were captured by radar data on the first day of the fire (Lareau et al., 2022). Due to these high winds, the LES domain's horizontal resolution from Chapter 2 and Chapter 3 (200 m) resulted in instability in the model and violation of the CFL condition (see Methods 2.2.1). This forced us to use the global 9 s NLCD topography to drive the LES domain (as opposed to high resolution 30 m topography from the LANDFIRE database) and to push the horizontal resolution up to 240 m to maintain numerical stability not violate the CFL condition. Pushing to smaller time steps is not currently possible with the dependance of fire spread on time step described in the Supplemental Section A.2. At coarse horizontal resolutions like 240 m, the LES simulation may struggle to accurately capture turbulent winds in the atmospheric boundary layer or the entraining plume (Chapter 1, Supplemental Section; Chapter 2), although the impact on my results is difficult to say as the model is unstable at resolutions finer than this. The broader implication of this resolution change is that tradeoffs are needed for WRF-Fire to simulate both the turbulent boundary layer and the massive convective plumes and possible tornadic activity that result from a simulated fire such as the Creek Fire, but this could be perhaps eliminated in the future by fixing the dependence of fire spread on time step.

The 2020 Creek fire is notable not only for its massive pyroCb that formed but also for the large extent of bark beetle mortality in the region and its likely impact on fire activity (Stephens et al., 2022). Studies have indicated that under bark beetle infestation and mortality, forested regions tend to see a drop in canopy fuels and an increase in surface fuels (Bright et al., 2017) as trees lose dying branches and leaves to the ground. Here I follow Chapter 2 and 3

70

in using increased fuel loadings from FINN and relevant field studies (Keifer et al., 2006; Wiedinmyer et al., 2011) but increase fuel depths up to 1 m (Table 4.1), which is roughly in line, both in fuel depth and loading, with other studies increasing fuel properties to account for bark beetle mortality (Lee et al., 2023). An average fuel depth of 1 m is well above literature values (Donato et al., 2013; Hoffman et al., 2011) but a doubling of fuel depth 5 years post outbreak is possible (Hoffman et al., 2011) which implies a somewhat high level of variability possible in reality. In combination with these studies, 1 m fuel depth was chosen as it was found to be capable of achieving deep smoke injection heights while maintaining reasonable heat output and fuel loadings. I did not reduce the canopy fuel loads to reflect bark beetle mortality, partially because of the uncertainty already present in my canopy model and the data, and partially because it would have led to lower smoke injection heights. Note that surface fuel loadings are about 4 times higher than canopy fuel loadings in my simulations.

	Scott-Burgan	Scott-Burgan FINN	Fuel Depth
15: Short, Sparse Dry Climate Grass (Dynamic) [GR1 (101)]	0.02	0.25	0.12
16: Low Load, Dry Climate Grass (Dynamic) GR2 (102)	0.02	0.25	0.30
17: Low Load, Very Coarse, Humid Climate Grass (Dynamic) [GR3 (103)]	0.02	0.25	0.61
18: Moderate Load, Dry Climate Grass (Dynamic) [GR4 (104)]	0.06	0.62	0.61
19: Low Load, Humid Climate Grass (Dynamic) [GR5 (105)]	0.09	0.99	0.46
20: Moderate Load, Humid Climate Grass (Dynamic) [GR6 (106)]	0.02	0.25	0.46
21: High Load, Dry Climate Grass (Dynamic) [GR7 (107)]	0.22	2.47	0.91
22: High Load, Very Coarse, Humid Climate Grass (Dynamic) [GR8 (108)]	0.11	1.24	1.22
23: Very High Load, Humid Climate Grass (Dynamic) [GR9 (109)]	0.22	2.47	1.52
24: Low Load, Dry Climate Grass-Shrub (Dynamic) [GS1 (121)]	0.04	0.66	0.27
25: Moderate Load, Dry Climate Grass-Shrub (Dynamic) [GS2 (122)]	0.11	1.66	0.46
26: Moderate Load, Humid Climate Grass-Shrub (Dynamic) [GS3 (123)]	0.07	1.00	0.55
27: High Load, Humid Climate Grass-Shrub (Dynamic) [GS4 (124)]	0.43	6.30	0.64
28: Low Load Dry Climate Shrub (Dynamic) [SH1 (141)]	0.06	0.83	0.30
29: Moderate Load Dry Climate Shrub [SH2 (142)]	0.30	4.48	0.30
30: Moderate Load, Humid Climate Shrub [SH3 (143)]	0.10	1.49	0.73
31: Low Load, Humid Climate Timber-Shrub [SH4 (144)]	0.19	2.82	0.91
32: High Load, Dry Climate Shrub [SH5 (145)]	0.81	11.95	1.83
33: Low Load, Humid Climate Shrub [SH6 (146)]	0.65	9.62	0.61
34: Very High Load, Dry Climate Shrub [SH7 (147)]	0.78	11.61	1.83
35: High Load, Humid Climate Shrub [SH8 (148)]	0.46	6.80	0.91
36: Very High Load, Humid Climate Shrub (Dynamic) [SH9 (149)]	1.01	14.93	1.34
37: Low Load Dry Climate Timber-Grass-Shrub (Dynamic) [TU1 (161)]	0.04	0.86	0.95
38: Moderate Load, Humid Climate Timber-Shrub [TU2 (162)]	0.21	4.08	1.58
39: Moderate Load, Humid Climate Timber-Grass-Shrub (Dynamic) [TU3 (163)]	0.25	4.73	2.05
40: Dwarf Conifer With Understory [TU4 (164)]	1.01	19.34	0.79
41: Very High Load, Dry Climate Timber-Shrub [TU5 (165)]	0.90	17.19	1.58
42: Low Load Compact Conifer Litter [TL1 (181)]	0.22	10.81	0.32
43: Low Load Broadleaf Litter [TL2 (182)]	0.31	6.02	0.32
44: Moderate Load Conifer Litter [TL3 (183)]	0.11	21.62	0.47
45: Small downed logs [TL4 (184)]	0.11	2.15	0.63
46: High Load Conifer Litter [TL5 (185)]	0.26	24.86	0.95
47: Moderate Load Broadleaf Litter [TL6 (186)]	0.54	10.31	0.47
48: Large Downed Logs [TL7 (187)]	0.07	1.29	0.63
49: Long-Needle Litter [TL8 (188)]	1.30	24.92	0.47
50: Very High Load Broadleaf Litter [TL9 (189)]	1.49	28.57	0.95
51: Low Load Activity Fuel [SB1 (201)]	0.34	6.45	1.58
52: Moderate Load Activity Fuel or Low Load Blowdown [SB2 (202)]	1.01	1.01	0.30
53: High Load Activity Fuel or Moderate Load Blowdown [SB3 (203)]	1.23	1.23	0.37
54: High Load Blowdown [SB4 (204)]	1.18	1.18	0.82

Table 4.1: Fuel loadings in kg/m^2 for "Scott-Burgan" and "Scott-Burgan FINN". Fuel depths in m for an average fuel depth of 1 m in forested regions. The first 14 fuel categories are not used by the Scott-Burgan 40 fuel category model in WRF-Fire.

Because the Creek Fire grew so rapidly on the first day, there is no NIROPS perimeter to start from, so again I deviate from Chapter 2 and 3 in the ignition method. Here I used the VIIRS morning (03:00 PDT September 5th) and afternoon (14:18 PDT September 5th) retrievals to start a real fire ignition. Inside the retrieval perimeter, I write negative values into the "LFN_HIST" variable in "wrfinput_d02" to ignite the fire, no-fuel values into the "NFUEL_CAT" variable to remove the already burnt fuel, and 101 values (grass fire, see Table 4.1) into the "NFUEL_CAT" variable near the edge of the perimeter to create a grass fire ignition. I chose grass to ignite the fire as it has low fuel loadings and depths, which reduced the unrealistic heat output (Figure 3.6), smoke injection heights, and fire-spread during ignition.

The simulations chosen for this chapter are described in Table 4.2 and are in part derived from Chapter 2 and 3. The *FMC* simulation uses the fuel moisture code and fuel loading increase from chapter Chapter 3 (*FMC),* the *canopy_fuels+_2014* simulation uses the canopy code and fuel loadings from the Chapter 3 *fuels+* simulations but fuel depth is increased to 1 m in forested categories (Table 4.2), horizontal resolution is set to 240 m, the fire is ignited from VIIRS perimeter at 003:00 PDT September 5th, and the fuel category and canopy data is taken from the 2014 LANDFIRE collection. The *canopy_fuels+_2016* simulation copies this configuration except it uses 2016 collection from LANDFIRE. The *canopy_base_2016* copies this configuration but without the fuel depth or fuel loading increases. Simulations with *afternoon* in the description are ignited from VIIRS perimeter at 14:18 PDT September 5th, just before the pyroCb. The *canopy_fuels+_2014_circ* simulation was a simulation were a modification of the

VIIRS perimeter resulted in an ignition shape that was more circular than the other simulations and will prove instructive later.

	Fuel Moisture	1 m Fuel Depth	FINN Fuel Loadings	Canopy Model	2014 Fuels	2016 Fuels	Circular Ignite
FMC	✓			✓			
canopy_fuels+2014		✓	✓	✓	✓		
canopy_fuels+2014_circ		✓	✓	✓	✓		✓
canopy_fuels+2016		✓	✓	✓		✓	
canopy_base_2016				✓		✓	

Table 4.2: Table of simulation configurations used in Chapter 4. "Fuel Moisture" refers to static, satellite derived, fuel moisture maps from NCAR. "1 m Fuel Depth" refers to average fuel depth in forested regions set to 1 meter. "FINN Fuel Loadings" refers to fuel loadings averages set to representative FINN values. "Canopy Model" refers to new fuel model out of University of Nevada, Reno (Shamsaei et al., 2023). "2014 Fuels" refers to fuel data from LANDFIRE from the 2014 collection, "2016 Fuels" being from the 2016 collection. "Circular Ignite" is a slightly different ignition shape that is more circular.

4.3 Results

In Figure 4.1, I show wildfire perimeters after a day of burning to illustrate the accuracy and effects of different configuration options. Daily burned area was comparable to NIROPS for all configuration options, but co-location of fire perimeters with observation was flawed. Simulations ignited on the morning of September 5th (Figure 4.1a) tended to burn towards the northeast while NIROPS depicts the fire was burning due north from its ignition point (approximately center the first VIIRS retrieval). By contrast, simulations ignited on the

afternoon of September 5th (Figure 341b) tended to align better with the shape of the first

NIROPS perimeter, perhaps owing to the similar shape of the afternoon VIIRS and nighttime

NIIROPS retrievals (Figure 4.1b, blue-gray area and red perimeter). I note that a smaller river

running north/south along the creek could have prevented fire from spreading more accurately

as well, as there is no formulation for fire spotting in the code. Increasing fuel loading and

depth (1 m average in forests) in the *canopy_fuels+* simulations created larger daily burned

areas when compared to the *canopy_base_2016* or *FMC* simulations (Figure 4.1a). This leads to

a slight overestimation of daily burned area in Figure 4.1a and a large overestimation of burned

area in Figure 4.1b. In the process of re-running simulations for data collection, I discovered

that duplicate *fuels+* runs produced slightly different fire-spreads, which was not true for

duplicate runs with canopy models (Figure 4.2) or previous work (Chapter 2 and 3). This

suggests a numerical error associated with the increase in fuel properties rather than the

canopy code itself.
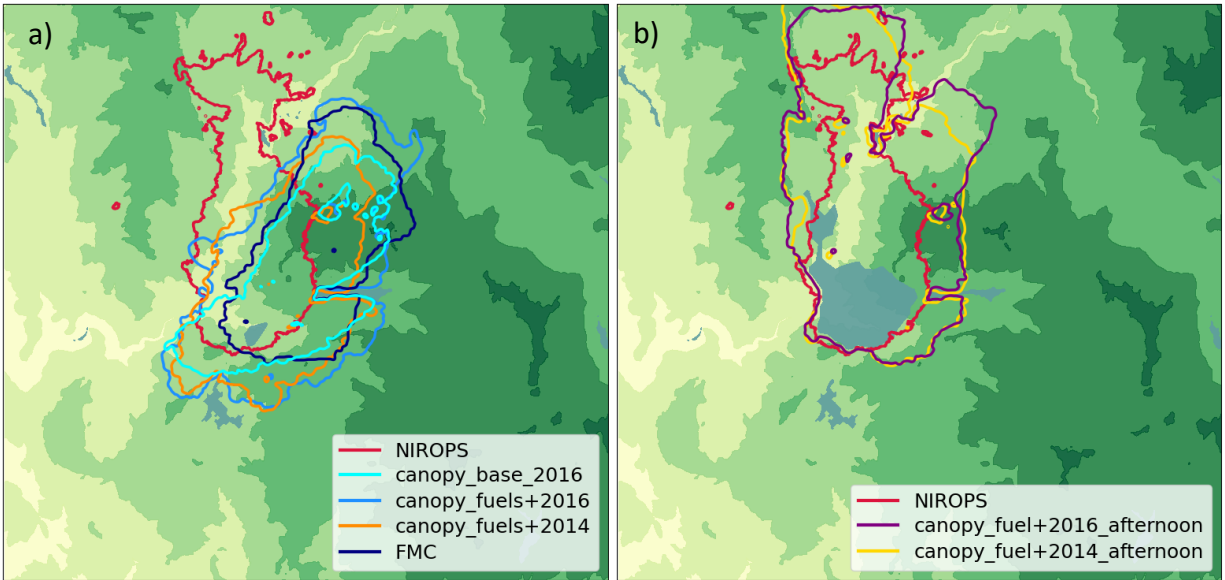
Figure 4.1: Fire perimeters over contours of altitude for WRF-Fire simulations vs NIROPS aircraft retrieval on 21:00 PDT Sept 5th, 2020 beginning on either 03:00 PDT Sept 5th (a) or 14:18 PDT Sept 5th (b). Blue-gray polygons at the center of fire perimeter indicate no-fuel regions where fires are ignited from VIIRS retrievals around their edges. Note the greater fire spread from *fuels+* simulations in a).
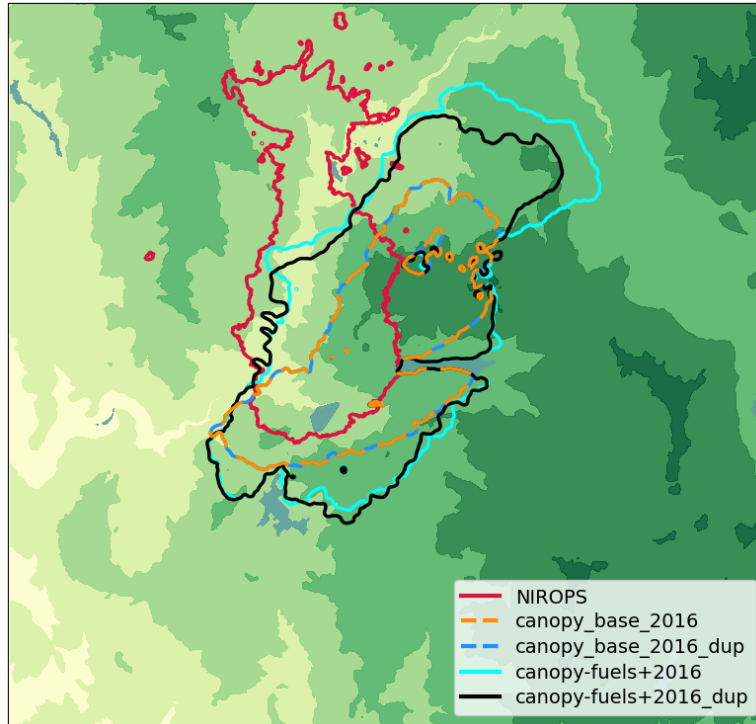
Figure 4.2: Fire burn perimeters approximately a day into the fire. Simulations with _dup_ are duplicate simulations of configurations without the label. _canopy_base_2016_ duplicate simulations are exactly on top of each other, while _canopy_fuels+2016_ duplicate simulations show a difference in fire spread due to the increase in fuel properties.

For initial visualizations of the vertical dimension of Creek Fire simulations, I show cross sections of contoured smoke height during a pyroCb event (Figure 4.3). This figure establishes the presence of pyrocumulonimbus clouds formed by WRF-Fire, with large smoke-filled updrafts injecting smoke and creating ice clouds above 15 km. Smoke cloud shelfs at the PBL can be seen as well as large regions of smoky air within the mixed layer. In Figure 4.3, ice clouds appear to be advected downwind and drawn into a turbulent wake at high altitudes; this was seen in many simulations. Interestingly, the ice cloud in the wake appears smaller than its

enclosing smoke plume, implying a potentially temporary nature to the ice clouds in my

simulations similar to previously described frameworks (Couto et al., 2024).
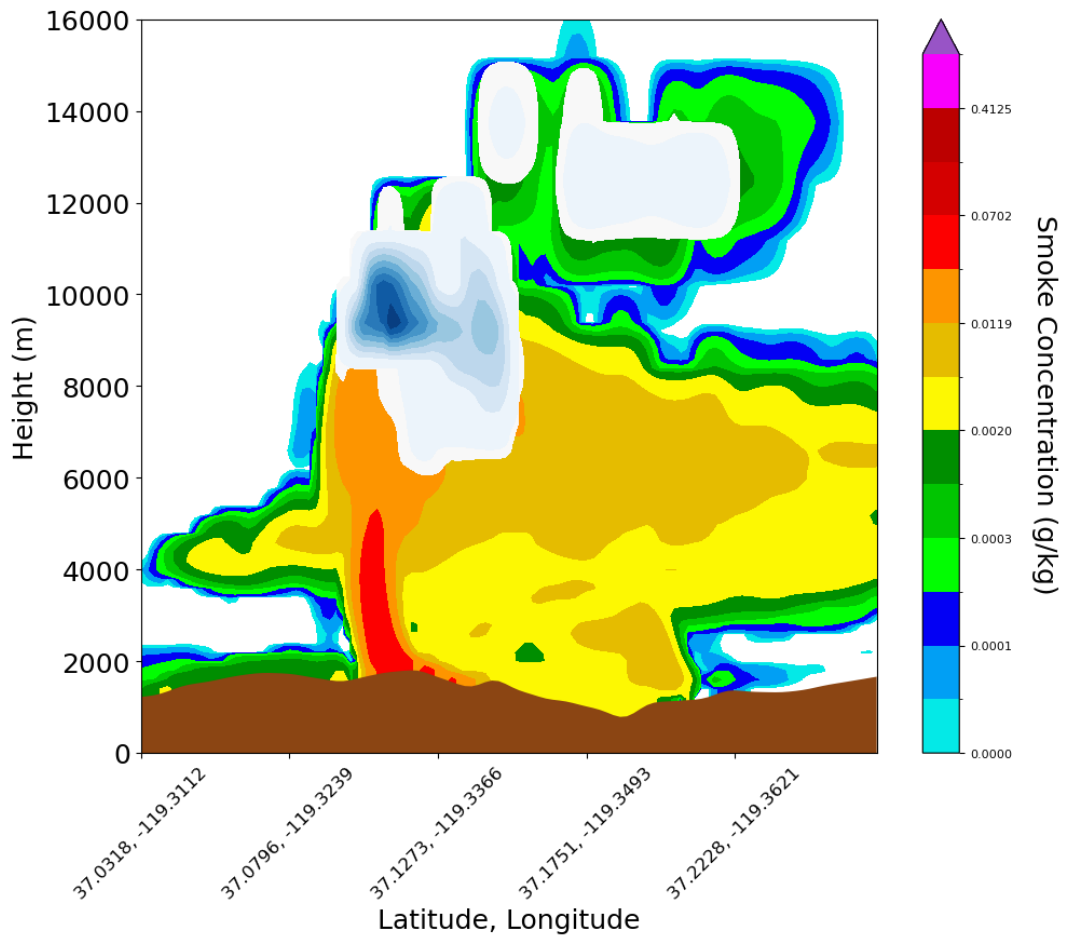
Figure 4.3: Cross section from a *canopy_fuel+2016* simulation during a pyroCb event at 02:00 PDT Sept

6th. Multicolored contours are smoke mixing ratios, while ice cloud mixing ratios are shown in blue

contours. Water clouds were also present in the cross section co-located with the ice clouds. Note the

low resolution at the top of the domain and the shelf of smoke near 5 km where the boundary layer is.

In Figure 4.4, I visualize the evolution of the smoke plume over time with a times series of smoke injection heights and ice cloud tops. Simulations trended upwards on smoke and ice heights over time, reaching unrealistic values toward the end of the simulations as the fire-weather feedback perhaps grew unstable (see Methods 4.2). With that in mind, most of the conclusions should be drawn from within the first day where values are reasonable. Most importantly, configurations with the *fuels+* designation reach considerably higher smoke injection heights and ice cloud tops than simulations without (*FMC, canopy_base_2016)*, reaching maximum injection heights of 15-18 km over the first day, which roughly corresponds with radar observation (Lee et al., 2023) and constitutes extreme pyroCb activity simulated within the coupled fire-weather framework. The best performing simulations were *canopy_fuel+2014* simulations, with the *circ* and *afternoon* designations coming very close to observed smoke injection height on the afternoon of Sept 5th. In general, *canopy_fuel+2016* simulations seem to inject too deeply at first. The duplicate *canopy_fuels+2014* (*_dup*) reveals relatively little change in smoke injection height due to numerical error and was representative of the typical change in duplicate *canopy_fuels+* simulations regardless of data year. Many of the simulations seem to lack diurnal activity, possibly because of the lack of dynamic fuel moisture scheme.
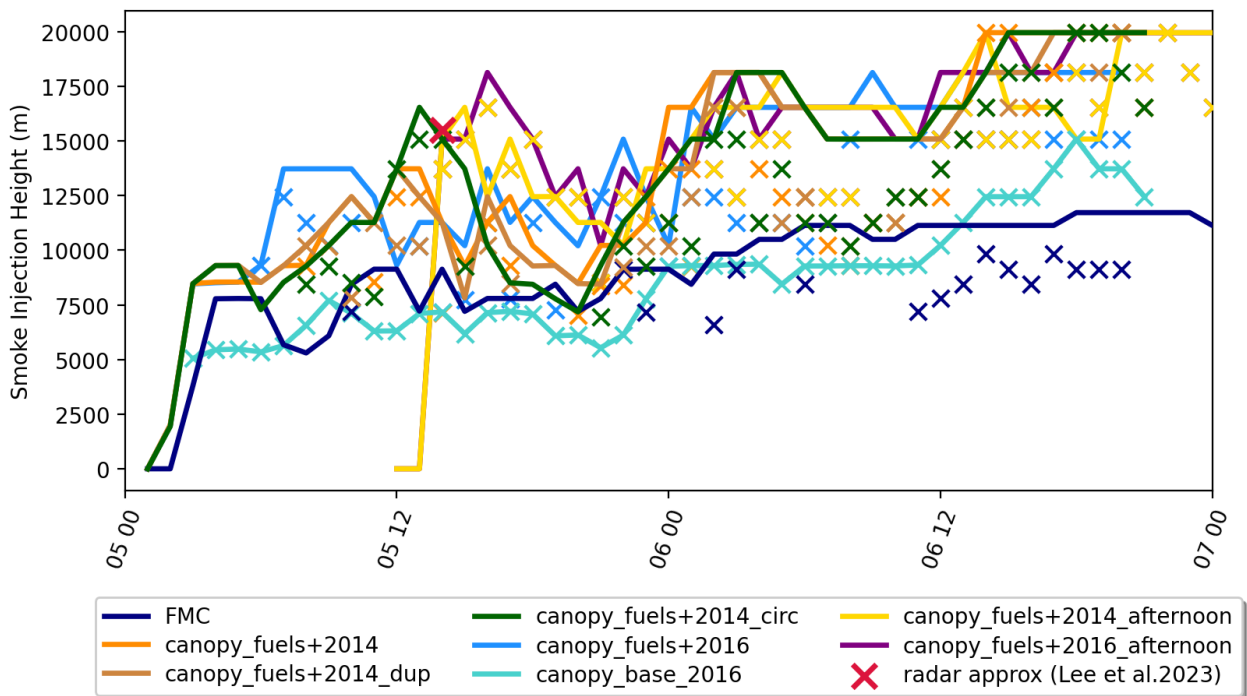
Figure 4.4: Smoke injection height times series as solid lines and ice cloud top heights as "X" from Sept 5th 2020 to Sept 7th 2020. Each smoke injection height is determined to be the height of the highest smoke cell in the inner domain above 1×10^{-7} g/kg air. Each cloud top height is the height of the highest cell with ice cloud mixing ratio above 0.

In Figure 4.5, I compare the Fire Radiate Power FRP of a few simulations which generated pyroCbs to doppler radar estimated FRP (Saide et al., 2023). Doppler radar estimates were chosen in this case as satellite retrievals are expected to underpredict FRP when pyroCbs form above the fire obscuring the heat signal. *Fuels+* simulations overestimate FRP while the others underestimate, neither achieving a high degree of agreement with observation during the first day of simulation. Although there are significant differences between simulation and

observation, radar estimates of FRP are a newly derived product with potentially unforeseen

uncertainties, and pyroCbs have been known to form upwards of 100 GW, so the distribution of

FRPs from my simulations is not outside the range of reasonable values for the first two thirds

of simulation time. The *canopy_fuels+2014_circ* simulation, while still overestimating, is only 85

GW above radar FRP at peak value on the first day, while the *canopy_fuels+2016* simulation is

144 GW above radar FRP at first day peak values, with max FRP from radar only reaching 184

GW. Because of its relatively accurate FRP while still maintaining pyroCb activity,

creek_fuels+2014_circ performs better on a smoke injection height/FRP ratio than other

simulations (Figure 4.6a).
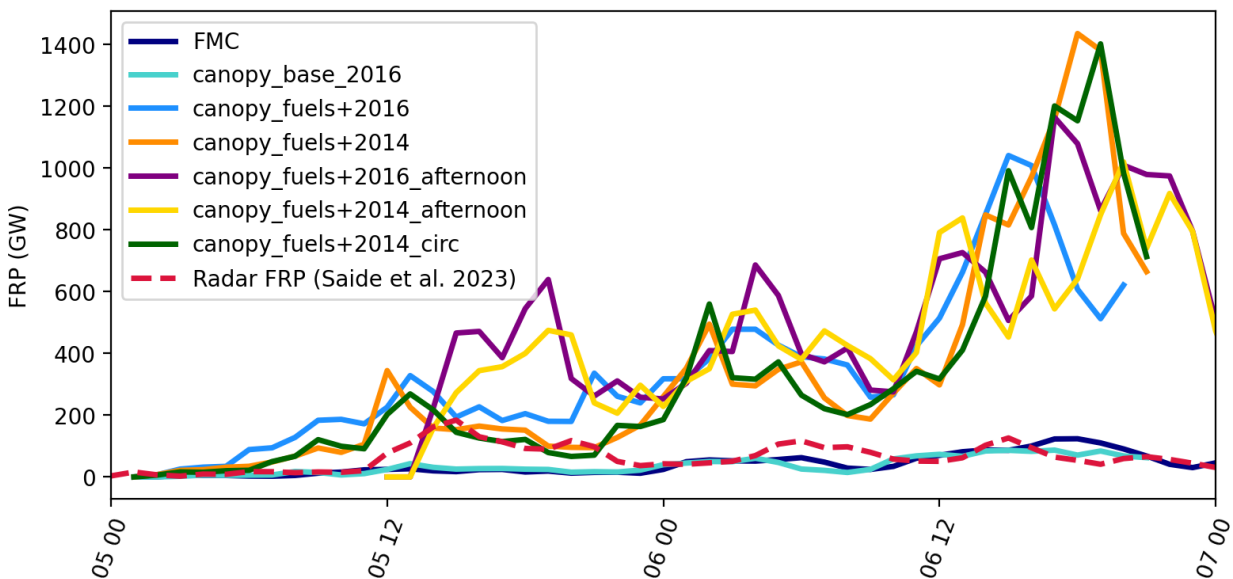
Figure 4.5: Fire radiate power FRP for simulations from Figure 4.4 against radar estimates (Saide et al.

2023). Max FRP retrieval from radar on the first day is 184 GW, while *fuels+* simulations ignited on 03:00

PDT Sept 5th, range from 269 to 344 GW over the same period.

To better understand the drivers behind PyroCb events in simulation I track the fire front and the conditions occurring within them. The fire front here was drawn as the maximum contour of heat flux data above 10 kW/m^2 (Figure 4.7a) and was chosen so that the contours would represent the whole length of burning perimeter but be broken into separate regions with the largest area representing the most intense burning, or the main fire front (Figure 4.7b). I show time series of average data within the main fire front for circle similarity (Figure 4.6b), wind speed at the lowest atmospheric cell (Figure 4.8), fuel loading (Figure 4.9), and fire front area (Figure 4.10) vs FRP. Circle similarity is defined as the ratio of area of the fire front to the area a circle would have given the perimeter of the fire front, making a score of 1 a perfect circle and scores near to 0 more like a line.
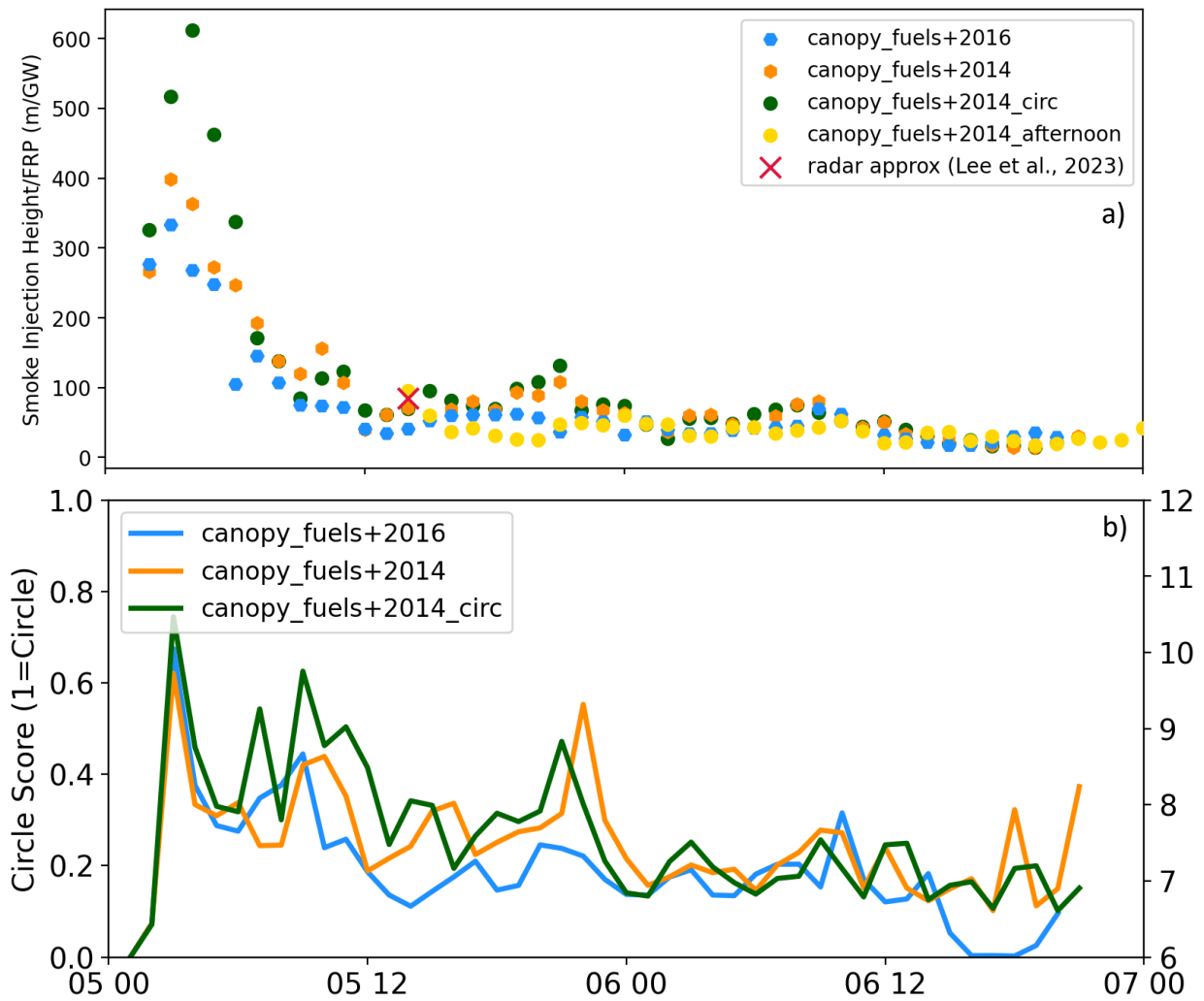
Figure 4.6: a) Smoke injection height vs FRP ratio time series for three instructive simulations and radar approximation (Lee et al. 2023). b) Circle similarity for the fire fronts of the same simulations as a). Circle similarity is defined as area of the fire front over the area a circle would have given the perimeter of the fire front, making a score of 1 a perfect circle and scores near to 0 more like a line. Note the better performance in Smoke Injection Height/FRP by the *canopy_fuels_2014* simulations in a), and the larger

circularity of their fire fronts in b). Note the similarity in behavior between a) and b) (Pearson correlation coefficient: *canopy_fuels+2014* = 0.50, pvalue = 0.00006, *canopy_fuels+2016* = 0.63, pvalue = 6.75x10^{-6}).
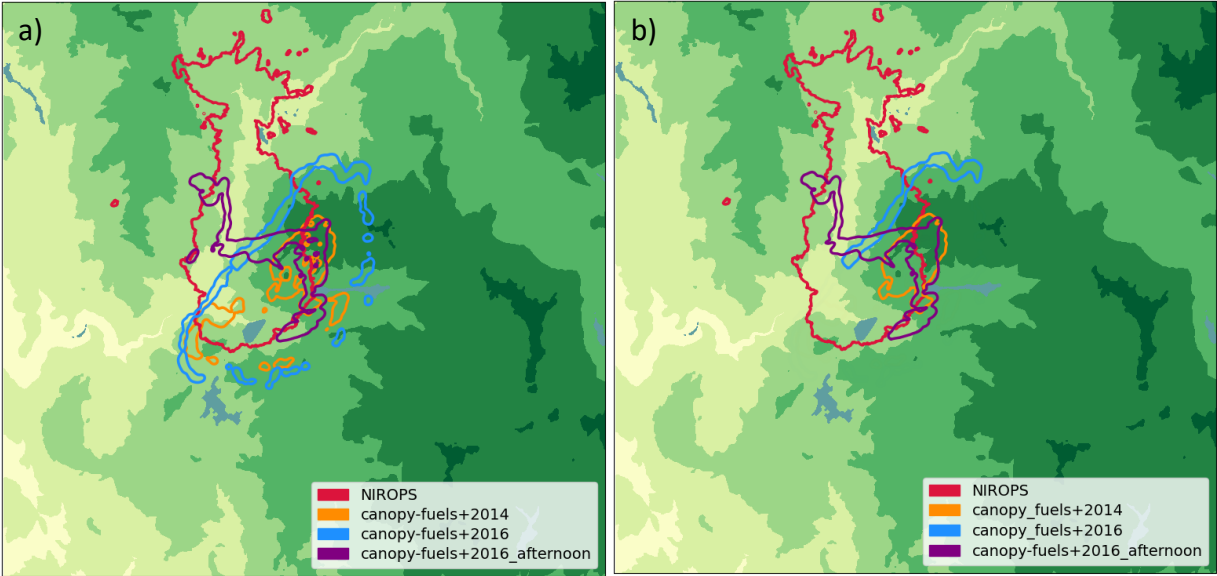
Figure 4.7: Iso-contours of heat flux at 10 kW/m^2 across the whole fire front (a), and of the contour with the maximum area (b). Times for these contours are chosen as each simulation's peak FRP time from Figure 4.5.
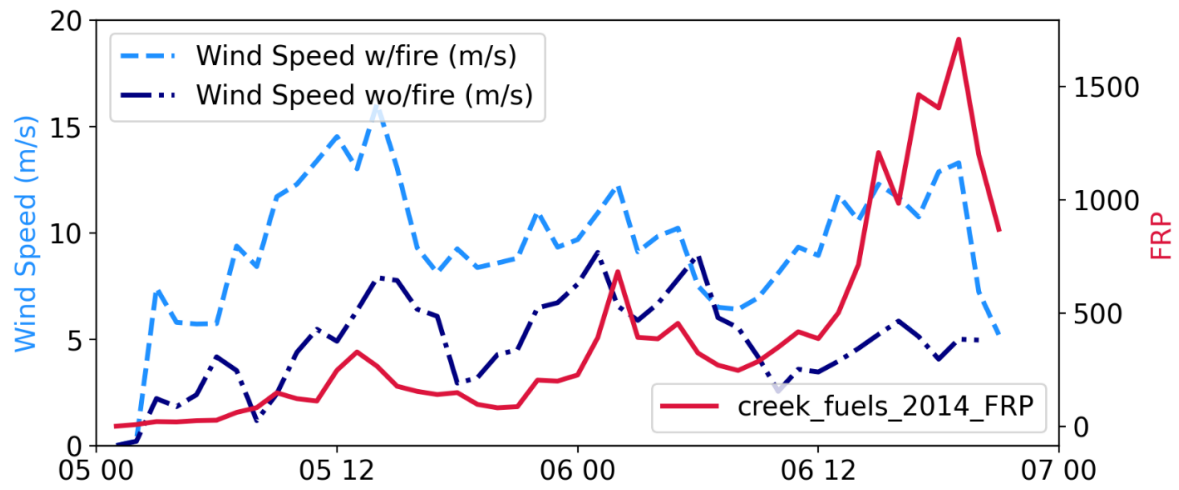
Figure 4.8: Time series of wind speeds in the first atmospheric cell across the fire front for the

canopy_fuels+2014 simulation. The light blue line shows wind speeds from the simulation with the fire

code turned on while the dark blue simulation has the fire turned off. FRP is plotted on the second axis.
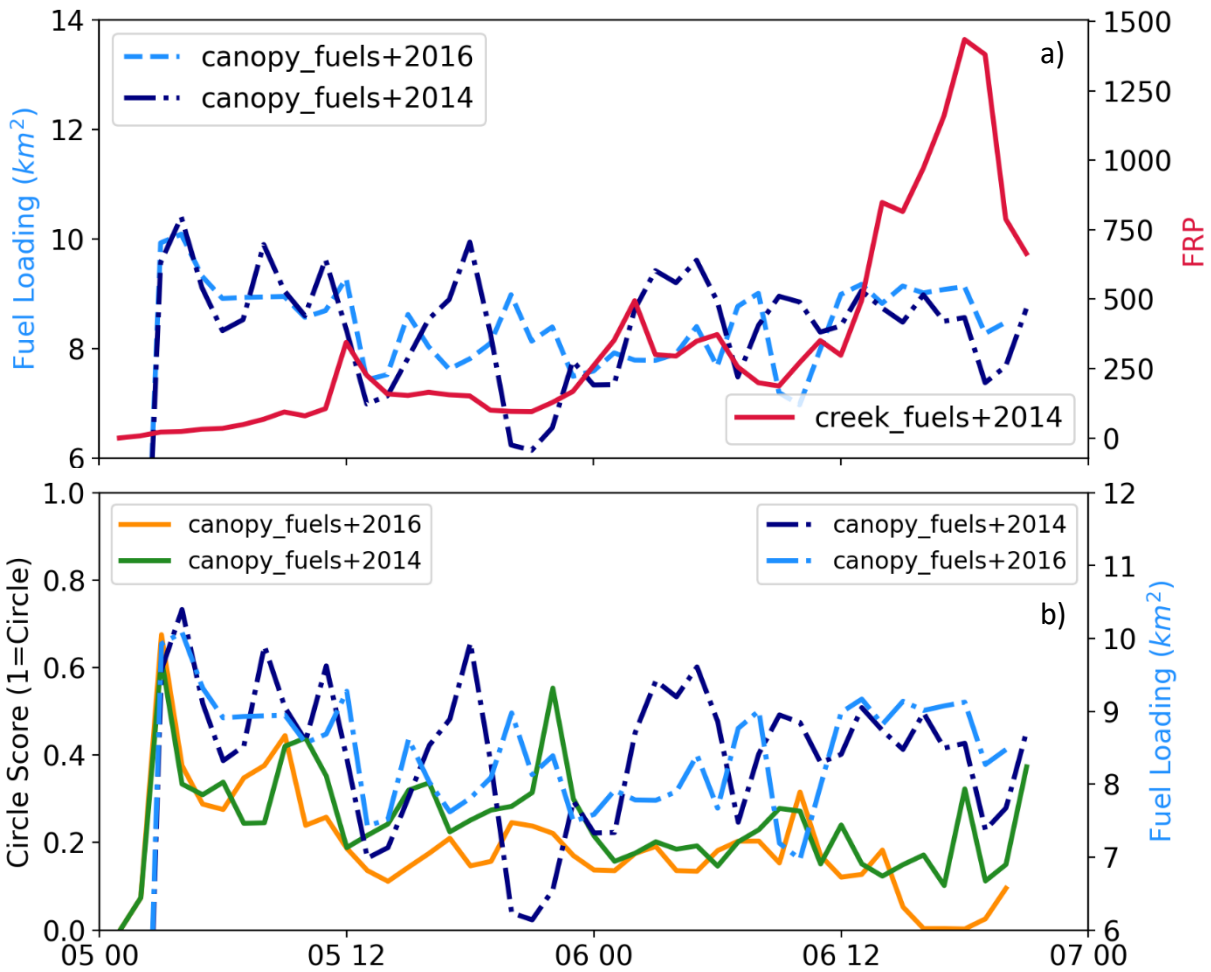
Figure 4.9: a) Time series of mean initial fuel loading for cells on fire within the fire front vs FRP for two pyroCb generating simulations. b) Time series of fuel loading and circle score on separate axis. Note the correlation between corresponding time series (PCC for *canopy_fuels+2014* = 0.36, pvalue = 0.015).
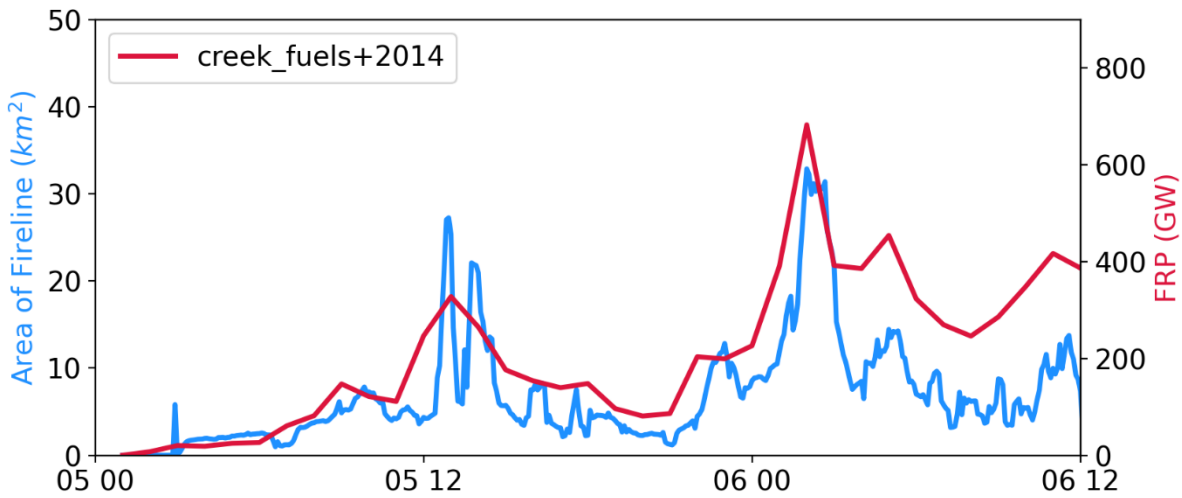
Figure 4.10: Time series of area of the fire front vs FRP for a pyroCb generating simulation.

When looking at key variables across the fire front of pyroCb generating simulations a few relationships become evident. In Figure 4.6 I show the downward trend in smoke injection height/FRP ratio and better performance of the *canopy_fuel+2014* simulation on that variable is correlated with the higher circularity of the fire front (PCC between the two times series = 0.50, pvalue = $6x10^{-5}$), most likely due to superior nature of a circular updraft in protecting its buoyant inner core from turbulent entrainment as it rises (Badlan et al., 2021b). This is spatially evident in Figure 4.7b where my method of isolating the main fire front reveals the circularity of the front during pyroCb activity, with the *canopy_fuels+2014* bring the most circular. Wind speed across the fire front shows a significant correlation with FRP (Figure 4.8) (PCC = 0.37, pvalue = 0.01) and are significantly enhanced by the fire-weather, more than doubling the wind speed during peak activity on the afternoon of September 5th. Mean initial fuel loadings seem

to dip across the fire line during peak FRP activity (Figure 4.9a) and correlate well with circle

score (Figure 4.9b) (PCC for *canopy_fuels+2014* = 0.36, pvalue = 0.015), implying that large

areas of shrub or grassland were burnt during high wind events, and that burning fuels with

higher fuel loadings results in more circular fire fronts. This is further backed by the observation

that the *canopy_fuel+2014* simulations burn through higher fuel loading fire fronts and have

higher circle scores than *canopy_fuel+2016* simulations in general (Figure 4.9). The fire area of

the fire front is highly correlated with FRP (Figure 4.10) but lags behind slightly most of the

time, implying heat release as the driving factor behind the wildfire spread rather than the

other way around.

For the *canopy_fuel+2014_circ* simulation, I show simulated cloud top divergence for a

pyroCb for the first time in the literature that I'm aware of (Figure 4.11). This is done to

investigate the relationship between divergence and max updraft speed, a potentially useful

satellite proxy. Only smoke or ice above 3300m is considered in this calculation and divergence

values at the edge of different cloud top height layers are excluded from the results as they

were always outliers and not reflective of the signal. Although the divergence values I show

here are about an order of magnitude higher than what recent satellite products have indicated

(McHardy et al., 2024, in review), the products are new and the horizontal resolution of the

satellite retrievals is in the kilometers range making analysis of uncertainties difficult. Despite

that, I show there is a strong relationship between maximum cloud top divergence and updraft

speed (Figure 4.12) making the possibility of a satellite derived proxy for updraft speed a more

tractable problem. Note that in Figure 4.12 the largest values of maximum divergence and

maximum updraft come in very short frequency bursts, reflecting the chaotic nature of pyroCb

updrafts in my simulations.
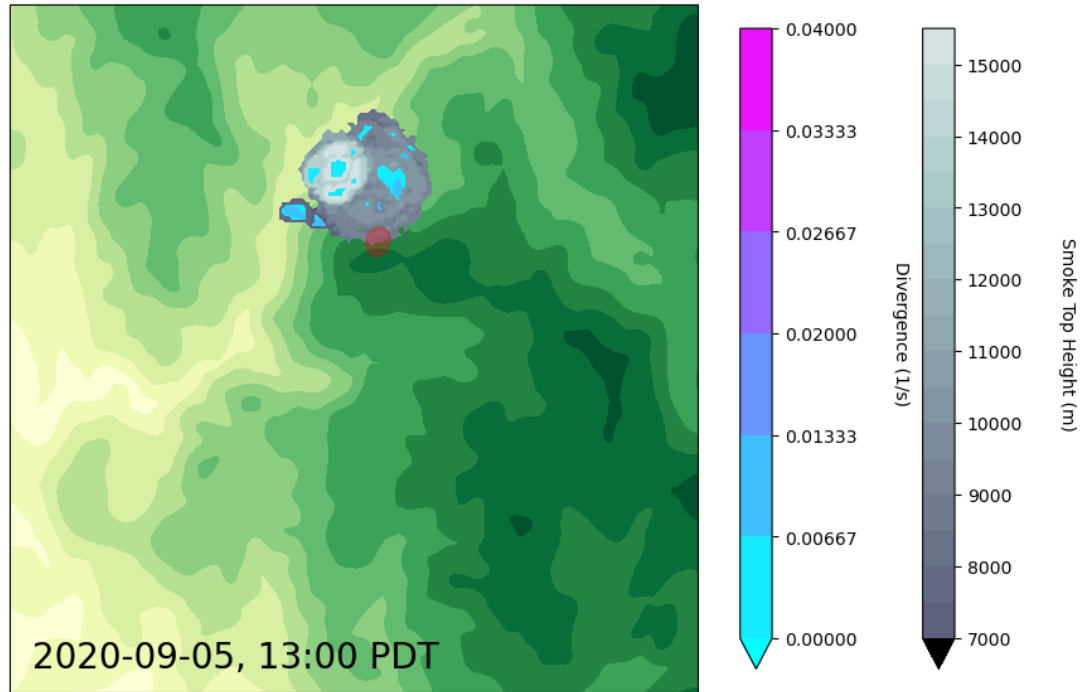
Figure 4.11: Snapshot of smoke injection height contours in the ice cloud of a pyroCb and divergence

contours across the cloud top for the *canopy_fuel+2014_circ* simulation. Only smoke or ice above

3300m is considered in this calculation and divergence on the edge of different smoke height layers is

excluded from the results. The red circle indicates the position of maximum updraft at the time of the

snapshot.
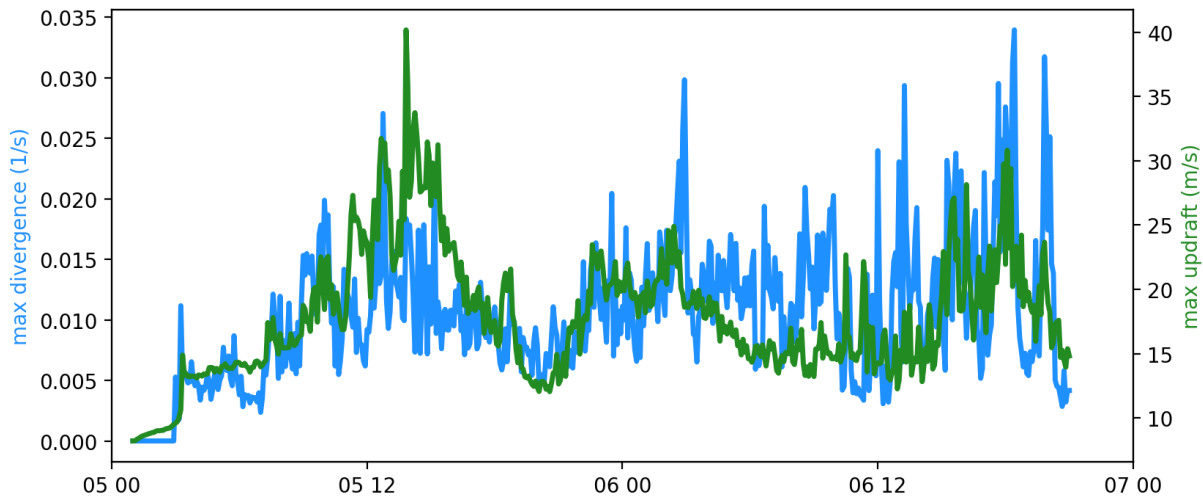
Figure 4.12: Time series of max divergence at the ice cloud top vs max updraft over 3300 m for the *canopy_fuels+2014_circ* simulation. Divergence values at the edge of different cloud top height layers are excluded from the results.

4.4 Discussion and Conclusions

Here I showed the first case of a fully coupled fire-weather model (WRF-Fire) capturing accurate pyroCb heights above ~15 km at roughly the right time. A newly developed canopy burning model (Shamsaei et al., 2023) was tested and was crucial for obtaining deep enough smoke plumes. I increased fuel depth in forested regions in WRF-Fire to reflect the presence of known bark beetle infestation in the region. Together, these two additions to the model proved enough to generate pyroCbs of similar depth to observation (~16 km). This is considerably closer to observation than other studies that included the effect of bark beetle mortality in their simulation of the Creek Fire (Lee et al., 2023) which did not account for canopy burning.

My *canopy_fuel+2014* simulation using 2014 fuel category and canopy data from LANDFIRE

showed the best results, capturing deep injection heights and not overestimating FRP by large

margins. I showed this was at least partially a function of higher fuel loads resulting in more

circular shaped fire fronts. My novel analysis into simulated cloud top divergence in pyroCb

reveals a strong relationship between cloud top divergence and updraft strength, opening the

door to further development of a proxy satellite product for updraft speeds during pyroCb

events.

I showed how altering fuel properties in WRF-Fire can play a role in achieving accuracy

in forecasting pyroCbs. Because of the large underestimation of smoke injection heights in

models without fuel depth increases linked to bark beetle infestations, it seems likely that

changes to the fuel structure from bark beetle mortality played a significant role in the

development of the deep pyroCbs during the 2020 Creek Fire. Although pyroCbs certainly form

without the influence of bark beetle, the Creek Fire was an extreme example, with injection

heights reaching around 15.5 km and currently holding the record for second largest burned

area from a single ignition fire in California behind the 2021 Dixie Fire. I showed the effect of

increasing the fuel depth and fuel loading at the same time was much higher FRP values and

smoke injection heights but also potential numerical instability in the model, likely due to the

high wind speeds pushing the model closer towards the CFL condition. Under fuel depth and

density increases, FRP and burned area were often overpredicted, indicating the need for a

canopy fire threshold to be implemented, or for a combination of other factor to be included

(i.e. fuel moisture models, fuel property accuracy, fire ignition improvements). I also note the

uncertainty in the values of fuel loadings and fuel depth associated with bark beetle infestation

in the literature (Hoffman et al., 2011; Lee et al., 2023; Stephens et al., 2022). Although I choose fuel depth values above what are reported in field studies, they are not outside what other studies have used and suggested possible (Lee et al., 2023), and were necessary in obtaining realistic smoke injection heights, further highlighting the uncertainty in changes to fuels during and after bark beetle infestations. Given that there were fire generated tornadic vortices during the creek fire (Lareau et al., 2022), it is also not unreasonable to suspect some disturbance to the fuel structure (fuel depth) despite its investigative absence in the literature.

Tracking variables across the fire front creates a better picture of how pyroCbs evolve in a coupled fire-weather simulation. I show circularity of the fire front is associated with increased smoke injection height to FRP ratio (Pearson Correlation Coefficient: *canopy_fuels+2014* = 0.50, pvalue = 6×10^{-5}, *canopy_fuels+2016* = 0.63, pvalue = 6.75×10^{-6}), owing to the ability of a circular convective plume to entrain less air and preserve buoyancy in assent. Circularity seems to decrease overtime for all simulations, implying that my best simulation on smoke injection height to FRP ratio may have grown relatively slowly initially and retained more circularity when winds picked up in the early afternoon. Indeed, the correlation between circle score and surface fuel loadings (Pearson Correlation Coefficient for *canopy_fuels+2014* = 0.36, pvalue = 0.015) suggest that fuels with higher loadings, such as forests and beetle kill regions, tend to create more circular fire fronts, while fuels with low loadings, like quick burning shrub and grasslands, tending towards more line-like fire fronts. This comports with the observation that circle score decreases over time as the fire line grows, showing that the general trend is for quickly expanding fires to be less circular when compared to slowly expanding fires. This adds to the existing literature on the causes of deep flaming

92

fronts (Badlan et al., 2021a) by suggesting that bark beetle infestation, and high fuel loadings in general, may also be considered driving factors. By extension, bark beetle infestations associated with climate change could be considered a positive climate feedback with increased fuel loads contributing to significantly deeper smoke injections.

I find that updraft speed and max divergence across the pyroCb top have a strong relationship although the magnitude of divergence is an order of magnitude lower than new satellite products (McHardy et al., 2024, in review). Although my horizontal resolution is much higher than what is available by satellite, my vertical resolution at the cloud top is quite coarse, and there is numerical instability likely caused by intense convective turbulence. More research is needed to discover the source of uncertainty in my modeled max divergence but the possibility of using max divergence at a satellite proxy for updraft speed is identified as a reasonable future endeavor.

Chapter 5

Conclusions

In this paper I explored the potential skill of a coupled fire spread model (WRF-Fire) to predict variables important to air quality modeling and emergency response. In Chapter 2, daily burned area and FRP were the main metrics investigated, and containment lines, fuel moisture content, and fuel loadings were found to be the most important input variables to capturing accuracy over the 2019 Williams Flats Fire. When all these factors were accounted for WRF-Fire could outperform persistence by ~30% over a 5-day forecast. In addition, fuel moisture dynamics were found to be linked to wildfire diurnal cycle. Expanding the analysis vertically over the 2019 Williams Flats Fire in Chapter 3, I aimed at prediction of smoke injection heights and fraction of smoke emitted above the boundary layer. Only by including a newly developed canopy burning code and increasing fuel depths to 50 cm on average in forested regions was I able to achieve realistic vertical distribution of smoke, although analysis revealed that CAPE was underpredicted and FRP overpredicted implicating a likely overcompensating effect. Moving this analysis to the 2020 Creek Fire, I looked for accuracy in smoke injection heights and deep pyroCb formation. The canopy formulation was again needed to achieve realistic smoke injection heights but fuel depth needed to be increased to 1 m on average in forested regions. This was justified and partly explained by the impact of bark beetle on the fuel structure of infested forests. The circularity of the fire front was found to be an important factor to achieving deep plumes with reasonable heat output and high fuel loads were implicated as a

causal factor.

The potential for WRF-Fire to be a valuable forecasting tool for air quality modeling is strong. With careful attention paid to meteorology and local fuel structure, simulations of WRF-Fire can outperform simpler models, but uncertainty in input conditions should be carefully evaluated in light of this research. Numerical error and long computational times were found at fine horizontal resolutions and small time steps, implicating the need to coarsen the resolution to as much as 240 m when forecasting large wildfires. This could limit the ability of WRF-Fire to accurately model plume rise and loss of buoyancy from turbulent entrainment but might be necessary for injection heights of as much as ~16 km. Ensemble forecasts and more accurate fuel models were also implicated as potential ways to improve skill.

Several important fundamental questions were addressed. For the 2019 Williams Flats Fire, containment efforts by wildland firefighter were likely effective in preventing a much bigger fire. Fuel depths needed to be increased to values higher than reported in field studies to achieve accurate smoke injection heights, implying missing meteorological instability or fuel representation. In addition, I found bark beetle infestation very likely played a role in the formation of pyroCbs over the 2020 Creek Fire, producing not only faster fire spread and more heat release, but also deeper, more circular fire fronts which led to deeper plumes. The increase in fire front circularity with higher fuel loads implicates both bark beetle and fire suppression as potential factors for deep fire fronts and pyroCbs.

Appendix A

Supporting Information for

Dissertation

Abstract

This supporting information provides a deeper understanding of the main text. Supplementary Section A.1 describes common turbulence/wildfire interactions that I see in my simulations, while Section A.2 describes a numerical parameter that my model is sensitive to and thus chosen carefully. Figures support these sections and provide additional data visualizations for simulations not shown in the main text. The table details the exact fuel densities that were used in my modeling in Chapter 2.

A.1 Turbulence and Wildfires

Although the effects of turbulence on wildfires are not completely understood, several well-known factors are represented in my simulations. One of the main mechanisms of fire-induced weather is a convective sink beneath the plume, drawing in air from all directions and inhibiting fire spread (Quaife & Speer, 2021). This effect is modulated by turbulence, as trains of

streamwise counter-rotating hairpin vortices in the PBL are drawn up by convection and become vertically aligned, leading to sub-regions of convergence and divergence along the fire line that result in fingering and fire whirls (Pagnini & Massidda, 2011). In addition, when the heads of the hairpins burst, they can bring down high-momentum air from above and sweep the fire front forward (Quaife & Speer, 2021). Mountain topography can also play a role in turbulence by tilting the shearing layer, forming mountain induced waves, and creating sharp temperature differences. Iplot iso-contours of Q-criterion (Supplemental Figures A.3-A.5), defined as vorticity minus shear, to qualitatively show that the interaction between background turbulence and convection is realistic: highly tilted counter-rotating vortices are formed over the fire line which terminate in bursting vortices.

A.2 Level Set Function Dependance on Time Step

During my testing of WRF-Fire, I discovered a dependance of fire spread on the discretization time step, shared by both the LES and fire model. In standard practice, I can expect small chaotic variations in model results from errors relating to time step, but a strong functional dependency is unusual. I observed in WRF-Fire, that the fire spread is dependent on the time step in that making the time step smaller reduces fire-spread speed and eventually converges the perimeter on stagnation (Supplemental Figure A.6, top). I believe this results from the time step acting as a secondary control on the number of re-initialization iterations on the level-set function. Indeed, decreasing the time step by half yields a nearly identical

stagnation phenomenon as doubling the number of re-initialization iterations per second

(Supplemental Figure A.6, bottom). This is the opposite result from what is described in the

literature for WRF-Fire (Muñoz-Esparza et al., 2018) where increasing the number of iterations

per second led to an increase in the fire-spread. My studies differ significantly in resolution,

forcing, topography and fuel properties so research is needed to understand why I observe a

different behavior here. What I can say is that the model appears to be sensitive to a derived

numerical parameter, the number of re-initialization iterations per second, and setting it

correctly could benefit simulation accuracy. This is controlled by both the

"FIRE_LSM_REINIT_ITER" parameter, which sets the number of iterations per time step, and the

"parent_time_step_ratio" which sets the number of seconds for the time step on the inner

domain. Dividing the two gives the number of iterations per second which I find to optimally be

around 3.33 in this work, when using 1 iteration per time step with a time step of 0.3 seconds

(Supplemental Figure A.6).

To get faster computational times for some sensitivities (Section 2.2.4), I needed to use

large time steps with spectrally smoothed topography and thus adjusted the re-initialization

iterations per second accordingly. In this study, I smoothed a 200 m inner domain with a 275 m

spectral smoothing pass, allowing us to double my time step from 0.3 s to 0.6 s, and double the

number of re-initialization iterations per time step from 1 to 2 to keep the simulations

reasonable.

A.3 Open Research

The official repository for WRF, which includes WRF-Fire configurations, is through GitHub (*WRF: The official repository for the Weather Research and Forecasting (WRF) model*, n.d.). The WRF Pre-processing System (WPS) is also available through GitHub (*WPS: The official repository for the WRF Preprocessing System (WPS)*, n.d.). The Open Wildland Fire Modeling E-community maintains a guide on WRF-Fire which was useful for this project (https://wiki.openwfm.org/wiki/How_to_run_WRF-Fire_with_real_data).

Input data for WRF-Fire is open source and described in-text. The High-Resolution Rapid Refresh (HRRR) model (Dowell et al., 2022) output is archived in grib2 format at the University of Utah https://home.chpc.utah.edu/~u0553130/Brian_Blaylock/hrrr_FAQ.html, (B. Blaylock and Horel 2021; B. K. Blaylock, Horel, and Liston 2017). High-resolution topography and fuel categories can be found on the LANDFIRE data distribution site (Department of Interior, Geological Survey, and U.S. Department of Agriculture., 2016; Ryan & Opperman, 2013). The fuel moisture content maps are archived by the National Center for Atmospheric Research (NCAR) and Geoscience Data Exchange (GDEX) (Kosovic et al., 2019). Containment data and fire perimeters can be found at the National Interagency Fire Center (NIFC) Open Data Site (Wildland Fire Interagency Data Service (WFIGS), National Interagency Fire Center (NIFC), National Wildfire Coordinating Group (NWCG) Geospatial Subcommittee, 2021). Perimeters as well as intense heat and scattered heat partitions can be found on the NIFC Public Access Folder in Incident Specific Data (https://ftp.wildfire.gov/). RAWS data can be accessed through an open access online portal (Western Regional Climate Center, n.d.).

To insert a fire perimeter and remove the fuel in the non-intense heat regions on the wrfinput_d02 file, I used the following open source python libraries:

- netCDF4.Dataset is used to read and overwrite variables in wrfinput_d02. I read in the variable LFN_HIST and overwrite it with the imprinted perimeter,
- json is used to read the polygon geometry coordinates in the perimeter file (in geojson format),
- matplotlib.path.Path and matplotlib.path.contains_points are used to mask points in/out of the fire perimeter,
- scipy.ndimage.distance_transform_edt is used to assign a value of 1 to points where the perimeter mask is True, and calculate the exact Euclidean distance between True points (inside of perimeter) and their closest False point (perimeter boundary). The resulting distances are reversed (1-x), yielding a new LFN_HIST field where negative values indicate points inside the perimeter,
- shapely.geometry.polygon.contains is used to check if grid cells are within the intense heat areas for fuel removal.

The calculation of GOES-17 grid cell centers followed this tutorial on MakerPortal (https://makersportal.com/blog/2018/11/25/goes-r-satellite-latitude-and-longitude-grid-projection-algorithm). GOES-17 Wildfire Automated Biomass Burning Algorithm (WFABBA) FRP product is generated by the Cooperative Institute for Meteorological Satellite Studies (CIMSS) at the University of Wisconsin, Madison. GOES-17 fire detections and FRP data for this study, as well as DC-8 measurements are archived by NASA/LARC/SD/ASDC

(NASA/LARC/SD/ASDC, 2020).

The following open source python libraries were used for data analysis in this study:

- salem.open_mf_wrf_dataset was used to open multiple WRF output files in a single xarray.dataset,

- pyproj.transform was used with cartopy contours of FIRE_AREA (WRF-Fire output) to project shapely.geometry.polygon fire perimeters (Equal Area Cylindrical) for burned area calculations,

- geopandas was used to open and project NIROPS shape files (Equal Area Cylindrical) for burned area calculations,

- matplotlib.path.Path and matplotlib.path.contains_points were used to check if WRF-Fire grid cells were within GOES-17's grid cells

- scipy.signal.correlate was used to create the cross correlation matrix from which offset in FRP temporal cycle was calculated,

Matplotlib v3.1.3 (Caswell et al., 2020) and Cartopy 0.17.0 (Elson et al., 2022) were used to create the 2-dimensional figures in this dissertation. The Visualization and Analysis Platform for Ocean, Atmosphere, and Solar Researchers (VAPOR) was used to make 3-dimensional contour plots of Q-Criterion (Li et al., 2019).

A sample case has been made available for Chapter 2 with Zenodo (Turney, 2023). This contains much of the inputs and outputs from the *contain-FMC* simulation ignited just before August 6th. Found there is the information needed to run WRF-Fire including the configurations files *namelist.input* and *namelist.fire.*
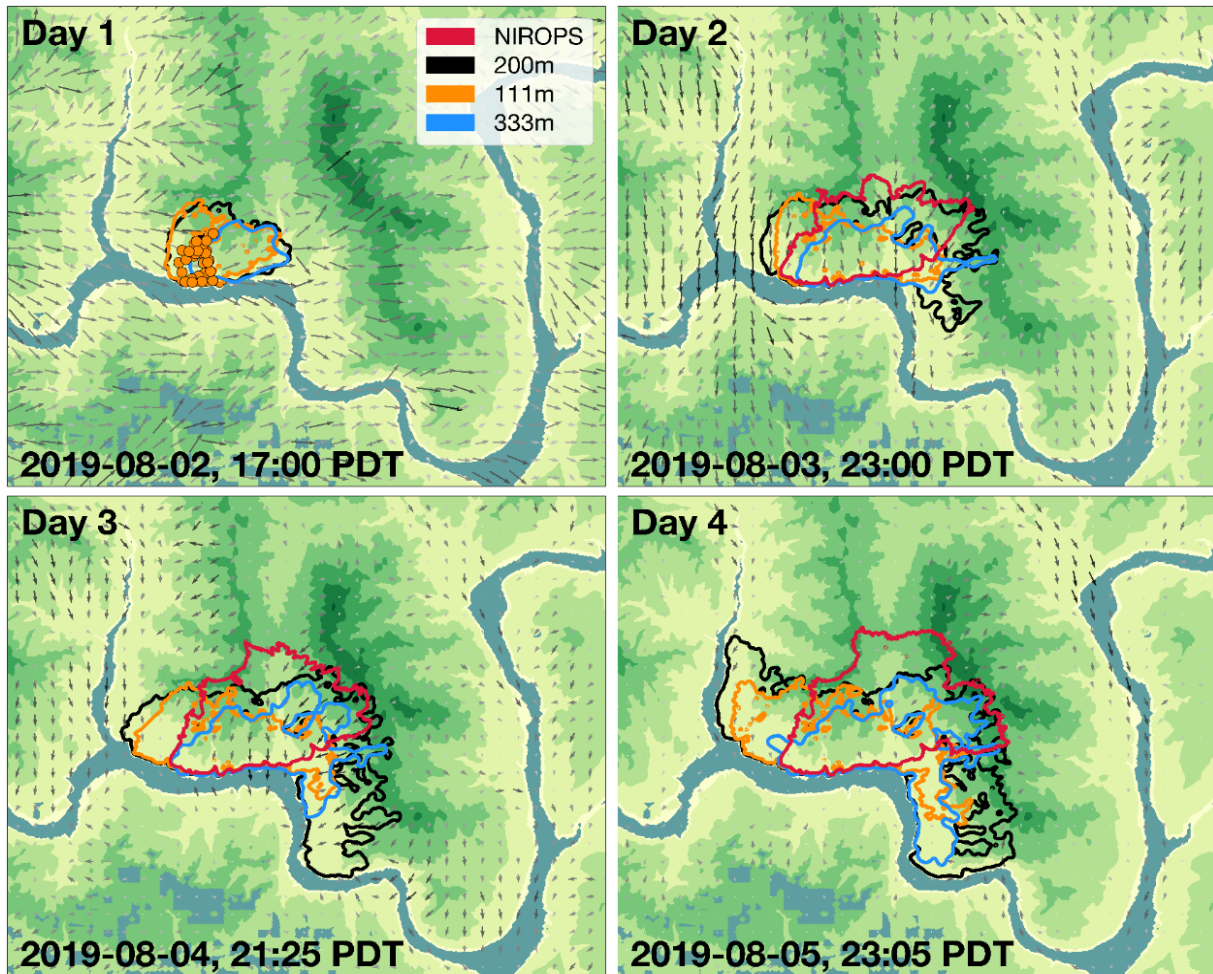
Supplemental Figure A.1. Fire perimeters for point ignition simulation showing the sensitivity of WRF-Fire to different horizontal resolutions. 200m is chosen as the base for Chapter 2.
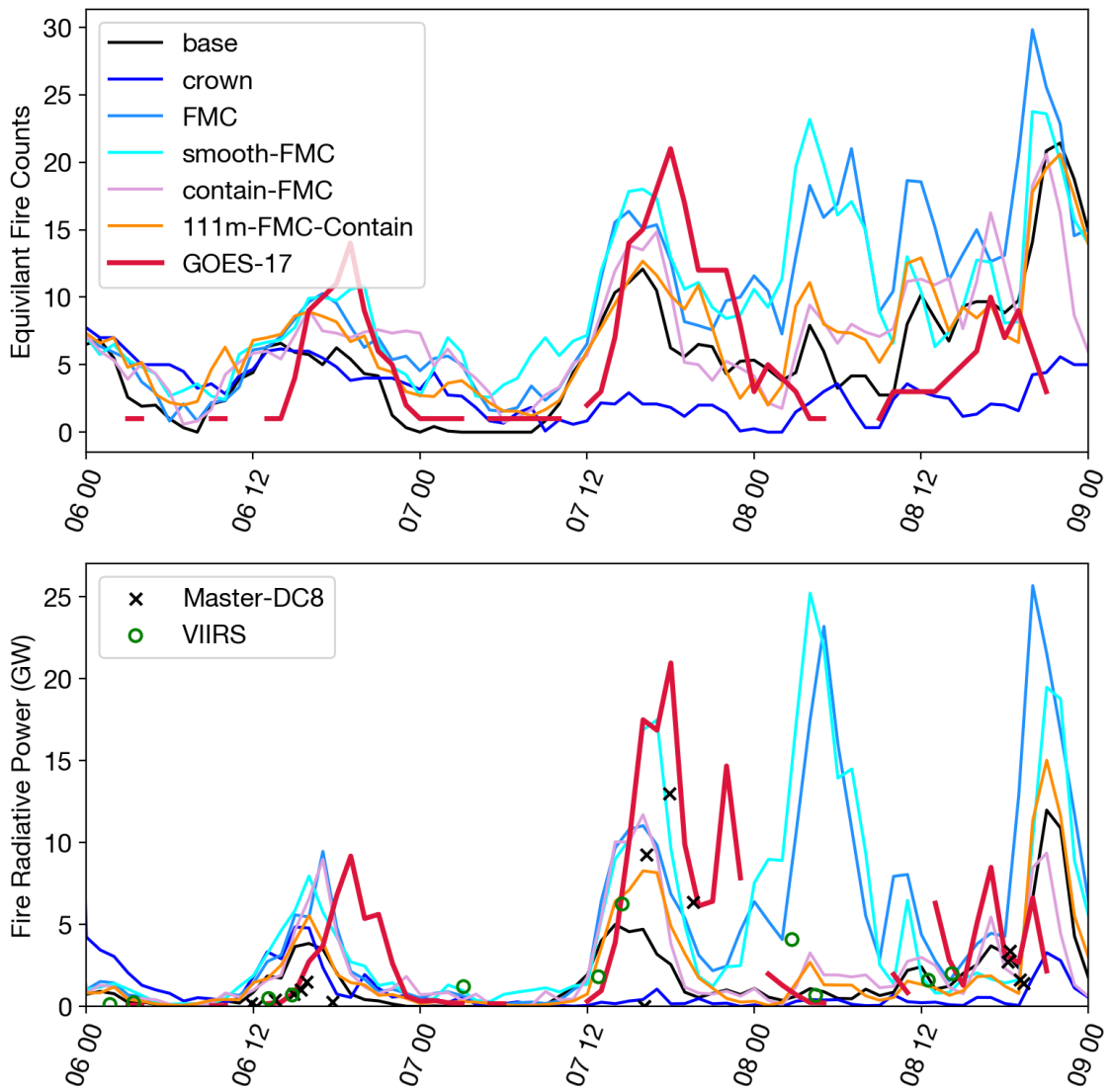
Supplemental Figure A.2. Fire Counts and FRP for fire ignited just before 8/06. See Figure 2.8 for a

breakdown.
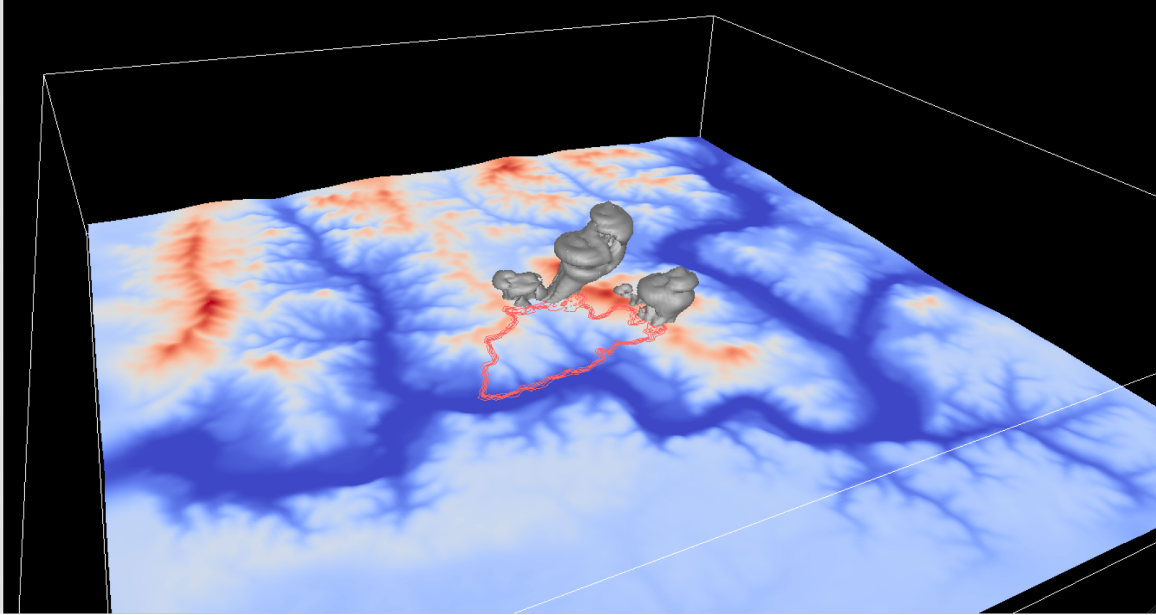
Supplemental Figure A.3. VAPOR snapshot five minutes after ignition of an iso-contour of Q-criterion

(vorticity minus shear), for a fuel moisture simulation starting on August 6th, 2019. Fire perimeter is a

red contour and altitude is shown in blue/red, although the height scale is not visually accurate. Tilted

hairpin vorticity packets lifted by convection and aligned vertically can be seen.
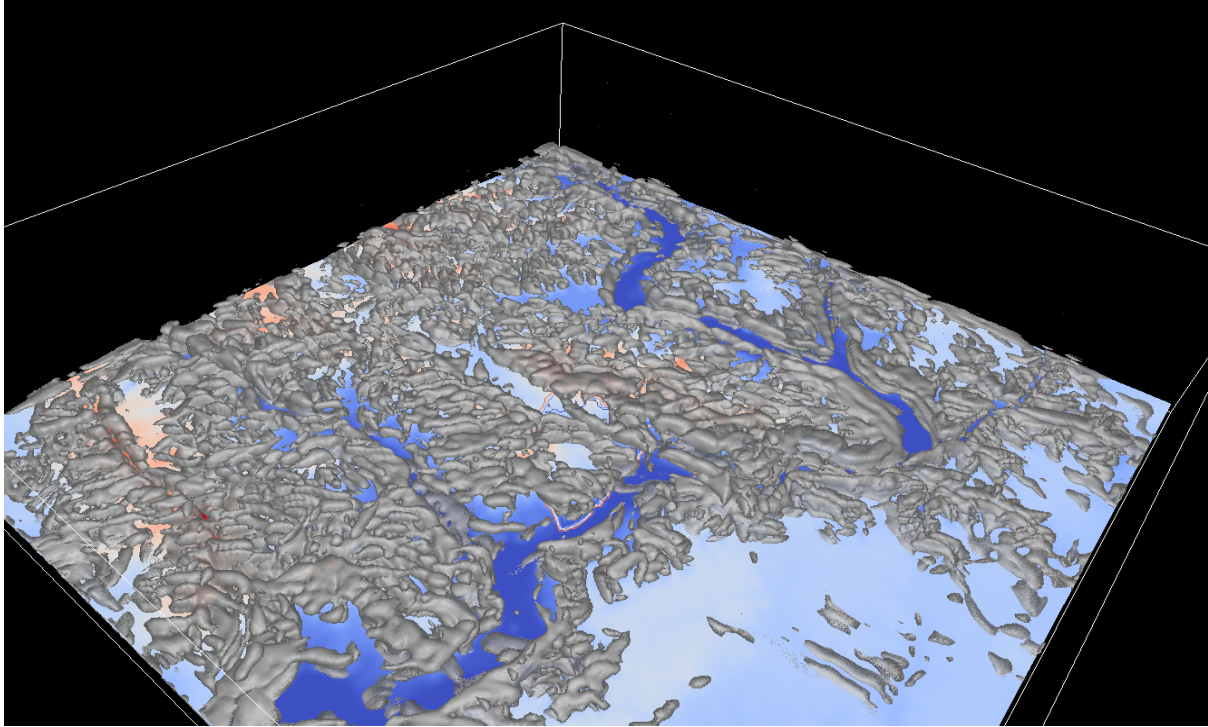
Supplemental Figure A.4. VAPOR snapshot at 10 AM PDT on August 6th showing background turbulence before intense fire activity. Plotted is an Iso-contour of Q-criterion (vorticity minus shear), for contain-FMC simulation. Fire perimeter is a red contour and altitude is shown in blue/red, although the height scale is not visually accurate. A field of hairpins organized in trains can be seen. Mostly the bursting heads of the vortices are visible with a few well defined counter-rotating legs rendered as well.
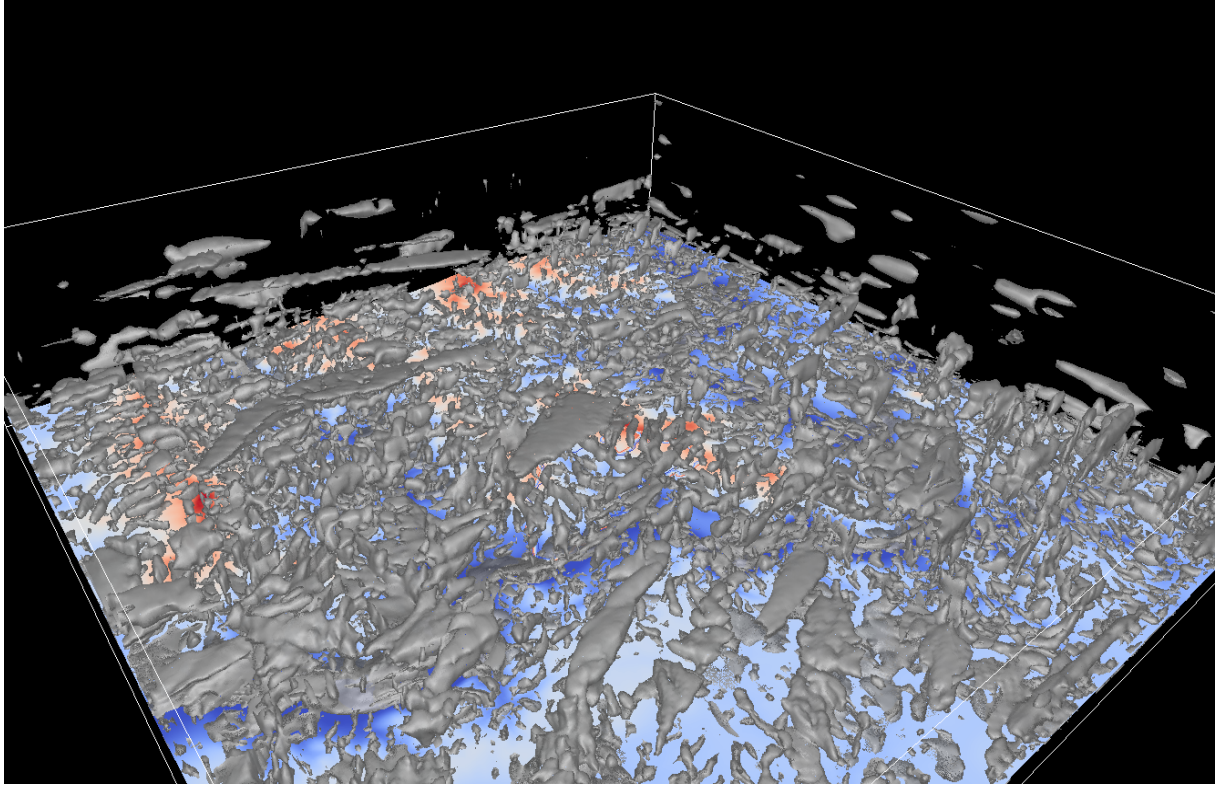
Supplemental Figure A.5. VAPOR snapshot at 10 AM PDT on August 6th showing background turbulence before intense fire activity. Plotted is an iso-contour of Q-criterion (vorticity minus shear), for contain-FMC simulation. Fire perimeter is a red contour and altitude is shown in blue/red, although the height scale is not visually accurate. Turbulence can be seen through much of the domain.
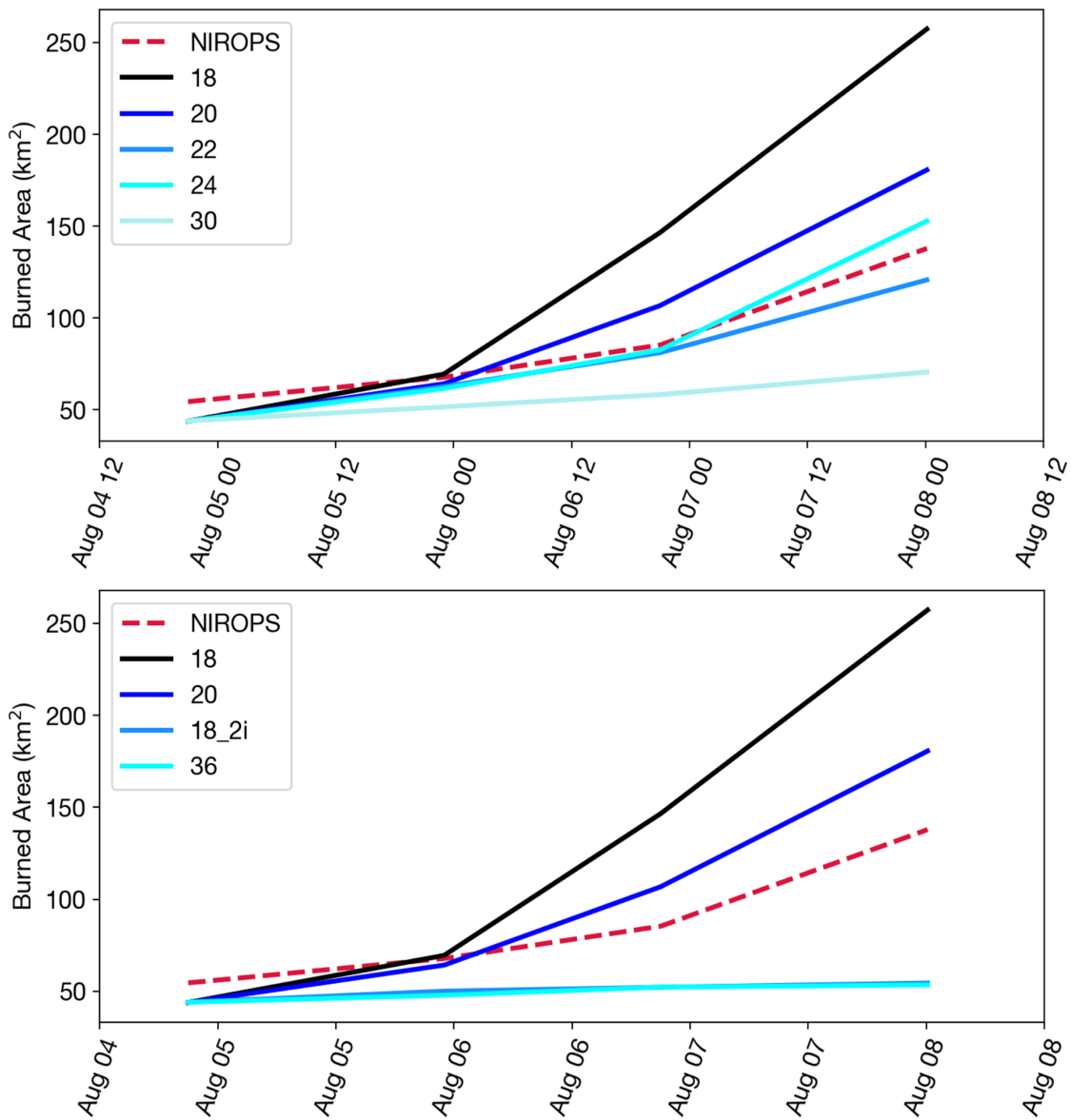
Supplemental Figure A.6. Top: For a simulation ignited on August 5th I show the model sensitivity to the parameter "parent_time_step_ratio" which sets the denominator for the time step for the fire and weather models. The numerator is 6 seconds thus the ratios 18, 20, 22, 24, and 30 represent time steps of 0.33, 0.30, 0.27, 0.25, and 0.20 respectively. Simulations are FMC configurations and differ only in time step. Bottom: Similar set of simulations to top but "18_2i" notates a ratio of 18 but with 2 iterations of a reinitialization scheme for the level set method.
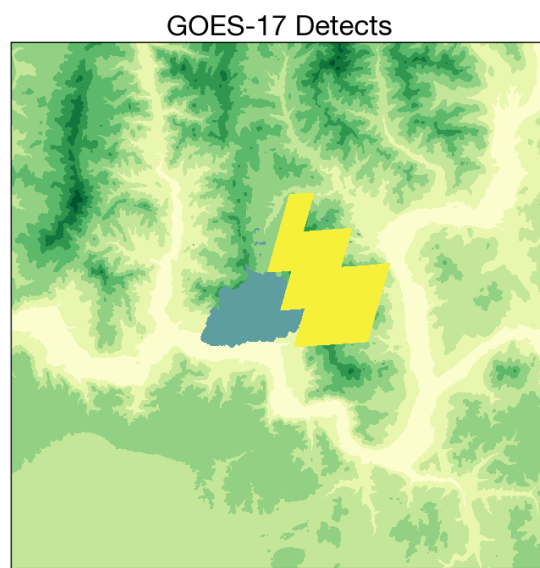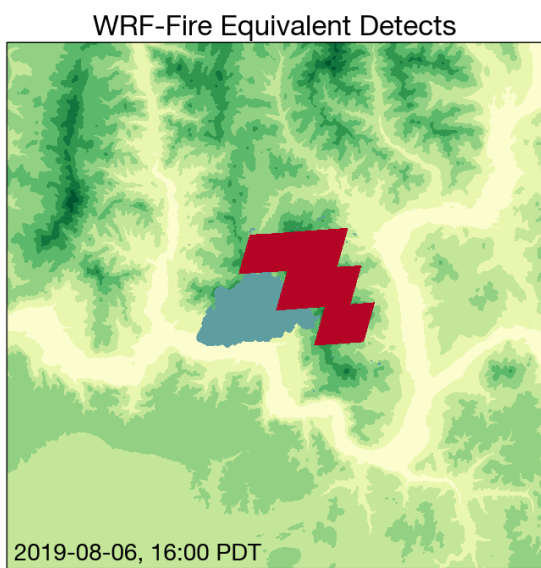
Supplemental Figure A.7. Example of WRF-Fire re-gridding output to the GOES-17 grid at the peak of the

Williams Flats fire at 16:00 PDT on August 6th. Blue/Gray color represents burnt out interior.
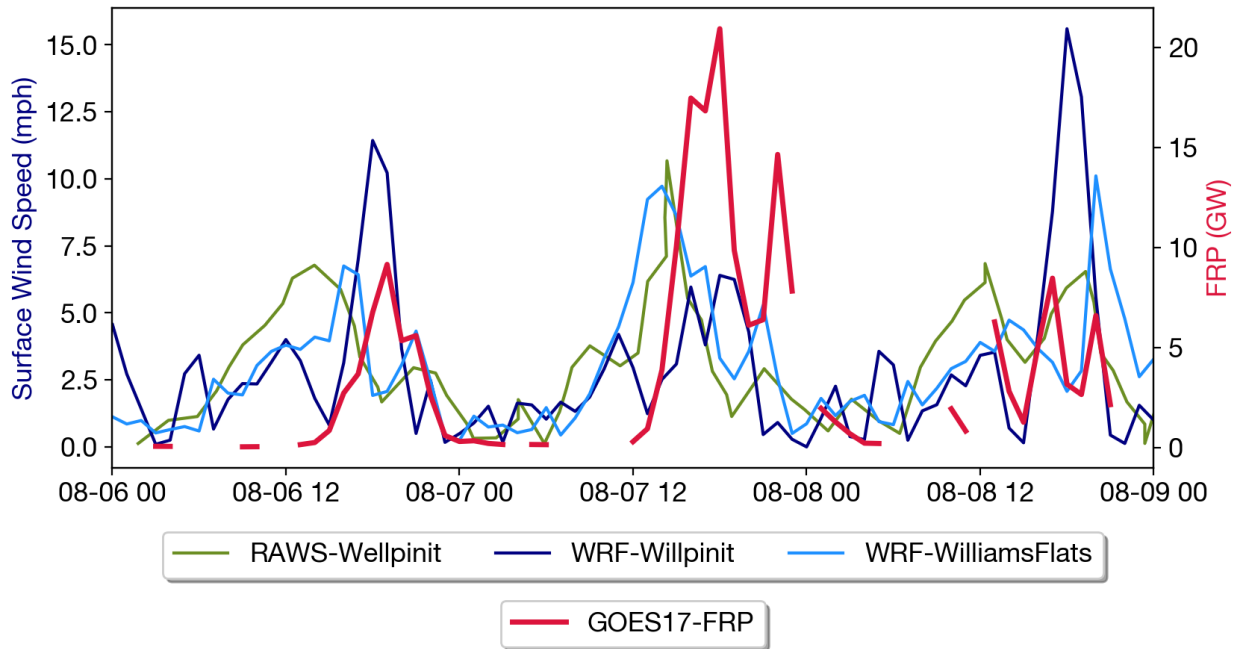
Supplemental Figure A.8. Surface wind speeds and FRP curves comparison. Red colors are FRP, blue colors are WRF simulated wind speeds, and green colors are RAWS detected wind speeds. Note that all observations and simulations of wind speed lead observations of FRP.
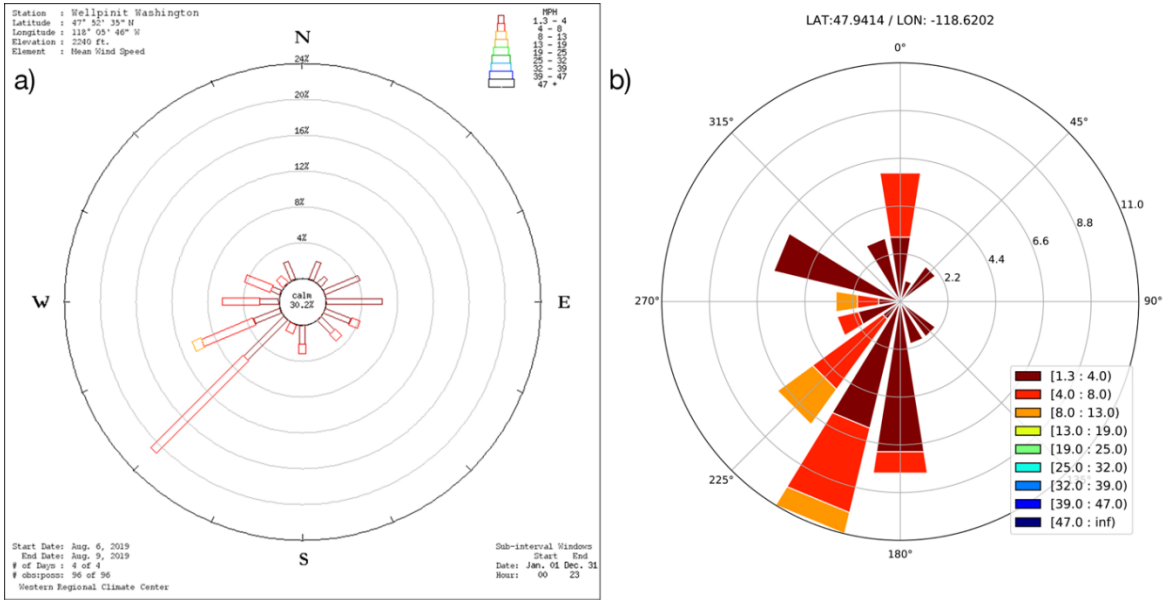
Supplemental Figure A.9. Wind Roses of mean wind speed from a) RAWS Wellpinit station and b) nearby

Williams Flats Fire from August 6th through 9th from the contain-FMC simulation ignited on August 6th.

Note the slight southerly bias in WRF for periods of high mean wind speed.
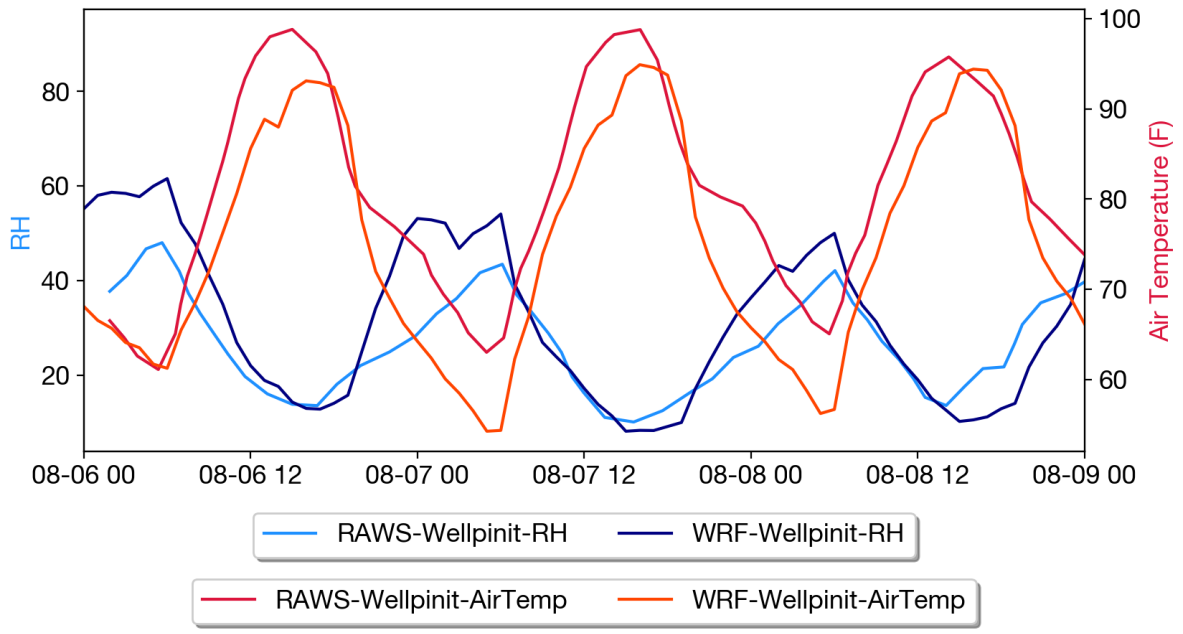
Supplemental Figure A.10. Blue colors show surface relative humidity between WRF and RAWS, red

colors show air temperature.
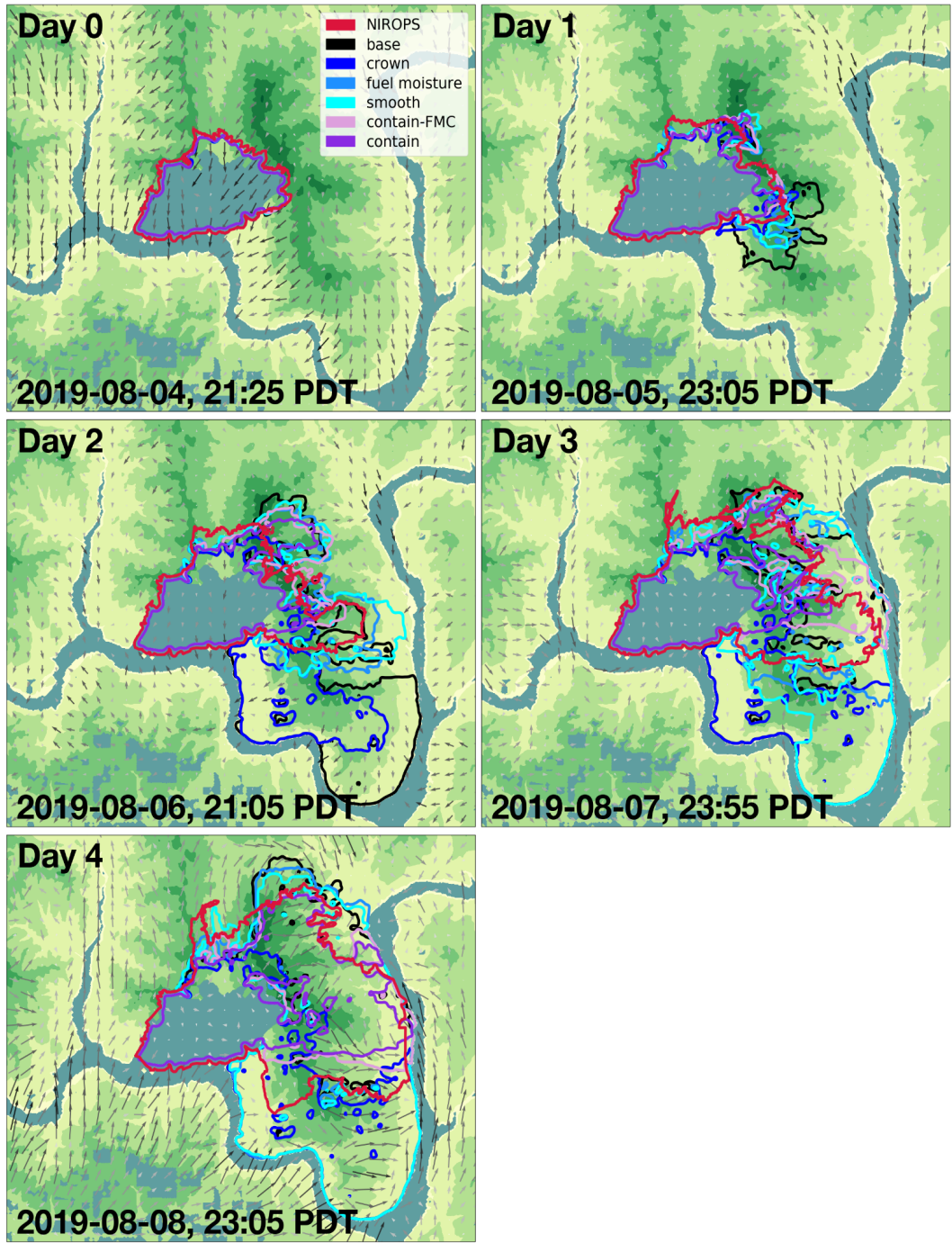
Supplemental Figure A.11. Fire perimeters for simulations ignited on August 5th, 2019. See Figures 2.2

and 2.3 for a breakdown of simulations and no-fuel sections. Figure is included as an example of

simulation data from an ignition day not shown in the main text.
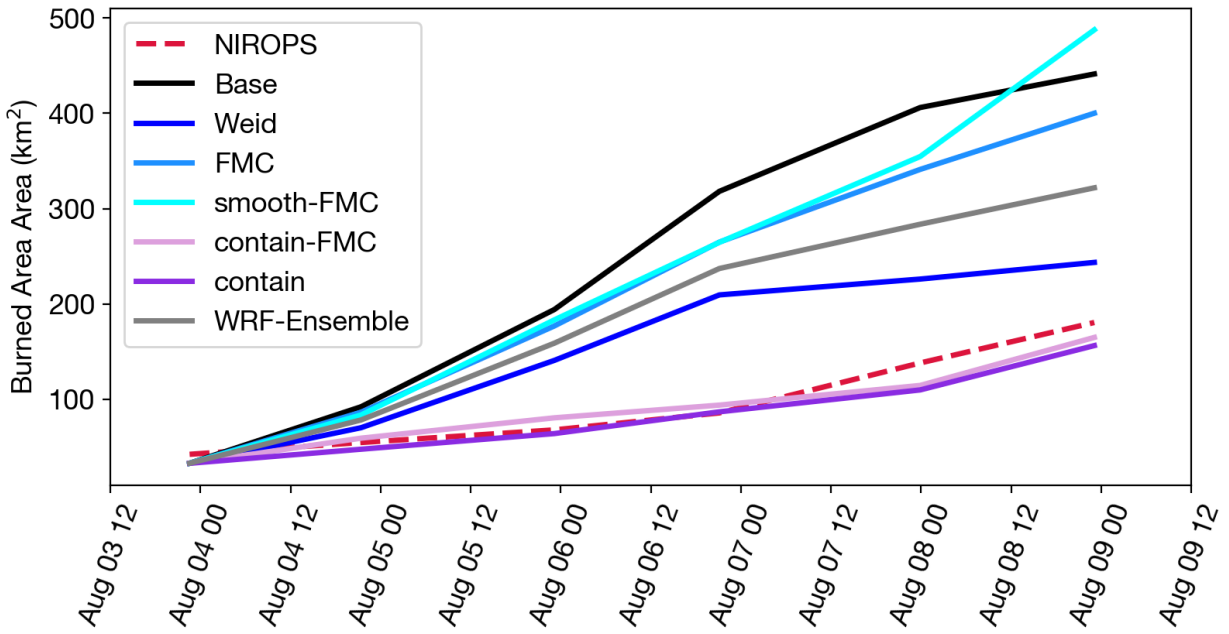
Supplemental Figure A.12. Burned area time series for simulations ignited on August 4th, 2019. Figure is

included as an example of simulation data from an ignition day not shown in the main text.
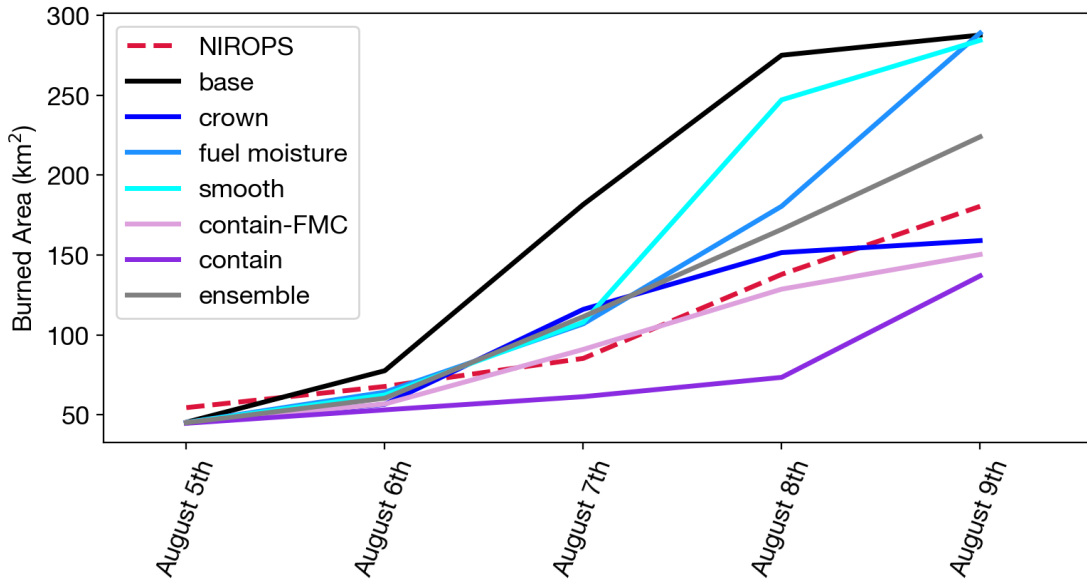
Supplemental Figure A.13. Burned area time series for simulations ignited just before August 5th, 2019.

Figure is included as an example of simulation data from an ignition day not shown in the main text.
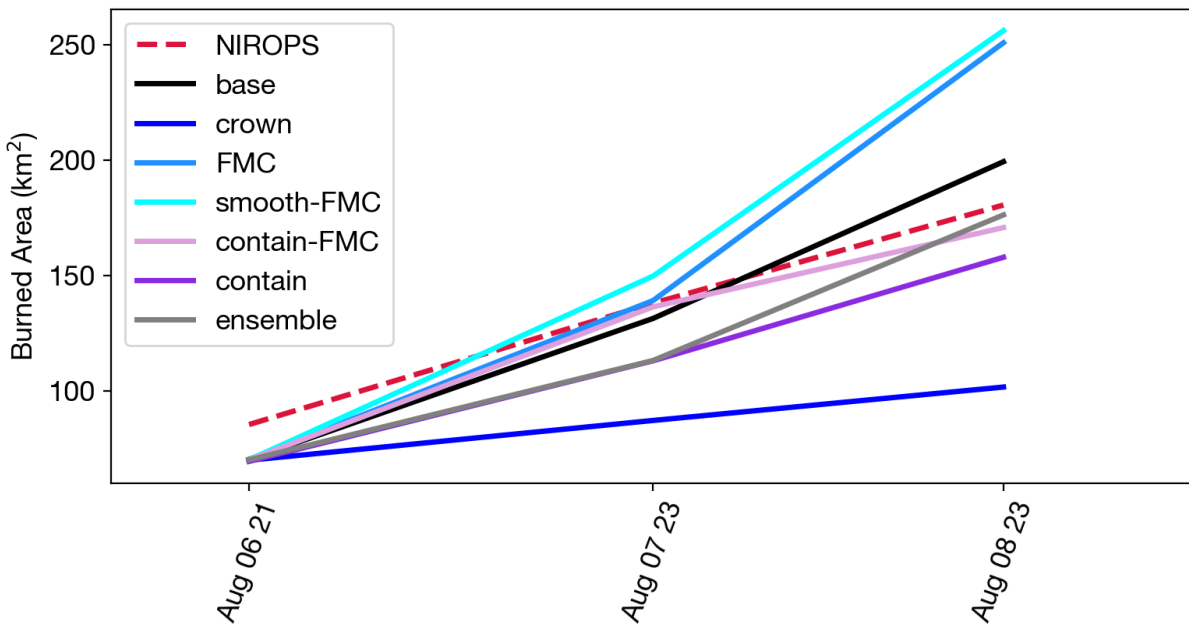
Supplemental Figure A.14. Burned area time series for simulations ignited just before August 7th, 2019.

Figure is included as an example of simulation data from an ignition day not shown in the main text.

Supplemental Figure A.15. FRP for fire ignited just before August 7th, 2019. See Figure 2.8 for a

breakdown. Figure is included as an example of simulation data from an ignition day not shown in the

main text.

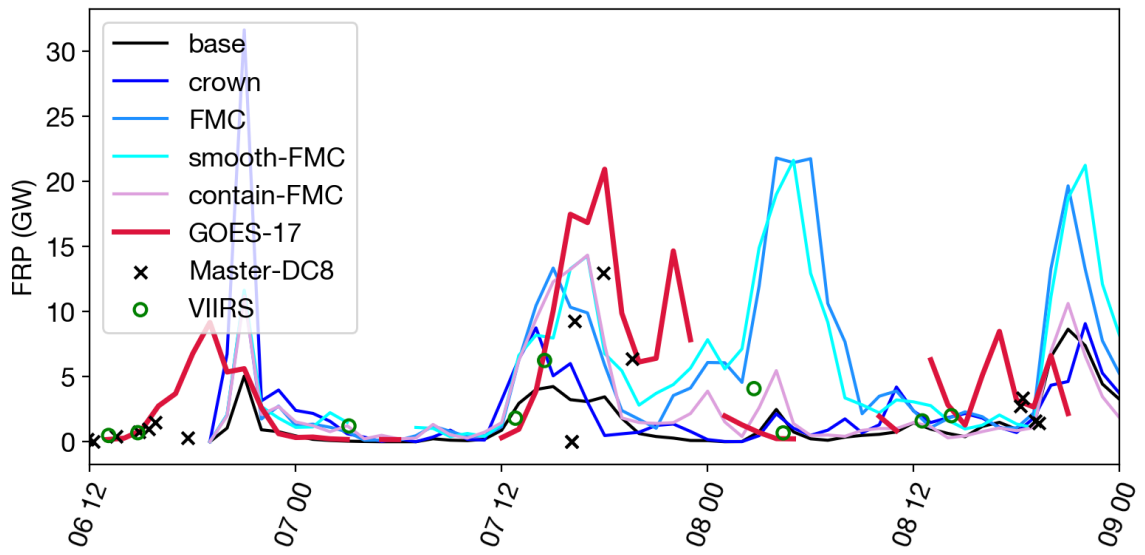|	Fuel Densities (kg/m²)			
	13-Category	13-Category FINN	41-Category	41-Category FINN
1: Short grass (1 ft)	0.17	0.98		
2: Timber (grass and understory)	0.9	5.7		
3: Tall grass (2.5 ft)	0.67	0.98		
4: Chaparral (6 ft)	3.59	5.7		
5: Brush (2 ft)	0.74	5.7		
6: Dormant brush, hardwood slash	1.34	5.7		
7: Southern rough	1.09	0.98		
8: Closed timber litter	1.12	10.49		
9: Hardwood litter	0.78	10.49		
10: Timber (litter + understory)	2.69	10.49		
11: Light logging slash	2.58	10.49		
12: Medium logging slash	7.75	10.49		
13: Heavy logging slash	13.02	10.49		
14: no fuel	0.0	0.0	0.0	0.0
15: Short, Sparse Dry Climate Grass (Dynamic) [GR1 (101)]			0.02	0.25
16: Low Load, Dry Climate Grass (Dynamic) GR2 (102)			0.02	0.25
17: Low Load, Very Coarse, Humid Climate Grass (Dynamic) [GR3 (103)]			0.02	0.25
18: Moderate Load, Dry Climate Grass (Dynamic) [GR4 (104)]			0.06	0.62
19: Low Load, Humid Climate Grass (Dynamic) [GR5 (105)]			0.09	0.99
20: Moderate Load, Humid Climate Grass (Dynamic) [GR6 (106)]			0.02	0.25
21: High Load, Dry Climate Grass (Dynamic) [GR7 (107)]			0.22	2.47
22: High Load, Very Coarse, Humid Climate Grass (Dynamic) [GR8 (108)]			0.11	1.24
23: Very High Load, Humid Climate Grass (Dynamic) [GR9 (109)]			0.22	2.47
24: Low Load, Dry Climate Grass-Shrub (Dynamic) [GS1 (121)]			0.04	0.66
25: Moderate Load, Dry Climate Grass-Shrub (Dynamic) [GS2 (122)]			0.11	1.66
26: Moderate Load, Humid Climate Grass-Shrub (Dynamic) [GS3 (123)]			0.07	1.0
27: High Load, Humid Climate Grass-Shrub (Dynamic) [GS4 (124)]			0.43	6.3
28: Low Load Dry Climate Shrub (Dynamic) [SH1 (141)]			0.06	0.83
29: Moderate Load Dry Climate Shrub [SH2 (142)]			0.3	4.48
30: Moderate Load, Humid Climate Shrub [SH3 (143)]			0.1	1.49
31: Low Load, Humid Climate Timber-Shrub [SH4 (144)]			0.19	2.82
32: High Load, Dry Climate Shrub [SH5 (145)]			0.81	11.95
33: Low Load, Humid Climate Shrub [SH6 (146)]			0.65	9.62
34: Very High Load, Dry Climate Shrub [SH7 (147)]			0.78	11.61
35: High Load, Humid Climate Shrub [SH8 (148)]			0.46	6.8
36: Very High Load, Humid Climate Shrub (Dynamic) [SH9 (149)]			1.01	14.93
37: Low Load Dry Climate Timber-Grass-Shrub (Dynamic) [TU1 (161)]			0.04	0.8
38: Moderate Load, Humid Climate Timber-Shrub [TU2 (162)]			0.21	3.8
39: Moderate Load, Humid Climate Timber-Grass-Shrub (Dynamic) [TU3 (163)]			0.25	4.4
40: Dwarf Conifer With Understory [TU4 (164)]			1.01	18.01
41: Very High Load, Dry Climate Timber-Shrub [TU5 (165)]			0.9	16.0
42: Low Load Compact Conifer Litter [TL1 (181)]			0.22	4.0
43: Low Load Broadleaf Litter [TL2 (182)]			0.31	5.6
44: Moderate Load Conifer Litter [TL3 (183)]			0.11	2.0
45: Small downed logs [TL4 (184)]			0.11	2.0
46: High Load Conifer Litter [TL5 (185)]			0.26	4.6
47: Moderate Load Broadleaf Litter [TL6 (186)]			0.54	9.6
48: Large Downed Logs [TL7 (187)]			0.07	1.2
49: Long-Needle Litter [TL8 (188)]			1.3	23.21
50: Very High Load Broadleaf Litter [TL9 (189)]			1.49	26.61
51: Low Load Activity Fuel [SB1 (201)]			0.34	6.0
52: Moderate Load Activity Fuel or Low Load Blowdown [SB2 (202)]			1.01	18.01
53: High Load Activity Fuel or Moderate Load Blowdown [SB3 (203)]			1.23	22.01
54: High Load Blowdown [SB4 (204)]			1.18	21.01

Supplemental Table A.1. Fuel Density Adjustments. Fuel densities for 13-category (Anderson 1981), and

41-category (Scott 2005), as well as the scaled fuel densities by FINN categories (Wiedinmyer et al.

2011).

Bibliography

Abatzoglou, J. T., & Williams, A. P. (2016). Impact of anthropogenic climate change on wildfire across western US forests. *Proceedings of the National Academy of Sciences of the United States of America*, *113*(42), 11770–11775.

Ahmadov, R., Grell, G., James, E., Csiszar, I., Tsidulko, M., Pierce, B., et al. (2017). Using VIIRS fire radiative power data to simulate biomass burning emissions, plume rise and smoke transport in a real-time air quality modeling system. In *2017 IEEE International Geoscience and Remote Sensing Symposium (IGARSS)* (pp. 2806–2808). ieeexplore.ieee.org.

Anderson, D. H., Catchpole, E. A., De Mestre, N. J., & Parkes, T. (1982). Modelling the spread of grass fires. *ANZIAM Journal*, *23*(4), 451–466.

Anderson, H. E. (1981). *Aids to Determining Fuel Models for Estimating Fire Behavior*. U.S. Department of Agriculture, Forest Service, Intermountain Forest and Range Experiment Station.

Andrews, P. L. (2014). Current status and future needs of the BehavePlus Fire Modeling System. *International Journal of Wildland Fire*, *23*(1), 21.

Badlan, R. L., Sharples, J. J., Evans, J. P., & McRae, R. H. D. (2021a). Factors influencing the development of violent pyroconvection. Part I: fire size and stability. *International Journal of Wildland Fire*, *30*(7), 484–497.

Badlan, R. L., Sharples, J. J., Evans, J. P., & McRae, R. H. D. (2021b). Factors influencing the development of violent pyroconvection. Part II: fire geometry and intensity. *International Journal of Wildland Fire*, *30*(7), 498–512.

Bakhshaii, A., & Johnson, E. A. (2019). A review of a new generation of wildfire–atmosphere modeling. *Canadian Journal of Forest Research. Journal Canadien de La Recherche Forestiere*, *49*(6), 565–574.

Balch, J. K., Abatzoglou, J. T., Joseph, M. B., Koontz, M. J., Mahood, A. L., McGlinchy, J., et al. (2022). Warming weakens the night-time barrier to global fire. *Nature*, *602*(7897), 442–448.

Balshi, M. S., Mcguire, A. D., Duffy, P., Flannigan, M., Kicklighter, D. W., & Melillo, J. (2009). Vulnerability of carbon storage in North American boreal forests to wildfires during the 21st century. *Global Change Biology*, *15*(6), 1491–1510.

Benjamin, S. G., Weygandt, S. S., Brown, J. M., Hu, M., Alexander, C. R., Smirnova, T. G., et al. (2016). A North American Hourly Assimilation and Model Forecast Cycle: The Rapid Refresh. *Monthly Weather Review*, *144*(4), 1669–1694.

Berman, M., Ye, X., Thapa, L., Peterson, D., Hyer, E., Soja, A., et al. (2021). Quantifying Burned Area of Wildfires from Satellite Active Fire Detections (Vol. 2021). AGU Fall Meeting. Retrieved from https://ui.adsabs.harvard.edu/abs/2021AGUFM.U55A..08B

Black, C., Tesfaigzi, Y., Bassein, J. A., & Miller, L. A. (2017). Wildfire smoke exposure and human health: Significant gaps in research for a growing public health issue. *Environmental Toxicology and Pharmacology*, *55*, 186–195.

Blaylock, Brian, and John Horel. 2021. Metadata for the High Resolution Rapid Refresh Model Archives [Dataset]. April 15, 2021. https://dx.doi.org/10.7278/S5JQ0Z5B.

Blaylock, Brian K., John D. Horel, and Samuel T. Liston. 2017. "Cloud Archiving and Data Mining of High-Resolution Rapid Refresh Forecast Model Output [Data]." *Computers & Geosciences* 109 (December): 43–50.

Bright, B. C., Hudak, A. T., Meddens, A. J. H., Hawbaker, T. J., Briggs, J. S., & Kennedy, R. E. (2017). Prediction of Forest Canopy and Surface Fuels from Lidar and Satellite Time Series Data in a Bark Beetle-Affected Forest. *Forests, Trees and Livelihoods*, *8*(9), 322.

Byram. (1959). Combustion of forest fuels. *Forest Fire: Control and Use*. Retrieved from https://ci.nii.ac.jp/naid/10029316165/

Caswell, T. A., Droettboom, M., Lee, A., Hunter, J., Firing, E., Stansby, D., et al. (2020). *matplotlib/matplotlib v3.1.3*. [Software] https://doi.org/10.5281/zenodo.3633844

Chopp, D. L. (1991). *Computing minimal surfaces via level set curvature flow*. (J. Sethian, Ed.). University of California, Berkeley, Ann Arbor, United States. Retrieved from https://www.proquest.com/dissertations-theses/computing-minimal-surfaces-via-level-set/docview/303917093/se-2

Clark, T. L., Coen, J., & Latham, D. (2004). Description of a coupled atmosphere–fire model. *International Journal of Wildland Fire*, *13*(1), 49–63.

Coen, J. L. (2005). Simulation of the Big Elk Fire using coupled atmosphere–fire modeling. *International Journal of Wildland Fire*, *14*(1), 49–59.

Coen, J. L., Cameron, M., Michalakes, J., Patton, E. G., Riggan, P. J., & Yedinak, K. M. (2013). WRF-Fire: Coupled Weather–Wildland Fire Modeling with the Weather Research and Forecasting Model. *Journal of Applied Meteorology and Climatology*, *52*(1), 16–38.

Couto, F. T., Filippi, J.-B., Baggio, R., Campos, C., & Salgado, R. (2024). Triggering Pyro-Convection in a High-Resolution Coupled Fire–Atmosphere Simulation. *Fire*, *7*(3), 92.

Dahl, N., Xue, H., Hu, X., & Xue, M. (2015). Coupled fire–atmosphere modeling of wildland fire spread using DEVS-FIRE and ARPS. *Natural Hazards*, *77*(2), 1013–1035.

Deardorff, J. W. (1980). Stratocumulus-capped mixed layers derived from a three-dimensional model. *Boundary - Layer Meteorology*, *18*(4), 495–527.

De Moura, C. A., & Kubrusly, C. S. (2013). *The Courant–Friedrichs–Lewy (CFL) Condition*. Birkhäuser Boston.

Department of Interior, Geological Survey, and U.S. Department of Agriculture. (2016). LANDFIRE: LANDFIRE 13 Fire Behavior Fuel Models-Anderson, LANDFIRE 40 Fire Behavior Fuel Models-Scott/Burgan, Elevation (2020, Last Update) [Dataset]. *[Online] Available: Http://landfire.cr.usgs.gov/viewer/*.

Dobrinkova, N., & Dobrinkov, G. (2014). FARSITE and WRF-Fire Models, Pros and Cons for Bulgarian Cases. In *Large-Scale Scientific Computing* (pp. 382–389). Springer Berlin Heidelberg.

Donato, D. C., Harvey, B. J., Romme, W. H., Simard, M., & Turner, M. G. (2013). Bark beetle effects on fuel profiles across a range of stand structures in Douglas-fir forests of Greater Yellowstone. *Ecological Applications: A Publication of the Ecological Society of America*, *23*(1), 3–20.

Dowell, D. C., Alexander, C. R., James, E. P., Weygandt, S. S., Benjamin, S. G., Manikin, G. S., et al. (2022). The High-Resolution Rapid Refresh (HRRR): An Hourly Updating Convection-Allowing Forecast Model. Part I: Motivation and System Description. *Weather and*

Forecasting, *37*(8), 1371–1395.

Drury, Stacy A., Narasimhan Sim Larkin, Tara T. Strand, Shihming Huang, Scott J. Strenfel, Erin M. Banwell, Theresa E. O'Brien, and Sean M. Raffuse. 2014. "Intercomparison of Fire Size, Fuel Loading, Fuel Consumption, and Smoke Emissions Estimates on the 2006 Tripod Fire, Washington, USA." *Fire Ecology* 10 (1): 56–83.

Elson, P., de Andrade, E. S., Lucas, G., May, R., Hattersley, R., Campbell, E., et al. (2022). *SciTools/cartopy: v0.21.1*. [Software] https://doi.org/10.5281/zenodo.7430317

Finney, M. A. (1998). *FARSITE, Fire Area Simulator--model Development and Evaluation*. U.S. Department of Agriculture, Forest Service, Rocky Mountain Research Station.

Frankman, D., Webb, B. W., Butler, B. W., Jimenez, D., Forthofer, J. M., Sopko, P., et al. (2012). Measurements of convective and radiative heating in wildland fires. *International Journal of Wildland Fire*, *22*(2), 157–167.

Frediani, M., Juliano, T. W., DeCastro, A., Kosovic, B., & Knievel, J. (2021, April 19). *A fire-spotting parameterization coupled with the WRF-fire model*. *Earth and Space Science Open Archive*. Earth and Space Science Open Archive. https://doi.org/10.1002/essoar.10506771.1

Freeborn, P. H., Wooster, M. J., Hao, W. M., Ryan, C. A., Nordgren, B. L., Baker, S. P., & Ichoku, C. (2008). Relationships between energy release, fuel mass loss, and trace gas and aerosol emissions during laboratory biomass fires. *Journal of Geophysical Research*, *113*(D1). https://doi.org/10.1029/2007jd008679

Graff, C. A., Coffield, S. R., Chen, Y., Foufoula-Georgiou, E., Randerson, J. T., & Smyth, P. (2020). Forecasting Daily Wildfire Activity Using Poisson Regression. *IEEE Transactions on*

Geoscience and Remote Sensing: A Publication of the IEEE Geoscience and Remote Sensing Society, *58*(7), 4837–4851.

Halofsky, J. E., Peterson, D. L., & Harvey, B. J. (2020). Changing wildfire, changing forests: the effects of climate change on fire regimes and vegetation in the Pacific Northwest, USA. *Fire Ecology*, *16*(1), 4.

Hiers, J. K., Stauhammer, C. L., O'Brien, J. J., Gholz, H. L., Martin, T. A., Hom, J., & Starr, G. (2019). Fine dead fuel moisture shows complex lagged responses to environmental conditions in a saw palmetto (Serenoa repens) flatwoods. *Agricultural and Forest Meteorology*, *266-267*, 20–28.

Hoffman, C. M., Sieg, C. H., McMillin, J. D., & Fulé, P. Z. (2011). Fuel loadings 5 years after a bark beetle outbreak in south-western USA ponderosa pine forests. *International Journal of Wildland Fire*, *21*(3), 306–312.

Jimenez, P. A., Brown, B., Kosovic, B., Cowie, J., Munoz-Esparza, D., Anderson, A., et al. (2018). Description and evaluation of the Colorado Fire Prediction system (CO-FPS) (Vol. 2018, p. EP31B–03). ui.adsabs.harvard.edu.

Johnson, E. A., Miyanishi, K., & Bridge, S. R. J. (2001). Wildfire Regime in the Boreal Forest and the Idea of Suppression and Fuel Buildup. *Conservation Biology: The Journal of the Society for Conservation Biology*, *15*(6), 1554–1557.

Johnston, J. M., Wooster, M. J., Paugam, R., Wang, X., Lynham, T. J., & Johnston, L. M. (2017). Direct estimation of Byram's fire intensity from infrared remote sensing imagery. *International Journal of Wildland Fire*, *26*(8), 668–684.

Juliano, T. W., Kosović, B., Jiménez, P. A., Eghdami, M., Haupt, S. E., & Martilli, A. (2022). "Gray

Zone" Simulations Using a Three-Dimensional Planetary Boundary Layer Parameterization

in the Weather Research and Forecasting Model. *Monthly Weather Review*, *150*(7), 1585–

1619.

Katich, J. M., Apel, E. C., Bourgeois, I., Brock, C. A., Bui, T. P., Campuzano-Jost, P., et al. (2023).

Pyrocumulonimbus affect average stratospheric aerosol composition. *Science*, *379*(6634),

815–820.

Keifer, M., van Wagtendonk, J. W., & Buhler, M. (2006). Long-term surface fuel accumulation in

burned and unburned mixed-conifer forests of the Central and Southern Sierra Nevada, CA

(USA). *Fire Ecology*, *2*(1), 53–72.

Kochanski, A. K., Jenkins, M. A., Mandel, J., Beezley, J. D., Clements, C. B., & Krueger, S. (2013).

Evaluation of WRF-SFIRE performance with field observations from the FireFlux

experiment. *Geoscientific Model Development*, *6*(4), 1109–1126.

Kochanski, A. K., Herron-Thorpe, F., Mallia, D. V., Mandel, J., & Vaughan, J. K. (2021). Integration

of a coupled fire-atmosphere model into a regional air quality forecasting system for

wildfire events. *Frontiers in Forests and Global Change*, *4*.

https://doi.org/10.3389/ffgc.2021.728726

Kosovic, B. (2021). *WPS-GEO-LocalFilter: Python scripts for local filtering of terrain heights in

WPS geo_em* files created by geogrid.exe*. [Software] Github. Retrieved from

https://github.com/brankokosovic/WPS-GEO-LocalFilter

Kosović, B., Jimenez, P., & McCandless, T. (2020). Estimation Of Fuel Moisture Content by

Integrating Surface and Satellite Observations Using Machine Learning. *IGARSS 2020-2020*.

Retrieved from

https://ieeexplore.ieee.org/abstract/document/9323134/?casa_token=Ryzhr34S48YAAAA

A:ncKoFH9fH0Wp8diNdVyw_pdyCMmd409halIxweDSOHmY_JlahDu__mZIYzOlEB-

8My45cfUxr7c

Kosovic, B., Massie, S., McCandless, T., Petzke, B., Jimenez Munoz, P., DeCastro, A., Siems-

Anderson., A. (2019). Fuel Moisture Content (Live and Dead) over the Conterminous United

States. Version 1.0. UCAR/NCAR - GDEX [Dataset]. https://doi.org/10.5065/qt42-zd40

Krishna, M., Saide, P. E., Ye, X., Turney, F., & Hair, J. (2023). Evaluation of Wildfire Plume

Injection Heights Estimated from Operational Weather Radar Observations using Airborne

Lidar Retrievals. *Authorea*. https://doi.org/10.22541/essoar.169447401.10794597

Kumar, R., Bhardwaj, P., Pfister, G., Drews, C., Honomichl, S., & D'Attilo, G. (2021). Description

and Evaluation of the Fine Particulate Matter Forecasts in the NCAR Regional Air Quality

Forecasting System. *Atmosphere*, *12*(3), 302.

Lareau, N. P., Nauslar, N. J., Bentley, E., Roberts, M., Emmerson, S., Brong, B., et al. (2022). Fire-

Generated Tornadic Vortices. *Bulletin of the American Meteorological Society*, *103*(5),

E1296–E1320.

Lee, G.-J., Muñoz-Esparza, D., Yi, C., & Choe, H. J. (2019). Application of the Cell Perturbation

Method to Large-Eddy Simulations of a Real Urban Area. *Journal of Applied Meteorology*

and Climatology, *58*(5), 1125–1139.

Lee, J. M., Mirocha, J. D., Lareau, N. P., Whitney, T., To, W., Kochanski, A., & Lassman, W.

(2023). Sensitivity of pyrocumulus convection to tree mortality during the 2020 creek fire

in California. *Geophysical Research Letters*, *50*(16). https://doi.org/10.1029/2023gl104193

Levin, N., Yebra, M., & Phinn, S. (2021). Unveiling the factors responsible for Australia's Black

Summer fires of 2019/2020. *Fire*, *4*(3), 58.

Li, Fangjun, Xiaoyang Zhang, Shobha Kondragunta, Christopher C. Schmidt, and Christopher D.

Holmes. 2020. "A Preliminary Evaluation of GOES-16 Active Fire Product Using Landsat-8

and VIIRS Active Fire Data, and Ground-Based Prescribed Fire Records." *Remote Sensing of*

Environment 237 (February): 111600.

Li, S., Jaroszynski, S., Pearse, S., Orf, L., & Clyne, J. (2019). VAPOR: A Visualization Package

Tailored to Analyze Simulation Data in Earth System Science [Software]. *Atmosphere*, *10*(9),

488.

Mandel, J., Beezley, J. D., & Kochanski, A. K. (2011, February 7). *Coupled atmosphere-wildland*

fire modeling with WRF-Fire. *arXiv [physics.ao-ph]*. Retrieved from

http://arxiv.org/abs/1102.1343

Ma, W., Wilson, C. S., Sharples, J. J., & Jovanoski, Z. (2023). Investigating the Effect of Fuel

Moisture and Atmospheric Instability on PyroCb Occurrence over Southeast Australia.

Atmosphere, *14*(7), 1087.

Mandel, J., Amram, S., Beezley, J. D., Kelman, G., Kochanski, A. K., Kondratenko, V. Y., et al.

(2014). New features in WRF-SFIRE and the wildfire forecasting and danger system in Israel.

Natural Hazards and Earth System Sciences Discussions, *2*(2), 1759–1797.

McCaffrey, S., McGee, T. K., & Coughlan, M. (2020). … wildfire mitigation and preparedness in

the context of extreme wildfires and disasters: Social science contributions to

understanding human response to wildfire. *Extreme Wildfire Events and*. Retrieved from

https://www.sciencedirect.com/science/article/pii/B9780128157213000084

McHardy, T., Peterson, D., Apke, J., Miller, S., Campbell, J. Hyer, E. (2024, in review). Novel

    Comparison of Pyrocumulonimbus Updrafts to Volcanic Eruptions and Supercell

    Thunderstorms Using Optical Flow Techniques.

Moinuddin, K., Khan, N., & Sutherland, D. (2021). Numerical study on effect of relative humidity

    (and fuel moisture) on modes of grassfire propagation. *Fire Safety Journal*, *125*, 103422.

Muñoz-Esparza, D., Kosović, B., Jiménez, P. A., & Coen, J. L. (2018). An Accurate Fire-Spread

    Algorithm in the Weather Research and Forecasting Model Using the Level-Set Method.

    Journal of Advances in Modeling Earth Systems, *10*(4), 908–926.

NASA/LARC/SD/ASDC. (2020). FIREX-AQ DC-8 In-Situ Aerosol Data [Dataset]. NASA Langley

    Atmospheric Science Data Center DAAC. Retrieved from

    https://doi.org/10.5067/ASDC/FIREXAQ_Aerosol_AircraftInSitu_DC8_Data_1

Nolan, R. H., Bowman, D. M. J. S., Clarke, H., Haynes, K., Ooi, M. K. J., Price, O. F., et al. (2021).

    What Do the Australian Black Summer Fires Signify for the Global Fire Crisis? *Fire*, *4*(4), 97.

Pagnini, & Massidda. (2011). The randomized level-set method to model turbulence effects in

    wildland fire propagation. *Fire Behaviour and Risk. Proceedings of …*. Retrieved from

    https://www.researchgate.net/profile/Luca-

    Massidda/publication/322023955_The_randomized_level-

    set_method_to_model_turbulence_effects_in_wildland_fire_propagation/links/5a3e4fb5a

    6fdcce197011560/The-randomized-level-set-method-to-model-turbulence-effects-in-

    wildland-fire-propagation.pdf

Peterson, D., Hyer, E., & Wang, J. (2013). A short-term predictor of satellite-observed fire

    activity in the North American boreal forest: Toward improving the prediction of smoke

emissions. *Atmospheric Environment*, *71*, 304–310.

Peterson, D., Wang, J., Ichoku, C., Hyer, E., & Ambrosia, V. (2013). A sub-pixel-based calculation of fire radiative power from MODIS observations: 1: Algorithm development and initial assessment. *Remote Sensing of Environment*, *129*, 262–279.

Peterson, D. A., Fromm, M. D., Solbrig, J. E., Hyer, E. J., Surratt, M. L., & Campbell, J. R. (2017). Detection and Inventory of Intense Pyroconvection in Western North America using GOES-15 Daytime Infrared Data. *Journal of Applied Meteorology and Climatology*, *56*(2), 471–493.

Peterson, D. A., Thapa, L. H., Saide, P. E., Soja, A. J., Gargulinski, E. M., Hyer, E. J., et al. (2022). Measurements from inside a thunderstorm driven by wildfire: The 2019 FIREX-AQ field experiment. *Bulletin of the American Meteorological Society*. https://doi.org/10.1175/bams-d-21-0049.1

Preisler, H. K., & Westerling, A. L. (2007). Statistical Model for Forecasting Monthly Large Wildfire Events in Western United States. *Journal of Applied Meteorology and Climatology*, *46*(7), 1020–1030.

Quaife, B., & Speer, K. (2021). A Simple Model for Wildland Fire Vortex–Sink Interactions. *Atmosphere*. Retrieved from https://www.mdpi.com/2073-4433/12/8/1014

Rai, R. K., Berg, L. K., Kosović, B., Haupt, S. E., Mirocha, J. D., Ennis, B. L., & Draxl, C. (2019). Evaluation of the Impact of Horizontal Grid Spacing in Terra Incognita on Coupled Mesoscale–Microscale Simulations Using the WRF Framework. *Monthly Weather Review*, *147*(3), 1007–1027.

Roberts, M., Lareau, N., Juliano, T., Shamsaei, K., Hamed, Ebrahimian, & Kosović, B. (2023).

Sensitivity of simulated fire-generated circulations to fuel characteristics during large

wildfires. https://doi.org/10.22541/essoar.169264796.69205142

Rodriguez, B., Lareau, N. P., Kingsmill, D. E., & Clements, C. B. (2020). Extreme pyroconvective

updrafts during a megafire. *Geophysical Research Letters*, *47*(18).

https://doi.org/10.1029/2020gl089001

Rogers, E., DiMego, G., Black, T., Ek, M., Ferrier, B., Gayno, G., et al. (2009). The NCEP North

American mesoscale modeling system: Recent changes and future plans. In *Preprints, 23rd*

Conference on weather analysis and forecasting/19th conference on numerical weather

prediction. ams.confex.com. Retrieved from

https://ams.confex.com/ams/23WAF19NWP/techprogram/paper_154114.htm

Roos, C. I., Rittenour, T. M., Swetnam, T. W., Loehman, R. A., Hollenback, K. L., Liebmann, M. J.,

& Rosenstein, D. D. (2020). Fire Suppression Impacts on Fuels and Fire Intensity in the

Western U.S.: Insights from Archaeological Luminescence Dating in Northern New Mexico.

Fire, *3*(3), 32.

Rothermel, R. C. (1972). *A Mathematical Model for Predicting Fire Spread in Wildland Fuels*.

Intermountain Forest & Range Experiment Station, Forest Service, U.S. Department of

Agriculture.

Ryan, K. C., & Opperman, T. S. (2013). LANDFIRE – A national vegetation/fuels data base for use

in fuels treatment, restoration, and suppression planning. *Forest Ecology and*

Management, *294*, 208–216.

Saide, P. E., Krishna, M., Ye, X., Thapa, L. H., Turney, F., Howes, C., & Schmidt, C. C. (2023). Estimating fire radiative power using weather radar products for wildfires. *Geophysical Research Letters*, *50*(21). https://doi.org/10.1029/2023gl104824

Salis, M., Arca, B., Alcasena, F., Arianoutsou, M., Bacciu, V., Duce, P., et al. (2016). Predicting wildfire spread and behaviour in Mediterranean landscapes. *International Journal of Wildland Fire*, *25*(10), 1015–1032.

Salas-Porras, E. D., Tazi, K., Braude, A., Okoh, D., Lamb, K. D., Watson-Parris, D., et al. (2022, November 16). *Identifying the Causes of Pyrocumulonimbus (PyroCb). arXiv [stat.ML]*. Retrieved from http://arxiv.org/abs/2211.08883

Schmidt, C. (2020). Monitoring fires with the GOES-R series. In *The GOES-R Series* (pp. 145–163). Elsevier.

Scott, J. H. (2005). *Standard Fire Behavior Fuel Models: A Comprehensive Set for Use with Rothermel's Surface Fire Spread Model*. U.S. Department of Agriculture, Forest Service, Rocky Mountain Research Station.

Shamsaei, K., Juliano, T. W., Roberts, M., Ebrahimian, H., Lareau, N. P., Rowell, E., & Kosovic, B. (2023, May 24). *The role of fuel characteristics and heat release formulations in coupled fire-atmosphere simulation*. *Preprints*. https://doi.org/10.20944/preprints202305.1672.v1

Simpson, C. C., Sharples, J. J., & Evans, J. P. (2014). Resolving vorticity-driven lateral fire spread using the WRF-Fire coupled atmosphere–fire numerical model. *Natural Hazards and Earth System Sciences*, *14*(9), 2359–2371.

Skamarock, W. C., J. B. Klemp, J. Dudhia, D. O. Gill, Z. Liu, J. Berner, W. Wang, J. G. Powers, M. G. Duda, D. M. Barker, and X.-Y. Huang, 2019: A Description of the Advanced Research WRF

Version 4. *NCAR Tech. Note NCAR/TN-556+STR*, 145 pp.

[doi:10.5065/1dfh-6p97](doi:10.5065/1dfh-6p97) Sussman, M., Smereka, P., & Osher, S. (1994). A Level Set Approach for Computing Solutions to Incompressible Two-Phase Flow. *Journal of Computational Physics*, *114*(1), 146–159.

Sofiev, M., Ermakova, T., & Vankevich, R. (2011). Evaluation of the smoke-injection height from wild-land fires using remote-sensing data. *Atmospheric Chemistry and Physics*, *12*, 1995–2006.

Stephens, S. L., Bernal, A. A., Collins, B. M., Finney, M. A., Lautenberger, C., & Saah, D. (2022). Mass fire behavior created by extensive tree mortality and high tree density not predicted by operational fire behavior models in the southern Sierra Nevada. *Forest Ecology and Management*, *518*, 120258.

Thapa, L. H., Ye, X., Hair, J. W., Fenn, M. A., Shingler, T., Kondragunta, S., et al. (2022). Heat flux assumptions contribute to overestimation of wildfire smoke injection into the free troposphere. *Communications Earth & Environment*, *3*(1), 1–11.

Turney, F. (2023). Williams Flats WRF-Fire Output Contain for FMC [Dataset]. Zenodo. https://doi.org/10.5281/zenodo.7693759

Tymstra, C., Bryce, R. W., Wotton, B. M., Taylor, S. W., Armitage, O. B., & Others. (2010). Development and structure of Prometheus: the Canadian wildland fire growth simulation model. *Natural Resources Canada, Canadian Forest Service, Northern Forestry Centre, Information Report NOR-X-417. (Edmonton, AB)*. Retrieved from http://epe.lac-bac.gc.ca/100/200/301/nrcan-rncan/cfs-scf/nor-x/dev_structure_prometheus/31775.pdf

Tymstra, C., Jain, P., & Flannigan, M. D. (2021). Characterisation of initial fire weather

conditions for large spring wildfires in Alberta, Canada. *International Journal of Wildland Fire*, *30*(11), 823–835.

Wang, Q., Ihme, M., Linn, R. R., Chen, Y.-F., Yang, V., Sha, F., et al. (2022, December 9). *A High-resolution Large-eddy Simulation Framework for Wildfire Predictions using TensorFlow*. *arXiv [physics.flu-dyn]*. Retrieved from http://arxiv.org/abs/2212.05141

Western Regional Climate Center. n.d. "RAWS USA Climate Archive State Selection Map [Software]." Accessed July 8, 2023. https://raws.dri.edu/.

Wiedinmyer, C., Akagi, S. K., Yokelson, R. J., Emmons, L. K., Al-Saadi, J. A., Orlando, J. J., & Soja, A. J. (2011). The Fire INventory from NCAR (FINN): a high resolution global model to estimate the emissions from open burning. *Geoscientific Model Development*, *4*(3), 625–641.

Wildland Fire Interagency Data Service (WFIGS), National Interagency Fire Center (NIFC), National Wildfire Coordinating Group (NWCG) Geospatial Subcommittee. 2021. Operational Data Archive 2019 [Dataset]. January 7, 2021. https://data-nifc.opendata.arcgis.com/.

Wooster, M. J. (2002). Small‐scale experimental testing of fire radiative energy for quantifying mass combusted in natural vegetation fires. *Geophysical Research Letters*, *29*(21). https://doi.org/10.1029/2002gl015487

WPS: The official repository for the WRF Preprocessing System (WPS). (n.d.) [Software]. Github. Retrieved from https://github.com/wrf-model/WPS

WRF: The official repository for the Weather Research and Forecasting (WRF) model. (n.d.) [Software]. Github. Retrieved from https://github.com/wrf-model/WRF

Wyngaard, J. C. (2004). Toward Numerical Modeling in the "Terra Incognita." *Journal of the Atmospheric Sciences*, *61*(14), 1816–1826.

Xu, Weidong, Martin J. Wooster, Jiangping He, and Tianran Zhang. 2021. "Improvements in High-Temporal Resolution Active Fire Detection and FRP Retrieval over the Americas Using GOES-16 ABI with the Geostationary Fire Thermal Anomaly (FTA) Algorithm." *Egyptian Journal of Remote Sensing and Space Sciences* 3 (June): 100016.

Ye, X., Saide, P. E., daSilva, A., Kondragunta, S., Lyapustin, A., Wang, Y., et al. (2019). Evaluation of biomass burning smoke simulations incorporating near real-time inversions of multi-fire emissions over the Western U.S (Vol. 2019, p. A22A–07).

Ye, X., Arab, P., Ahmadov, R., James, E., & Saide, P. E. (2021). Evaluation and intercomparison of wildfire smoke forecasts from multiple modeling systems for the 2019 Williams Flats fire. *Atmospheric Chemistry and Physics*, *21*(18), 14427–14469.